Strange Particle Production in Proton-Proton Collisions at 158 GeV

Ph.D. Thesis

Dániel Barna

Doctoral School of Physics, Eötvös Loránd University
Head: Dr. Zalán Horváth

Particle Physics and Astronomy Program
Head: Dr. György Pócsik

Supervisor: Dr. György Vesztergombi

KFKI Research Institute for Particle and Nuclear Physics
Budapest

November, 2002

Summary

A new experimental procedure to reconstruct neutral strange particles (so-called V^0s, like Λ, $\overline{\Lambda}$) and multiply strange particles (*cascades*, like Ξ^- and Ω^-) in the NA49 experiment at the CERN SPS is presented in this thesis, together with the results obtained by this method in proton-proton collisions at 158 GeV beam energy.

The NA49 experiment, its detector system and reconstruction software is briefly described. The way from the detector signals to reconstructed particle trajectories is explained, with special emphasis on V^0 and cascade reconstruction. The newly developed procedure is presented together with another method. These two methods are compared, and their performance is studied in detail. Arguments for the need of the newly developed procedure (and for the need of two independent methods) are given.

The results of my work, presented in this thesis (obtained by combining the results of the two separate methods) are as follows:

- Inclusive longitudinal and transverse momentum distributions of Λ and $\overline{\Lambda}$ in proton-proton collisions are presented, providing a large improvement in quality compared to the previously existing results. The shape of the transverse momentum distribution is found to be independent from the longitudinal momentum.

- Previously existing experimental data on Λ and $\overline{\Lambda}$ production in p-p collisions are compiled, and compared to the NA49 results.

- Inclusive longitudinal and transverse momentum distributions of the Ξ^- and $\overline{\Xi}^+$ particles in proton-proton collisions are presented. These are the first measurement of Ξ production cross sections in proton-proton collisions.

- The Ω^- particle is observed in proton-proton collisions for the first time. Its production cross section in the central region is estimated to be $(8.5 \pm 1.3) \cdot 10^{-5}$ per inelastic event and unit of rapidity. The upper limit for the $\overline{\Omega}^+/\Omega^-$ ratio is estimated to be 0.5 with 95% confidence level. Antibaryon to baryon ratios are presented and compared to model predictions as a function of strangeness. These results contradict to the predictions of string models.

- The transverse momentum distributions of Λs and protons are compared at midrapidity, and are found to have a very similar shape. $\overline{\Lambda}$s and antiprotons also have a very similar p_T distribution, but with smaller inverse slope.

- Baryon-antibaryon correlations are studied. The rapidity distribution of Λs created in conjunction with $\overline{\Lambda}$s or $\overline{\mathrm{p}}$s has a maximum at midrapidity (contrary to the same distribution in minimum-bias p-p collisions), which is attributed to baryon pair production. The shape of the p_T distribution of Λs created together with $\overline{\Lambda}$s or $\overline{\mathrm{p}}$s has the same shape as in minimum bias proton-proton events.

- Strangeness enhancement in proton-nucleus and nucleus-nucleus collisions is studied, using the results of the NA49 experiment in proton-proton collisions as a reference, and results of the NA49 and WA97 experiments in proton-nucleus and nucleus-nucleus collisions. Enhancement (about a factor of 2) is seen already in p-Be collisions. Larger enhancement is seen for larger number of collisions per participant, and the enhancements in proton-nucleus and nucleus-nucleus collisions are found to be of similar magnitude.

Összefoglaló

A dolgozatban egy új módszert mutatok be semleges ritka részecskék (úgynevezett V^0-k, mint például a Λ, $\overline{\Lambda}$) illetve többszörösen ritka részecskék (úgynevezett kaszkádok: Ξ^- vagy Ω^-) rekonstruálására a CERN SPS gyorsítóján levő NA49 kísérletben, és bemutatom az ezzel a módszerrel kimért eredményeket proton-proton ütközésekben, 158 GeV nyalábenergián.

Röviden bemutatom az NA49 kísérletet, a detektorrendszerét és a rekonstrukciós szoftverét. Bemutatom a detektorok jeleitől a rekonstruált részecskepályákig vezető utat, melynek során különös hangsúlyt kap a V^0 és kaszkád rekonstrukció. Az újonnan kidolgozott módszert egy másik módszerrel együtt tárgyalom; összehasonlítom őket, és bemutatom a teljesítőképességüket, az előnyeiket és hátrányaikat. Megindoklom, hogy miért van szükség az új módszerre – illetve két módszerre is.

A disszertációban bemutatott eredményeim, melyeket a két módszer eredményeit kombinálva kaptam, a következők:

- A Λ és $\overline{\Lambda}$ részecskék inkluzív longitudinális és transzverzális impulzuseloszlásai proton-proton ütközésekben, melyek az eddigi mérési eredmények minőségének nagymértékű javulásához járulnak hozzá. A transzverzális impulzuseloszlás alakját a longitudinális impulzustól függetlennek találtam.

- A korábbi mérési eredményeket összegyűjtöttem a publikációkból, melyeket itt összefoglalok, és összehasonlítom az NA49 kísérletben kapott eredményekkel.

- Bemutatom a Ξ^- és $\overline{\Xi}^+$ részecskék inkluzív longitudinális és transzverzális impulzuseloszlásait proton-proton ütközésekben. Ezek az első erre vonatkozó mérési eredmények proton-proton ütközésekben.

- Első alkalommal tudtuk megfigyelni az Ω^- részecske keletkezését proton-proton ütközésekben. A központi tartományban a keltési hatáskeresztmetszete inelasztikus ütközésenkként, egységnyi rapiditástartományban $(8.5\pm1.3)\cdot10^{-5}$-nek adódott. Az $\overline{\Omega}^+/\Omega^-$ keletkezési arány felső határa 95% konfidenciaszinntel 0,5-nek adódott. A mért antibarion/barion arányok ellentmondanak a string-modellek jóslatainak.

- Összehasonlítom a Λ és proton transzverzális impulzuseloszlásait 0 rapiditásnál. A két részecske eloszlásának alakja igen hasonlónak bizonyult. Az $\overline{\Lambda}$-k és antiprotonok szintén nagyon hasonló alakú transzverzális impulzus eloszlással rendelkeznek, ám az eloszlásuk meredekebb.

- Bemutatom barion-antibarion korrelációk vizsgálatát. Az $\overline{\Lambda}$-val vagy $\overline{\mathrm{p}}$-nal együtt keletkező Λ-knak a rapiditáseloszlása (ellentétben az átlagos p-p ütközésekben mért eloszlással) 0 rapiditásnál maximummal rendelkezik, amit a barion párkeltésnek tulajdonítok. A Λ-k p_T eloszlásának alakja nem változik meg, ha $\overline{\Lambda}$-val vagy $\overline{\mathrm{p}}$-nal keletkező részecskéket vizsgálunk.

- Megvizsgáltam a ritka részecskék keletkzési gyakoriságának növekedését proton-atommag, illetve atommag-atommag ütközésekben. Azt találtam, hogy már p-Be ütközésekben is megfigyelhető egy körülbelül kétszeres növekedés. Nagyobb növekedés figyelhető meg az olyan ütközésekben, ahol a résztvevő nukleonok átlagosan többet ütköznek. Proton-atommag illetve atommag-atommag ütközésekben hasonló nagyságú növekedést tapasztaltam.

Contents

1 Introduction **1**

1.1 Heavy Ion Physics and the Quark Gluon Plasma 2

1.2 Author's Contribution, and the Structure of this Thesis 5

2 The NA49 Experiment **7**

2.1 The NA49 Coordinate System 8

2.2 Beam Definition, Trigger System and Target Setups 8

2.2.1 The Beam Definition 8

2.2.2 The Trigger System 9

2.2.3 The Target Setup 10

2.3 The Time Projection Chambers (TPC) 11

2.3.1 Operation of the TPCs 11

2.3.2 Construction 13

2.3.3 Readout Electronics and DAQ 15

2.4 The Time of Flight Detectors 15

2.5 The Ring Calorimeter and Veto Proportional Chamber 16

3 The NA49 Software **17**

3.1 The Reconstruction Software 17

3.1.1 Cluster Finding 18

3.1.2 Tracking and Momentum Fit 20

3.1.3 The Momentum Fitting Procedure 21

3.1.4 Main Vertex Reconstruction 21

3.1.5 Track Merging 22

3.2 Particle Identification: Specific Energy Loss 22

3.3 Simulation 25

4 V^0 and Cascade Finding **28**

4.1 The Original Methods . . . 29

4.1.1 V^0 Reconstruction . . . 29

4.1.2 Cascade Reconstruction . . . 31

4.1.3 Limitations . . . 31

4.2 The New Method . . . 33

4.2.1 V^0 Reconstruction . . . 33

4.2.2 Cascade Reconstruction . . . 36

4.2.3 Outlier Removal . . . 36

4.2.4 Performance of `MTVO` . . . 41

5 Analysis **48**

5.1 Selection of Candidates . . . 48

5.2 Event Selection and Cross Section Determination . . . 53

5.2.1 Trigger Cross Section . . . 53

5.2.2 Event Selection . . . 54

5.2.3 The Event Weighting Technique . . . 56

5.3 Determination of the Number of Candidates . . . 58

6 Results **60**

6.1 Λ and $\overline{\Lambda}$ Results . . . 60

6.1.1 Rapidity – p_T binning . . . 60

6.1.2 Feynman-x – p_T binning . . . 65

6.2 Ξ Results . . . 69

6.2.1 Rapidity and Feynman-x Distributions . . . 69

6.2.2 Transverse Spectra . . . 70

6.3 $\Xi \rightarrow \Lambda$ Feeddown Correction . . . 71

6.4 Ω Results . . . 76

6.5 Stability of `MTVO` Results . . . 77

6.5.1 Stability Against the Cuts . . . 77

6.5.2 Stability of the Event Weighting Procedure . . . 77

6.5.3 Stability of the Ξ^- Results . . . 81

6.5.4 Averaging Between the two Finders . . . 83

7 Final Results and Discussion **88**

7.1 The Final Spectra of Strange and Multistrange Particles 88

7.1.1 Λ and $\overline{\Lambda}$ Spectra 88

7.1.2 Ξ^- and $\overline{\Xi}^+$ Results 95

7.2 Comparison to Other Measurements 97

7.3 Ω Yields 105

7.3.1 Experimental Results 105

7.3.2 Comparison to Model Predictions 106

7.4 Energy-dependence of midrapidity yields 108

7.5 Transverse Momentum Distributions of Λ and $\overline{\Lambda}$ at Midrapidity 111

7.6 Study of Baryon-Antibaryon Correlations 112

7.6.1 Experimental Results 112

7.6.2 Comparison to Model Predictions 121

7.7 Strangeness Enhancement in p-A and A-A collisions 123

7.7.1 Determination of Centrality or the Number of Collisions 123

7.7.2 Definitions of Strangeness Enhancement 124

7.7.3 Experimental Results 126

7.8 Summary and Outlook 129

A Numerical Results **130**

B Kinematical variables **134**

Chapter 1

Introduction

The history of strange particles begins in 1947 with the discovery of the so-called V particles, which left tracks in the shape of a V in nuclear emulsion, due to their decay into two charged particles. The first such particles are now called kaons (K^0) and lambdas (Λ^0). Later, when they were also produced in accelerators, they were called *strange* particles, because they were always created in pairs via the *strong* interaction; and though they were all unstable, their lifetime was long, indicating that they decay via the *weak* interaction. In order to explain these phenomena, a new quantum number (called *strangeness*, S) was introduced; lambdas were given $S = +1$, kaons were given $S =$ -1 or +1. A conservation law for strangeness in the strong interaction assured that these particles are produced in pairs, and – when they are separated in space and time – they can not decay via the strong interaction.

According to our current knowledge all hadrons are composed of *quarks*; in this model the strangeness quantum number is carried by the s (strange) quark. The study of the production of particles containing a strange quark is especially interesting due to the following reasons:

- The most common hadrons in our daily world (protons, neutrons) or the most easily created pions are composed of u and d quarks, and contain no s valence quarks. By the observation of strange particle production in particle collisions one can study the production of a new quark, which was not present in the initial state.

- The s quark is not only absent in the initial states of usual particle collisions, but it has higher mass than the u and d quarks. Production of s quarks might therefore be energetically disfavored under certain circumstances. In other cases

this suppression might be absent. Strange particle yields can therefore be an indicator of physical conditions during the collisions.

- Though the mass of the s quark is higher than that of the u and d, this mass is still substantially smaller than the mass of the remaining 3 quarks (c, b and t). This results in a relatively high production rate of strange particles compared to other ones containing these three quarks, such as the D mesons ($D^+ = c\overline{d}$, $D^0 = c\overline{u}$, $\overline{D}^0 = \overline{c}u$, $D^- = \overline{c}d$), the B mesons ($B^+ = u\overline{b}$, $B^0 = d\overline{b}$, $\overline{B}^0 = \overline{d}b$, $B^- = \overline{u}b$) or the charmed lambda baryon ($\Lambda_c^+ = udc$). This makes them a good candidate for experimentalists.

- Through their weak decay and long lifetime these particles most often offer a unique way to their identification.

In the remaining part of this introduction some of these aspects will be described in more details.

1.1 Heavy Ion Physics and the Quark Gluon Plasma

The quark model of hadrons (introduced and developed by Gell-Mann and Zweig in the 1960's) was not immediately generally accepted. One of the strongest objections to the model was that no free quarks have ever been observed. The current theory of the strong interaction, Quantum Chromodynamics (QCD) now successfully explains this by the *quark confinement*. QCD is a non-Abelian gauge theory, which uses the same mathematical apparatus and formalism, which is used by Quantum Electrodynamics, one of the most successful and accurate theories in physics.

However, due to the non-Abelian nature of this theory one faces difficulties during its practical applications. Processes involving small momentum transfers (soft hadronic physics) are difficult to deal with. At low momentum transfers the coupling constant of the theory diverges, prohibiting the perturbative approach. Numerical calculations are used instead (lattice QCD), or phenomenological/microscopic models, in the form of computer code (so-called *event generators*, which generate event configurations of different reactions).

The numerical calculations predict that under extremely high temperature and pressure a new state of matter, the *Quark Gluon Plasma* (QGP) will be formed. Within

this state of matter the quarks and gluons get free from being confined into protons and nucleons. These extreme conditions are hoped to be reached in high-energy heavy ion collisions. According to expectations, in high-energy collisions the nucleons of the two colliding nuclei will melt into a deconfined state, where quarks and gluons can move freely. However, this state will not last forever: after about 5 fm/c [25] the quarks will again form hadrons (*hadronization*). Only the final state hadrons are available to the experiments. To observe the new state, such signatures have to be searched, which survive the process of hadronization.

In the last decade an extensive heavy ion programme was launched internationally to study the various predicted signatures of the QGP. These signatures include (for a more detailed review see for example [6]):

Charmonium suppression

In 1986, Matsui and Satz suggested [7], that if a quark-gluon plasma is formed in heavy ion collisions, the production of charmonia would be suppressed with respect to the superposition of nucleon-nucleon collisions: the deconfining environment of a quark gluon plasma prohibits the formation of $c\overline{c}$ bound states.

Electromagnetic signals

Particles which do not interact strongly (leptons, photons), are unaffected by the process of hadronization. They deliver information from the phase where they were created, in the form of production rates and momentum distributions. The most prominent processes for direct photon production are $q\overline{q} \rightarrow \gamma g$ and $gq \rightarrow \gamma q$. Virtual photons created in the same way can decay into a lepton-antilepton pair.

Strangeness enhancement

In proton-proton collisions the production of particles containing a strange quark or antiquark is strongly suppressed compared to the production of particles containing only u and d quarks. This is explained by the higher mass of the s quark. The suppression increases with the strangeness content of the produced particle. Moreover, in proton-proton collisions strange particles can only be created in such a way, that all relevant quantum numbers are conserved. The process for Λ creation with the lowest threshold

energy is $pp \rightarrow p\Lambda K^+$ ($E_{thres.} = 674$ MeV). To produce an antilambda even more energy is required: $pp \rightarrow pp\Lambda\overline{\Lambda}$ ($E_{thres.} = 2.23$ GeV).

In the case of QGP formation, $s\overline{s}$ pairs can be produced via the interactions of two gluons ($gg \rightarrow s\overline{s}$) or a quark and an antiquark ($q\overline{q} \rightarrow s\overline{s}$). These channels do not produce strange hadrons (with large masses), only $s\overline{s}$ pairs, and therefore require much less threshold energy. The strange quarks combine with other quarks during hadronization to form strange hadrons.

Based on these arguments the yield of strange and multi-strange mesons and baryons has been predicted to be strongly enhanced in a QGP compared to elementary hadronic collisions [8,9].

A wide spectrum of interesting experimental results has been obtained by the heavy ion experiments. These results, however, can not be interpreted without a precise knowledge about elementary collisions:

- In order to trace the signatures of new physics one has to know, what can be expected and predicted from elementary collisions.
- Experimental results from heavy ion collisions are often compared to predictions of event generators. The accurate testing of these models with elementary collisions is therefore very important.

Due to the above arguments the experimental interest has again turned towards elementary reactions (including proton-proton and proton-nucleus collisions, which are often referred to as p-A collisions). However, precise data on strange particle production in proton-proton collisions is still missing, and the existing results do not go beyond the measurement of inclusive particle spectra: most of the available data on Λ and $\overline{\Lambda}$ production in p-p collisions originate from bubble chamber experiments with low statistics and large errorbars. As a reference for heavy ion collisions the results in p-Be collisions were used, instead of the p-p results measured by these old experiments. The heavy ion community has been lacking precise data on Λ and $\overline{\Lambda}$ production in p-p collisions measured by a high-statistics experiment. Moreover, Ξ^- and $\overline{\Xi}^+$ production (not to mention the Ω baryon) was not yet measured at all in p-p collisions. This situation produces an urgent need for detailed results on strange particle production in proton-proton collisions.

The main goals of the experimental work presented in this thesis is to fill this long-existing gap in the hadronic data. Through the measurement of strange particle cross sections we would like to provide precise reference data for strangeness enhancement studies. Through the presentation of experimental results beyond the inclusive level (particle correlations) we would like to offer the possibility of a more detailed test of event generators in elementary collisions, and stimulate theoretical activities about such open questions, which could not be answered in the past, due to lacking experimental data.

Throughout this thesis the natural units $\hbar = c = 1$ will be used. Mass and momentum values will be written in GeV.

1.2 Author's Contribution, and the Structure of this Thesis

The author participated in the acquisition of data which were used in this thesis. The author has developed a complete reconstruction software (`MTVO`) to find strange and multistrange hadrons (V^0s and cascades), and has participated in the collaboration meetings, presenting the status and results of this software. This software was meant to be an extension of already existing softwares (`VOFIND` for V^0 finding, and `XI_FIND` for cascade finding), but was later used as an independent finder. The author was responsible for the maintenance of this software, and has done the full analysis of Λ, $\overline{\Lambda}$, Ξ and $\overline{\Xi}$ particles in the proton-proton data using this software. The independent results obtained by `MTVO` were then combined with the results of `VOFIND` and `XI_FIND`, and these combined results are in preparation for publishing.

Chapter 2 will present the NA49 experiment. Most of its components and detectors will be described; but only those will be detailed, which were essential for the work presented in this thesis.

As most modern experiments in particle physics, NA49 also uses a huge software to reconstruct the usable physical information from the signals of the detectors. Since the author also contributed to this software, and this work could not be understood without the knowledge about this environment, chapter 3 will describe the reconstruction software of NA49 in details.

As it was already mentioned earlier, a new V^0- and cascade-finder (`MTVO`) was developed within the framework of this thesis. There already existed another finder for this

purpose in the experiment, so this work might seem to be needless. In order to convince the reader that this was not so, and give a good reasoning for such a 'duplicated' work, the V^0- and cascade-finding will be described in detail in a separate chapter (4). Both the original and the new finders will be described and their performance compared.

Chapter 5 will present the analysis procedure, and all the technicalities, which were needed during the data analysis. The results obtained by `MTVO` and `VOFIND`,`XI_FIND` separately will be presented and compared in chapter 6, together with the applied corrections, discussion about the stability of these results, and the method to derive the final results.

Chapter 7 contains the final spectra obtained by merging the results of the two finders. These results will be used to discuss topical questions of particle and heavy ion physics.

Chapter 2

The NA49 Experiment

NA49 is a large-acceptance, general purpose fixed target experiment located in the **N***orth* **A***rea* experimental hall of CERN (European Organization for Nuclear Research) [3], on the S4 beam of the SPS (*Super Proton Synchrotron*). This accelerator provides proton and lead-ion beams up to 200 GeV per nucleon. Besides, using a so-called *production target* one can produce several different fragmentation beams as well to study the evolution of the physical phenomena as a function of colliding system size; see section 2.2.1.

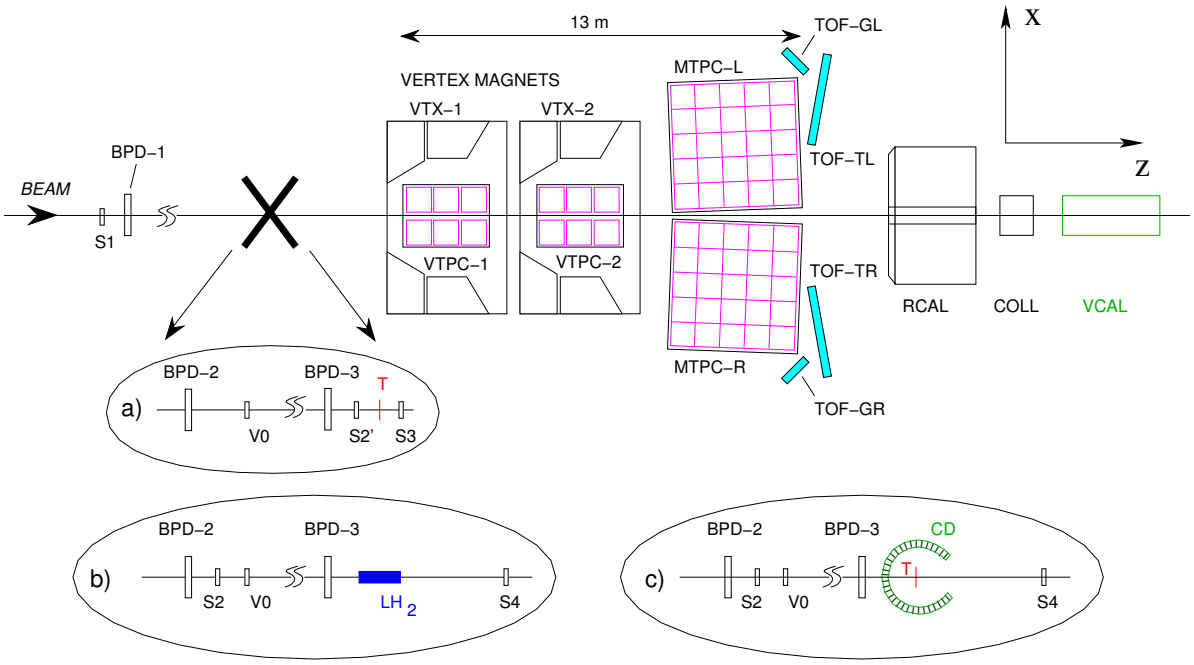

Figure 2.1: Layout of the NA49 experiment: a.) for Pb-Pb b.) for p-p and c.) for p-Pb reactions

The layout of the experiment is shown in figure 2.1. In order to study different reactions, different target setups can be used, which are shown separately in the figure (to be

discussed later). The detector system of NA49 is quite complex. For more details we refer to [4].

2.1 The NA49 Coordinate System

The coordinate system of the experiment is also shown in figure 2.1: the z axis points into the beam direction; the x axis is horizontal (in the plane of the figure), and the y axis is perpendicular to this plane, and points vertically upwards. The origin of the coordinate system is chosen to be the center of VTPC-2.

For a general orientation in the NA49 coordinate system the rough positions of the main detectors are given here:[1] the Main-TPCs are roughly between $z = 360$ cm and 730 cm; VTPC-2 extends roughly from $z = -115$ cm to $z = 115$ cm, and VTPC-1 from $z = -500$ cm to $z = -270$ cm.

2.2 Beam Definition, Trigger System and Target Setups

2.2.1 The Beam Definition

To study proton- or Pb-induced reactions, the proton or Pb beam extracted from the SPS is directly incident on the target of the experiment.

In order to study reactions with different beam particles, the proton or lead beam extracted from the SPS is directed onto a beryllium block, which is called the *production target*. There is a bulk of particles produced in the interaction of the primary beam with the production target. Magnets and collimators are used to select a small momentum interval of these particles. These particles are called the *secondary beam*. Note that only the momentum of the secondary beam can be selected this way; it consists of different types of particles (mostly pions). A Čerenkov detector is placed in the beamline, which can be tuned to be sensitive to only one type of particles at this momentum. When using a secondary beam, this detector is included in the trigger system, and it is used to tag the desired beam particles.

[1] We do not want to load the reader with the very precise positions, measured to a few 100 microns accuracy

The beam position is determined by 3 Beam Position Detectors (BPD-1, BPD-2 and BPD-3). These are multiwire proportional chambers with two orthogonal sense wire planes and cathode strip readout. The precision of the beam position extrapolated to the target is 40 μm for Pb, and 170 μm for proton beams.

2.2.2 The Trigger System

The trigger system is slightly different for different reactions. Here only the shorthand for the different detector names will be quoted. See figure 2.1 for their location in the experiment.

Pb-Pb collisions: S1, $\overline{\text{V0}}$, S2', $\overline{\text{S3}}$, VCAL

p-Pb collisions: S1, S2, $\overline{\text{V0}}$, CD, $\overline{\text{S4}}$

p-p collisions: S1, S2, $\overline{\text{V0}}$, $\overline{\text{S4}}$

In this notation the overline means that the detector is used in anticoincidence. Most of these detectors are counters, except VCAL and CD. The detectors are centered on the beamline in the x and y directions. Their position along the z (beam-) axis is also shown in brackets.

S1 (-3977 cm): 5 mm thick scintillator, equipped with 4 photomultipliers, approximately 34 m upstream from the target. For heavy ion runs this counter is replaced by a 200 μm thick quartz wafer, producing signals based on the Čerenkov effect.

S2' (-1569 cm): Helium gas Čerenkov counter

S2 (-1569 cm): 2 mm thick scintillator

V0 (1544 cm): Scintillation counter with a hole in the middle. Requiring an anticoincidence with this detector we can filter out interactions occurring in the detectors upstream.

S3 (-580 cm): Helium gas Čerenkov counter. The gas volume actually includes the Pb foil target as well.

S4: (-200 cm) Scintillation counter placed between VTPC-1 and VTPC-2. It is used in anticoincidence to exclude non-interacting beam particles.

CD: Centrality Detector, see figure 2.2.

VCAL: Veto Calorimeter. Detects the particles produced close to the beamline. The energy deposited in this calorimeter is assumed to be proportional to the number of spectators in Pb-Pb collisions, and is therefore a good measure of centrality in Pb-Pb collisions.

2.2.3 The Target Setup

In case of p-Pb and Pb-Pb collisions the beam is incident on a lead foil target (T in subfigures a.) and c.) in fig. 2.1). In case of p-Pb collisions the target is surrounded by the so-called centrality detector (CD, figure 2.2), which counts the *grey* particles.[2] This detector has the shape of a vertical cylinder with 16 cm diameter, and 20 cm height. 32 proportional tubes are located on its wall, having a vertical direction. Each of the cathodes of the tubes are segmented into 8 pieces, which are separately read out. Protons below 0.15 GeV momentum (*black*) are cut off by a cylindrical copper foil between the target and the proportional tubes. The output signals of each cathode segment are discriminated, and if the signal is above a certain threshold, it is accepted as a hit. In order to enrich the data sample with high-centrality events, on-line triggering on the number of hits in this detector is possible. In the later analysis, during the classification of events into different centrality classes, the number of grey particles detected in the TPCs are added to the number of hits observed in the CD. This information (together with model predictions) can be used to determine the centrality of the collisions.

The proton target is a liquid hydrogen tube. During the data taking period in 1996 its length was 14 cm. During later runs (in 1999 and 2000) it was replaced by a 20 cm long tube.

[2] This name originates from the time of emulsions: slower particles left a darker trace in the emulsion. Grey particles have a momentum between few hundred MeV and 1 GeV. Particles with momentum below a few hundred MeV are called *black*

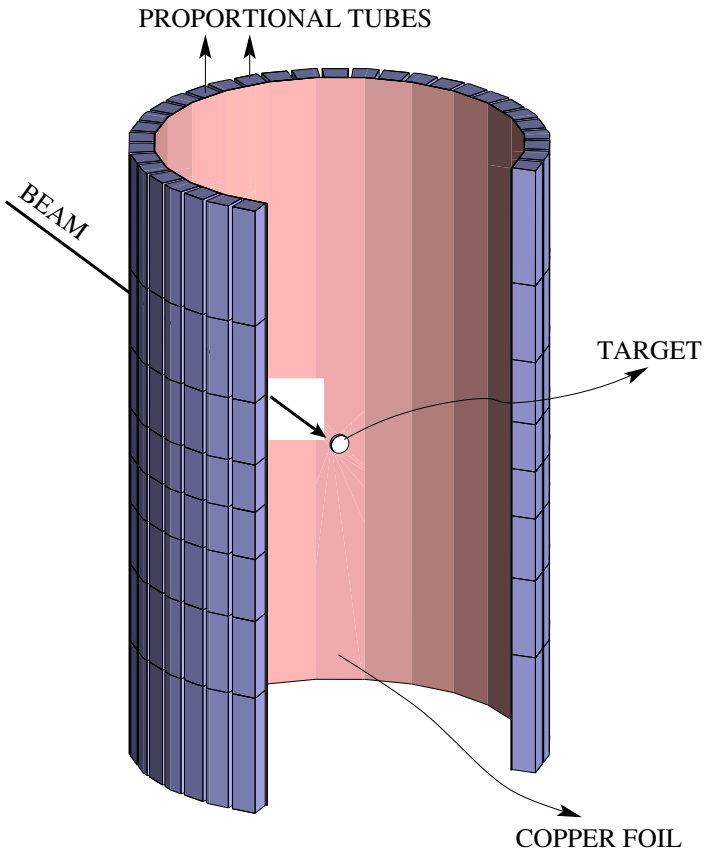

Figure 2.2: The Centrality Detector

2.3 The Time Projection Chambers (TPC)

The main detectors of NA49 are the four time projection chambers: the two Vertex-TPCs (VTPC-1 and VTPC-2) and the two Main-TPCs (MTPC-L and MTPC-R). These chambers are large volume tracking devices. VTPC-1 and VTPC-2 have similar construction and dimensions. MTPC-L and MTPC-R are mirror images of each other, and have different construction from that of the VTPCs.

2.3.1 Operation of the TPCs

TPCs are chambers filled with gas. At the bottom of the chamber the gas volume is limited by the *high voltage plane* (fig. 2.3). At the top of the chamber the *readout plane* is a metal plane segmented into small pieces called *pads*. Three grids of wires are spanned parallel to the readout plane: the *field/sense wire grid*, the *Frisch-grid* and the *Gating-grid*.

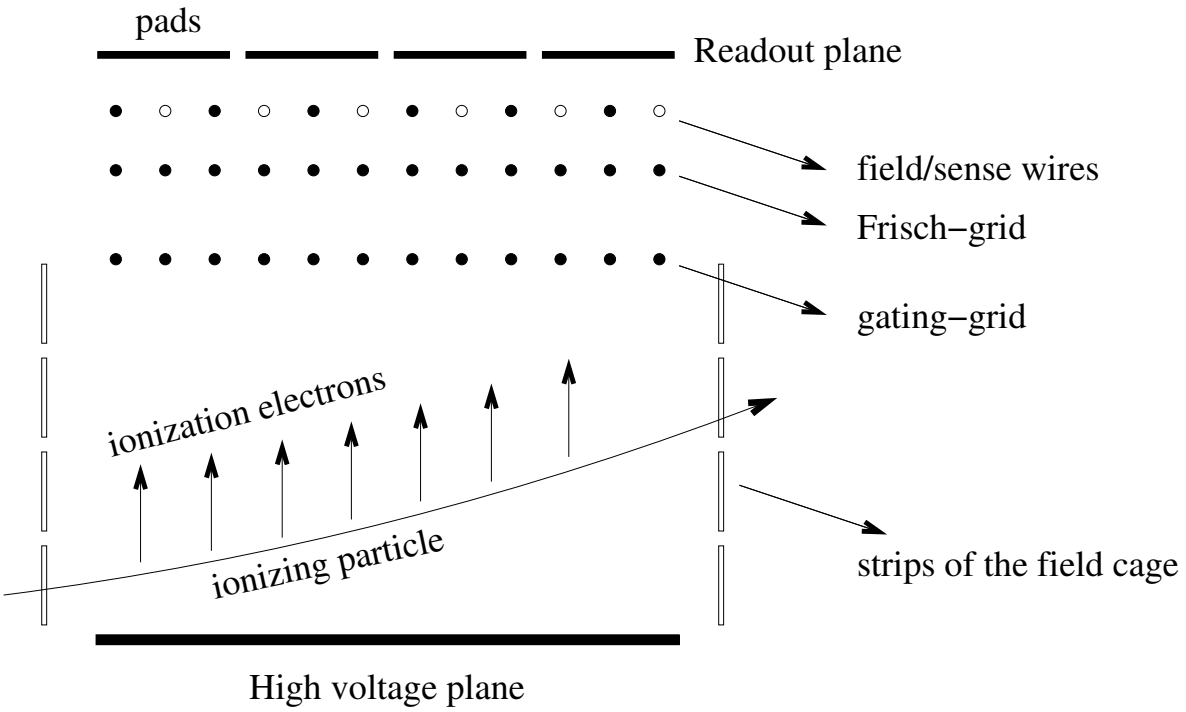

Figure 2.3: Operation of the TPCs

A charged particle passing through the gas volume of the TPC interacts with the atoms of the gas, and ionizes them. The ionization electrons begin to drift towards the readout plane, due to the electric field between the high-voltage plane (negative potential) and the Frisch-grid (at zero potential), which is almost homogenous. This region is called the *drift region*. The strength of this electric field is tuned such that no avalanche effect takes place in the drift region.

The sense wires are set to a positive potential. The field wires are set to zero potential and decouple the sense wires. All drift electrons, arriving from the drift region through the Frisch-grid, are collected on the sense wires. The electric field between the Frisch-grid and the sense wires is bigger than that in the drift region; in addition, since the electric force changes like $1/r$ close to the sense wires, the electrons are further accelerated here, and produce an avalanche. The electrons are collected and removed by the sense wires, and the remaining positive ions produce an induced signal in the pads of the readout plane. Each pad is read out separately.

The gating grid is used to toggle the detector between sensitive and insensitive state. During the closed state of the TPC (the default situation) the gating grid is switched to a voltage which is lower than what would correspond to its geometrical place between the high-voltage plane and the Frisch-grid, and in addition, the voltages of the wires

are alternatingly changed. In this state the electrons are captured on the wires of the gating grid (and the positive ions, which drift back from the sense wires, and have passed through the Frisch-grid without being neutralized there). The trigger signal of the experiment switches the TPC to the open state, when the potential of the gating grid is switched to a potential, which is optimized for maximum transmission of the electrons: the electric field between the Frisch-grid and the gating grid is larger or equal than the field in the drift region.

By simply reading out the pads we get the projection of the particle trajectories onto the readout plane. The third component (y coordinate in the NA49 experiment) of the points on the trajectories is determined as the product of the measured drift time of the electrons and the known drift velocity in the drift volume.

In order to make the electric field as homogenous as possible, a field cage is constructed around the drift volume. The strips of the field cage are connected to a resistor chain. Their potential is linearly changing with their position, fixing the boundary conditions for a homogenous field in the drift volume.

2.3.2 Construction

The basic concepts of the construction of a TPC have been discussed in the previous section. Here we discuss the more specific details of the TPCs of the NA49 experiment. There were several requirements to consider at their design:

- The Pb ion beam should not be allowed to pass through the detector because of its very large amount of ionization. Therefore the two Main-TPCs are placed on two sides of the beam, leaving a gap between them. Each vertex-TPC is also divided into a left and right part, with a 20 cm gap between the two halves. The beam passes through this gap, and though it does ionize the gas here, the charges soon recombine, since there is almost no electric field here to separate the charges. The left and right halves have their own field cage.

- In order to minimize multiple scattering and secondary interactions there should be as little material in the space region, where particles traverse, as possible. However, the detector should be mechanically stable, and its position has to be known to a very high accuracy. The walls of the TPCs were chosen to be 125 μm thick mylar

foils; the field cage is constructed from aluminized mylar strips suspended from ceramic posts at the edges.

- The drift velocity and the diffusion during the drift depend on the gas mixture, which therefore has to be controlled. It is also very essential, that there should be no components of the gas mixture, which have high electron-affinity (like oxygen): they cause an absorption of the drift-electrons in the sensitive volume. In order to maintain gas purity and avoid diffusion of oxygen into the gas volume through the walls, the walls of the TPCs are a double layer of mylar foil. The gap between the two layers is continously flushed with nitrogen. The filling gas of the VTPCs is a mixture of Ne/CO_2 (90:10). MTPCs are filled with a mixture of $Ar/CH4/CO_2$ (90:5:5).

- At NA49 the pads of the readout planes are grouped in rows, called *padrows*. In the case of VTPCs, padrows are parallel to the x axis; but in order to optimize the geometry, the directions of pads within the padrow are not perpendicular to the direction of the padrow. They are positioned parallel to the most probable direction of tracks passing over that point. For the MTPCs, the padrows and the pads within the padrows are perpendicular, but the whole TPCs are rotated by ± 0.98 degrees.

VTPC-1 and VTPC-2 are placed into a strong magnetic field of two superconducting magnets. The maximum bending power of the magnets is 9 Tm at currents of 5000 A. The standard magnetic field settings for data-taking are 1.5 and 1.1 T, respectively. The magnetic field map was measured on a three-dimensional grid with $4\times4\times4$ cm steps using Hall probes. Momentum determination is possible in these detectors by measuring the curvature of tracks in the known magnetic field. Since the VTPCs are close to the target, the track density here is substantially higher than in the MTPCs, and the determination of the specific energy loss of particles (used for particle identification, see section 3.2) is also less accurate. According to the number of padrows in both VTPCs, the maximum number of measured points of the traversing particle tracks is 72+72 in the magnetic field.

MTPCs are placed in a magnetic field free region. These detectors have to deal with a lower track density. The MTPCs extend the measured track length (by max. 90 points). They contribute to a more reliable particle identification based on the specific energy loss (dE/dx) measurement: not only by increasing the number of measured points, but also by a better dE/dx resolution.

2.3.3 Readout Electronics and DAQ

The readout signals of the pads of the TPCs are sent to the Data Acquisition (*DAQ*) through the *Front-End cards* and *Control and Transfer* boards (CT). The Front-End cards have two chips for signal preamplification, and two chips for signal shaping. Each chip has 16 electronics channels, therefore one Front-End card can serve 32 pads.

After the electronics receives an event trigger, it begins to measure the pad signals for 50 μs. This time period is divided into 512 time buckets. The amplitude of the signal is measured in each time bucket, and is digitized using an ADC. Regarding that there are about 180000 electronics channels, each having 512 time buckets, this is a huge amount of data.

Each CT board is connected to 24 Front-End cards, and supplies them with power. CT boards provide the signals for controlling the chips on the Front-End cards, and transmit so-called "house-keeping" data like board-identification, event number, etc.

2.4 The Time of Flight Detectors

Particle identification is carried out using the specific ionization of the observed particles in the TPCs (see section 3.2, figure 3.2). In the crossing region of the Bethe-Bloch curves (800 MeV $<\ p\ <$ 4 GeV) the particle identification using only dE/dx is impossible. Additional information is required for particle identification. The time of flight walls (TOF-GL, TOF-GR, TOF-TL and TOF-TR) consist of scintillators (read out by photomultiplier tubes), which measure the time of flight of the particles between the target and the wall. The momenta of the particles are measured by the TPCs. Using the measured the time of flight as well one can calculate the mass of the particle. This (in addition to the dE/dx information of the TPC-s) can be used for an improved particle identification.

The walls TOF-TL and TOF-TR cover a total surface of about 2 m^2; they were constructed by the Marburg and Dubna group of the experiment. The other two walls (TOF-GL and TOF-GR) were designed and built by the Budapest group. For a more detailed description of them see [22].

2.5 The Ring Calorimeter and Veto Proportional Chamber

The Ring Calorimeter (RCAL) is placed downstream from the Main TPCs. It has a twofold task: detect

- neutral particles (photons, neutrons, kaons, which are not detected in the TPCs, and not bent in the magnetic field)
- fast charged particles, which were not bent by the magnetic field enough to go through the TPCs, but passed through the gap between the left and right detectors

Since the calorimeter can not differentiate between charged and neutral particles, a new detector (Veto Proportional Chamber, VPC) was built and placed in front of the calorimeter. Charged particles are identified by matching hits in the calorimeter and the VPC. Neutral particles are identified by a hit in the calorimeter, and no hit in the VPC. For a more detailed description of the Ring Calorimeter and the Veto Proportional Chamber we refer to [23].

Chapter 3

The NA49 Software

3.1 The Reconstruction Software

The vast majority of data originates from the TPCs. One has to keep in mind, that the different TPCs (Main-TPC and Vertex-TPC) have different construction (rotated or not rotated pads, etc), and they operate under different conditions: Vertex-TPCs are placed within a magnetic field, and are exposed to a high flux of particles; Main-TPCs have no magnetic field. Moreover, there are other detectors like the TOF-walls, Ring Calorimeter, etc, which have a completely different structure (which is reflected in the data structures as well). Due to this complexity the reconstruction software can't contain a single scheme or procedure; it will necessarily be rather complex.

Since such a huge software can't be written by one person, there are naturally several contributions from different people, who favor different programming languages (`Fortran`, `C` or `C++`). The software environment must therefore be quite flexible, allowing separate, specific programs (dedicated for a certain detector or task) to be written in different languages, which communicate through a common protocol. The NA49 reconstruction scheme is organized as follows:

- The data are organized in structures. These objects represent logical units (like space-points, tracks, etc). Relationships (like *point of a track*) are expressed with pointers (the track structure has a pointer to the linked list of its points). These structures are the common interface between the separate reconstruction programs.
- A program (called *server*) is started, which loads the data into its memory, and takes care of memory management, etc.

- The separate reconstruction programs (dedicated for a specific purpose), which are called *clients*, connect to the server, one after the other. They can access the objects in the server's memory, read the information they need, and modify the existing structures, or create new ones.
- At the end of the reconstruction of an event, the objects stored in the server's memory are written out to a file.

In the following sections those steps of the reconstruction chain are described, which are relevant for the V^0-finding. Since in the framework of this thesis a new reconstruction software for V^0s has been developed, V^0-finding (which is the last step in the reconstruction chain) will be discussed in a separate chapter (4). In order to visualize the structure of the reconstruction software of NA49, the different clients described in the next subsections are represented in a block diagram shown in figure 3.1.

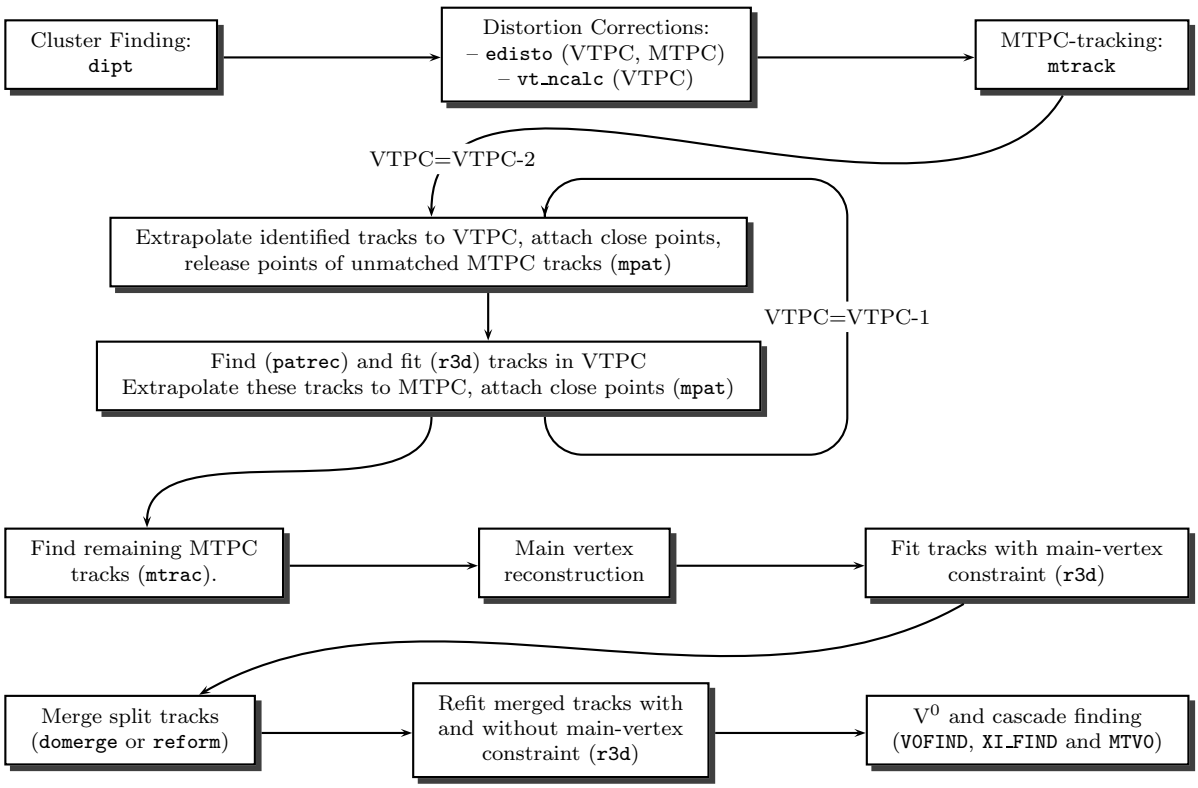

Figure 3.1: The schematic structure of the reconstruction software of NA49

3.1.1 Cluster Finding

During the drift in the chamber, the charge from the ionization diffuses, resulting in a cluster of charge extending over several adjacent pads and time bins. The signal of

each pad in the TPCs is recorded with 10 MHz sampling frequency into 512 time bins, corresponding to the maximum drift time of 50 μs. In each time bin the measured signal height is digitized with analog-to-digital converters (ADCs).

Cluster-finding is carried out padrow-by-padrow, in a two-dimensional plane (pad-direction [x-coordinate] and time-direction [y-coordinate]) by the `dipt` client. Only bins with a signal over a threshold are considered. The position of a cluster is found by center-of-gravity formation over the charge distribution. The maximal ADC count in the cluster, and the sum of the ADC counts (total ADC count) are also stored for each point, which can later be used for dE/dx analysis.

Distortion Corrections

Using the geometry database of the experiment and the drift-velocity information in the TPC, the clusters could directly be transformed into three-dimensional space points. However the charge detected at the readout plane might not originate from a space-point being vertically below the center of the detected cluster. This is caused by so-called distortion effects, which influence the path of the drifting electrons. These effects include the inhomogeneity of the electric field near the sense wires (in both VTPCs and MTPCs) and the so-called $\vec{E}\times\vec{B}$-effect in the VTPCs, the latter being the largest. They are corrected by the `edisto` and `vt_ncalc` clients, respectively.

The Lorentz-force acting on a charge q in an electromagnetic field is $\vec{F} = q(\vec{E}+\vec{v}\times\vec{B})$, where $\vec{v}$ is the velocity of the charge, and $\vec{E}$ and $\vec{B}$ are the electric and magnetic fields, respectively. If the $\vec{E}$ and $\vec{B}$ fields are parallel and point into the y direction ($\vec{E}\times\vec{B} = 0$,) a charge being initially at rest will also move into the y direction, and the Lorentz-force will have no perpendicular component to the direction of its motion. If however $\vec{E}\times\vec{B} \neq 0$, the path of the moving charge will be deflected from a straight vertical line. The $\vec{E}\times\vec{B}$ effect is most pronounced near the edges of the VTPCs, where the magnetic field is not parallel to the y axis.

In order to get rid of these distortion effects, correction tables are used. These tables are calculated by following an imaginary electron backwards from the point of detection in small steps using numerical methods, using the $\vec{E}$ and $\vec{B}$ fields at each point. The true position of the space-point is reached after the measured drift time has elapsed.

3.1.2 Tracking and Momentum Fit

The tracking procedure of NA49 has been designed for use in the high-multiplicity environment of heavy ion collisions. As a global remark the tracking software can be characterized as proceeding from the easier parts of the space covered by the detectors (from the most downstream located, lower-multiplicity region of the MTPCs, where there is also no magnetic field) towards the more difficult parts (VTPC2 and then VTPC1).

In the MTPCs the track density is lower, and due to the absence of a magnetic field, the particle trajectories are straight. Tracking in the MTPCs is carried out by the `mtrac` client: points from neighboring padrows are grouped, which point roughly in a backward-forward direction. A straight line is fitted to them, and this line is extrapolated to neighboring padrows. Points being close enough to this line are attached to the track, and the straight line is re-fitted. The track segments reconstructed in the MTPCs, which prove to be compatible with the assumption that they originate from the main vertex, are assigned a momentum with this additional constraint (*vertex-constraint*).

In the following step the MTPC tracks are extrapolated into VTPC2, and clusters close to these predictions are attached to the tracks (`mpat`). The clusters of those MTPC tracks, which have a predicted but not identified segment in VTPC2, are released for a second go of tracking.

Then all the remaining tracks in VTPC2 are reconstructed by the client `patrec`. This uses a helix model for the tracks (a straight line in the $y - z$ plane, and a circle in the $x - z$ plane). Since the magnetic field within one VTPC is more or less uniform, and the energy loss and multiple scattering do not have a large effect, this model gives a good approximation of the trajectories for track finding. These newly identified tracks are assigned a momentum by the momentum-fit module `r3d` (see section 3.1.3). These tracks are then extrapolated to the MTPCs, and clusters along these predictions are attached to the tracks.

VTPC2 and MTPC tracks are extrapolated to VTPC1, and clusters along these predictions are collected and attached to the tracks. The clusters of those MTPC tracks, which have a predicted but not identified segment in VTPC1, are released.

Then all remaining tracks in VTPC1 are reconstructed by `patrec`. These tracks are assigned a momentum by `r3d`, and are extrapolated to the MTPCs. Clusters along these predictions are attached to the tracks.

As the final step, all remaining tracks in the MTPCs are searched. After all tracks have been reconstructed, their momentum is fitted again by `r3d`.

3.1.3 The Momentum Fitting Procedure

During the tracking procedure described above the track segments identified in the TPCs were assigned a momentum, using a fitting procedure and the precise magnetic field map in the detectors. This section describes this procedure.

Based on the detailed magnetic field map, the trajectory of a charged particle starting from a point $\vec{x}$ with momentum $\vec{p}$ can be calculated using the Runge-Kutta algorithm [73]. During the local momentum fit, `r3d` carries out a 5-parameter fit using the Levenbergh-Marquardt procedure [73], the 5 parameters being the x and y coordinate of the starting point at the z coordinate of the first measured point of the track, and the 3 momentum components ($\vec{p}$) of the track at this point. The quantity to be minimized is

$$\chi^2 = \frac{1}{2N-P} \sum_i^N \left\{ \log\left(1 + 0.5 \cdot \Delta x_i^2\right) + \log\left(1 + 0.5 \cdot \Delta y_i^2\right) \right\} \tag{3.1}$$

where $\Delta x = (x_i^{\text{meas}} - x_i^{\text{pred.}})/\sigma_i^x$ is the deviation between the measured x coordinate of the ith point (x_i^{meas}) and the predicted x coordinate for the same point ($x_i^{\text{pred.}}$), divided by σ_i^x, the error of the x coordinate of the ith measured point.

A momentum with a *vertex constraint* (when the particle is assumed to originate from a vertex with fixed coordinates) can also be determined: in this case the fit has only 3 parameters, the momentum components of the particle at the vertex position.

3.1.4 Main Vertex Reconstruction

The primary interaction point (*main vertex*) is determined from the detected tracks. They are extrapolated upstream towards the target, and a 3-parameter fit is carried out, the 3 parameters being the 3 coordinates X, Y and Z of the main-vertex. The quantity to be minimized is

$$\sum_i \log\left(1 + \frac{1}{2} \cdot \frac{\left(X - x_i(Z)\right)^2}{\sigma_x^2}\right) + \log\left(1 + \frac{1}{2} \cdot \frac{\left(Y - y_i(Z)\right)^2}{\sigma_y^2}\right)$$

where $x_i(Z)$ and $y_i(Z)$ are the x and y coordinates of the ith extrapolated track at the z-coordinate Z, and σ_x and σ_y are numerical parameters (their value for p-p data were 0.22 and 0.35, respectively).

After the determination of the main vertex position, all global tracks are re-fitted by `r3d`, using the *main-vertex constraint* (that is, with the assumption that the tracks originate from this point). Tracks which do not seem to be compatible with this assumption (where the fit gives a too high χ^2) are flagged. The momentum of the tracks resulting from this fit does not replace the momentum obtained without the main-vertex constraint: both are stored (note that for V^0 finding, where the daughter tracks do not originate from the primary vertex, the momentum determined without the main-vertex constraint must be used).

3.1.5 Track Merging

After the main vertex determination the last step of the tracking procedure is carried out in order to avoid the presence of *split tracks* (unmatched track segments belonging to the same physical particle). The `domerge` client was developed to work in the high-multiplicity environment of heavy ion collisions. The `reform` client was developed to carry out a very accurate matching procedure in the lower-multiplicity environment of proton-nucleus or proton-proton collisions. If track segments have been matched in the last step, their momentum is re-fitted.

3.2 Particle Identification: Specific Energy Loss

Many experiments in the early times were able to detect the particles produced in the interaction, and accurately measure their momentum – but they were not able to identify the particles. Particles were *assumed* to be pions or protons (whatever the analysis wanted to study). In modern experiments particle identification is possible. The most widely used method is to measure the specific ionization (dE/dx) of the particles. This method is used also in the NA49 experiment, and will be shortly described here. dE/dx calibration is carried out differently for p-p and Pb-Pb reactions. For p-p reactions it is not part of the reconstruction chain – it is carried out after the large amount of data collected during a measurement period is reconstructed.

Charged particles traversing the active volume of the detectors interact with the gas via the Coulomb interaction, and ionize the gas molecules. The specific energy loss (or the amount of ionization) per unit path length is only a function of the velocity and charge of the particle (and of course the properties of the material) [18]:

$$\left\langle -\frac{dE}{dx} \right\rangle = \frac{2\pi N e^4}{m_e c^2 \beta^2} z^2 \left(\ln \frac{2 m_e c^2 \beta^2 \gamma^2 E_{\max}}{I} - 2\beta^2 - \delta \right) \tag{3.2}$$

where π is a universal constant (π=3.1415...), c is the speed of light, m_e is the electron mass, e is the electron charge, z is the charge of the traversing particle expressed in units of e, N is the number density of electrons in the material, I is the average ionization energy of the material and $E_{\max}$ is the maximum energy transfer from the traversing particle to an atomic electron. $\beta = v/c$ and $\gamma = 1/\sqrt{1-\beta^2}$, where v is the velocity of the particle. The last two terms in (3.2) are introduced to describe the screening of the Coulomb interaction by the polarization of the medium.

In practice it is much more important to have an easily treatable parametrized formula, which can be tuned via its parameters to the measured data [21]. In NA49 the following formula was used to describe the measured ionization of particles:

$$\left\langle -\frac{\mathrm{d}E}{\mathrm{d}x} \right\rangle = E_0 \beta^{\alpha} \left(b + 2\ln(\gamma) - \beta^2 - \delta(\beta) \right) \tag{3.3}$$

where the δ term includes several other parameters as well. The parameter values for the use of this formula were provided by collaborators, who did the whole calibration of the dE/dx measurement in the TPCs in the proton-proton data [21].

The *momentum* of the particles traversing the detectors (the VTPCs) is determined from the track curvature. The specific ionization is related to the *velocity* of the particle. These two information can be used to identify the particle – i.e. to estimate its mass. In practice one expresses the Bethe-Bloch formula (3.3) as a function of momentum and mass, using the following substitutions:

$$\beta = \frac{\beta\gamma}{\sqrt{1+\beta^2\gamma^2}} = \frac{p/m}{\sqrt{1+(p/m)^2}} \tag{3.4}$$

$$\gamma = \sqrt{1+\beta^2\gamma^2} = \sqrt{1+(p/m)^2} \tag{3.5}$$

and finally we obtain

$$\left\langle -\frac{dE}{dx} \right\rangle = B(p/m) \tag{3.6}$$

If one takes the mass m as a parameter, one obtains a universal expression of the specific ionization as a function of momentum. Plotting these curves as a function of momentum p (on a logarithmic p-axis) for different particle species (that is, with different mass parameters), one obtains several curves with the same shape, which are shifted along the horizontal axis, as shown in figure 3.2.

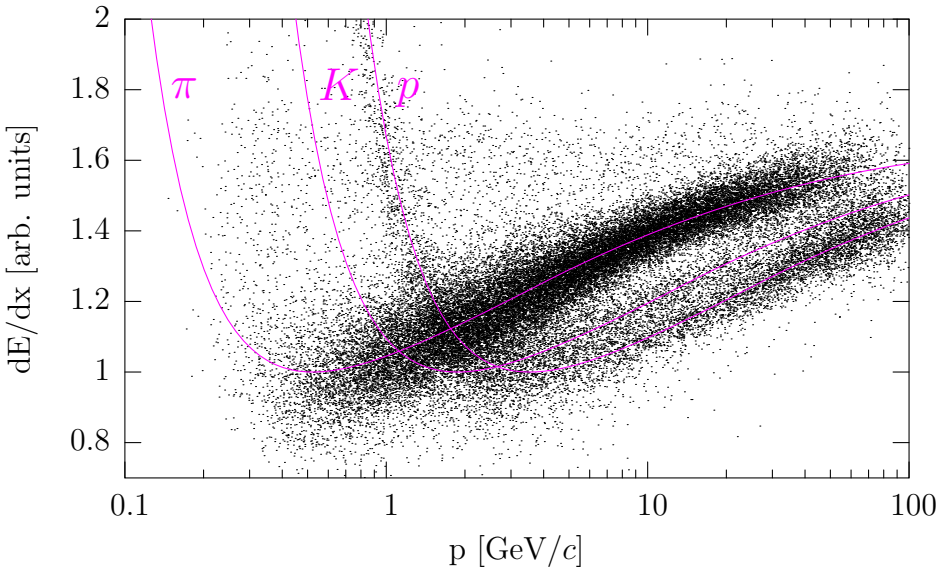

Figure 3.2: The curves describing the specific ionization of different particle species as a function of momentum, together with the detected particles.

For each point of a track the total ADC and maximum ADC counts are stored in the datafiles (see section 3.1.1). These numbers are used to determine the specific ionization of the particles. (The calibration and the calculation are rather complex procedures. For more details we refer to [21]). In figure 3.2 the detected particles are also shown: each point on the specific-ionization vs. p plane corresponds to a particle. The points clearly accumulate around the predicted curves. By selecting a momentum bin and fitting the dE/dx distribution in that bin one can determine the inclusive particle yields; by making a cut around the parametrized Bethe-Bloch curves one can select individual particles of a certain species (the contamination by other particle species, and the number of accepted particles by this cut depend on the tightness of the cut).

3.3 Simulation

In order to account for losses due to the non-complete acceptance of the detectors and estimate the efficiency of the reconstruction software, a full simulation of the machinery is needed.

The high-multiplicity environment of heavy ion collisions is different from proton-proton (or proton-nucleus) collisions. Due to that, there are different approaches how one carries out the simulation.

- In heavy ion collisions a track can not be treated separately: the signals of closely passing particles can interplay, and the reconstruction efficiency of a track depends on its environment. Therefore in heavy ion collisions (in order to produce the most realistic environment) the most common way of simulation of the detection/reconstruction is to take real events, and embed simulated particles into these events.

- In the low-multiplicity proton-proton collisions the detection/reconstruction efficiency of single particles is independent of the event-configuration. In this case one can either emit and simulate single particles, or take an event generator (like VENUS [76], FRITIOF [77], etc), which provide event configurations according to some physical models, and process all the particles from the generated events through the simulation chain

In the framework of this thesis proton-proton events were analyzed, therefore the second approach has been used. The reconstruction efficiency in the low-multiplicity environment is indeed independent from the event topology. However in proton-proton collisions (in order to exclude background events[1]) different cuts had to be applied on the reconstructed main vertex (this will be described later, in section 5.2.2). In order to study the effects of these cuts with simulation as well, complete events were simulated and processed through the GEANT [75] detector simulation tool. The simulation chain can be divided into the following steps:

[1]Interactions of the beam particle occurring outside of the target

- Generate events with an event generator
- Simulate the passage of particles through the materials of the detectors using the GEANT simulation tool. This software follows the particles in the matter (which might happen to be in electric or magnetic fields: in this case tracking is carried out using the magnetic field map), calculates the probabilities of different interactions, decays or secondary particle production (unstable particles are decayed isotropically in their rest frame). If a particle has decayed, or produced secondary particles by some interaction, its daughters are followed.
  Some volumes in the detectors are designated as sensitive volumes, and particles transported through these volumes leave hits; the coordinates of the hits are stored. The ionization charge produced in the gas volume of the TPCs is not followed by GEANT. The Monte-Carlo points of the tracks in the TPCs are determined as the track's coordinates vertically below the center (along the z axis) of a padrow.
- Due to the $\vec{E} \times \vec{B}$ effect, the drift path of the ionization charge towards the readout plane is more complex than a simple projection (see section 3.1.1). This can have the effect, that charge deposited geometrically below the readout plane may drift outside, and vice versa. Knowing where the particles pass through the detectors (the Monte Carlo points), a client called `MTSIM` simulates the response functions of the pads in the TPCs (including the distortions due to the $\vec{E} \times \vec{B}$-effect and the distortions of the electric field). Information about matching Monte Carlo points and signal-clusters is stored in order to make the matching of Monte Carlo and reconstructed tracks later possible.
- The whole data is processed through the same reconstruction chain, which is used to reconstruct the real data.
- Monte Carlo and reconstructed tracks are matched.

The structure of the simulation software of NA49 is represented in figure 3.3

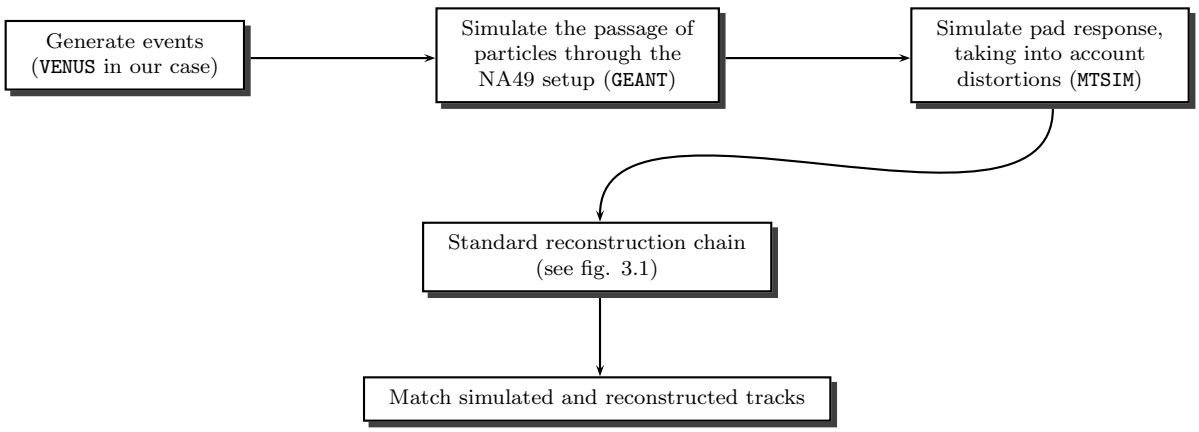

Figure 3.3: The structure of the simulation software of NA49

Chapter 4

V^0 and Cascade Finding

Strongly decaying resonant states (like Δ, N etc. resonances) have a very short lifetime, therefore they essentially decay at the primary interaction point: their decay vertex can not be separated from the primary vertex. To observe these states one usually applies the invariant mass method: all proper track pairs are formed, and their invariant mass is calculated. A peak is visible above the background at the nominal mass of the resonance (if it is produced in the interaction).

Weekly decaying particles (Λ^0, Ξ^0, Ξ^-, Ω^-, K^0) have a much longer lifetime ($c\tau$ = 7.89, 8.71, 4.91, 2.46 and 2.67 cm, respectively). Their decay vertex is usually displaced from the primary vertex.

Because Λs and K^0s are neutral, they leave no track in the detector – even if they travel several meters before they decay. These particles are called V^0-s, because of the characteristic V shape of their two charged daughters ($\Lambda \to p\pi^-$ with a branching ratio of 63.9%, $K^0_S \to \pi^+\pi^-$ with a branching ratio of 68.6%). These particles have to be reconstructed from their daughters.

Though Ξ^- and Ω^- particles are charged, at these energies they don't live long enough to be detected in the detectors (remember the large gap between the two halves of the VTPCs, and that the target is located approximately at $z = -580$ cm, and VTPC1 starts only at about $z = -500$ cm). They also have to be reconstructed from their daughter particles. This procedure is a bit more complex than that for the V^0s: Ξ^- and Ω^- decay into a Λ^0 and a π^- or K^-, respectively. Therefore they are often referred to as *cascades*.

There has been a reconstruction software in the NA49 experiment for many years (`VOFIND` and `XI_FIND`). In the framework of this thesis a new method was developed

(called MTVO), at that time with the main goal in mind to explore such configurations, and such regions of momentum space, which could not be used with the original method. To fully understand the motivations for such a big ("duplicated") work, we first describe the original method in section 4.1. The new method will be detailed in section 4.2.

The complex detectors and reconstruction software in today's particle physics experiments are a large source of errors or uncertainties. Results from an experiment are usually compared to the *world average* in order to get convinced about absolute normalizations, etc. Since many of the results presented in this thesis are first measurements, such a comparison could not be done in our case. In order to check the reliability of our results, and since MTVO proved to be a reliable method to be applied over the whole momentum region, it was finally used as a completely independent finder. During the analysis of our proton-proton data sample, results of MTVO and VOFIND were produced parallel (The VOFIND analysis was carried out by Tatjana Šusa). Differences between the two results were indeed useful to discover and correct errors in either analyses. The final results were derived as a combination of these two independent results.

4.1 The Original Methods

VOFIND was designed to be used in the high-multiplicity environment (about 1500 particles per collision) of heavy ion collisions. Such an environment has rather different requirements from those in a low-multiplicity proton-proton collision. For example, due to the huge combinatorics in a high-multiplicity environment, much tighter cuts have to be applied in order to produce a better signal/background ratio, and decrease the computation time (V^0-finding and fitting takes an essential fraction of the computing time for one event), and the data volume.

Since this thesis deals with results from proton-proton collisions, therefore here only those cuts for VOFIND will be presented, which were used in the proton-proton analysis. Since in proton-proton collisions the data volume, computing time and the combinatorial background are a much smaller problem, the policy here was to use as loose cuts as possible.

4.1.1 V^0 Reconstruction

V^0 and cascade finding is the last step in the reconstruction chain. It takes place, when all global tracks have been reconstructed and fitted. The basic idea is to extrapolate

pairs of tracks (one positive and one negative) upstream, and look for a closest approach of them (see figure 4.1). Tracks are extrapolated in the z-direction with 2 cm steps, and their distance in x and y directions is calculated. If there are 3 consecutive points, where the distance between the two tracks is smallest at the middle point, then the distance of closest approach must have occurred somewhere between the 1st and 3rd point. An interpolation is used to estimate the real point of closest approach [20,19].

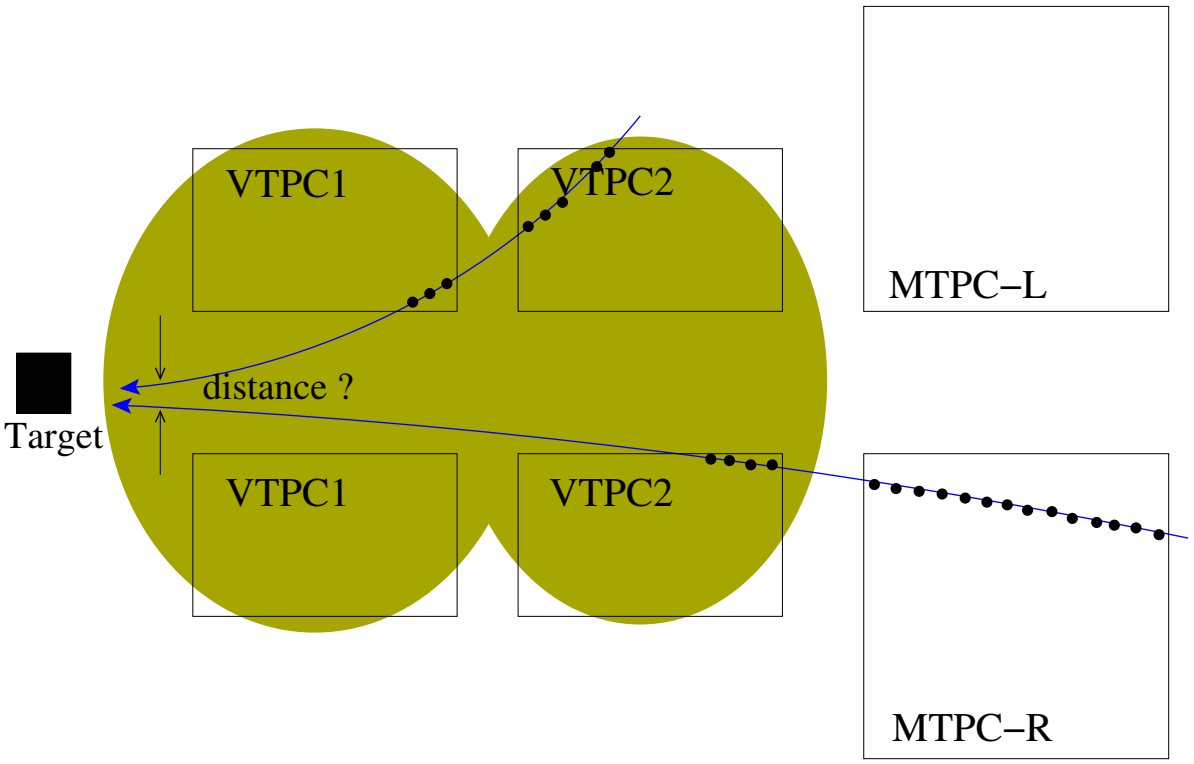

Figure 4.1: The `VOFIND` method. The shaded area represents the magnetic field (figure is not to scale)

If their distance of closest approach (DCA) is less than 1 cm in both x and y directions, the pair is accepted as a V^0-candidate. These candidates are then subject to further quality cuts and a fitting procedure (`VO_FIT`). Quality cuts right after the finding stage are essential in order to reduce the computation time spent in the fitting stage.

After the candidates have been identified, a geometrical fit is preformed on these V^0-candidates by the client `VO_FIT`. V^0s are fitted with a nine-parameter Levenberg-Marquardt fitting procedure [73], the nine parameters being the three coordinates of the decay vertex, and the momentum components of the two daughters at the vertex.

4.1.2 Cascade Reconstruction

Cascade (Ξ^-, Ω^-, $\overline{\Xi}^+$, $\overline{\Omega}^+$) particles decay into a V^0 (Λ^0 or $\overline{\Lambda}^0$) and a charged particle (π^-,K^-,π^+ or K^+ respectively). Cascade-finding is done by the client `XI_FIND`, and is similar to V^0-finding: all suitable V^0s are combined with charged tracks. Only those V^0s are used, which appear to be a Λ or $\overline{\Lambda}$ (using their invariant mass). Furthermore only negative tracks have to be combined with Λs, and only positive tracks have to be combined with $\overline{\Lambda}$s.

Both the $\Lambda(\overline{\Lambda})$ and the charged track are extrapolated upstream towards the target in 2 cm steps, and their distance calculated in both x and y directions; the extrapolation of the lambda is quite easy: its trajectory is a straight line. Again: if a minimum in the distance is observed, and this distance of closest approach is less than 1 cm in both directions, the V^0 and the charged track is accepted as a cascade candidate. There is no fitting of the cascade particles.

4.1.3 Limitations

The class of V^0s or cascades, which can be reconstructed by `VOFIND` and `XI_FIND` is determined also by the applied cuts during the reconstruction (and later). These cuts will be described in a later section, and here we only concentrate on the limitations of this software originating from its construction, which were originally the main reason to write `MTVO`.

Since `VOFIND` and `XI_FIND` extrapolate tracks in the magnetic field from their measured segments into such regions, where they were unseen, all tracks used in the analysis must necessarily have a fitted momentum. If a track for some reason has no fitted momentum, it is lost for this analysis:

a.) Fast tracks, which pass through the gap between the left and right halves of the vertex-TPCs, and are detected only in MTPC-L or MTPC-R (mtpc-only tracks). Their detected segment in the MTPC is straight, and their momentum can be determined only with the additional assumption, that they originated from the primary vertex.

b.) Low-momentum tracks have a high curvature in the magnetic field. As it turned out in a short study, the momentum-fit module `r3d` often fails on these tracks, and therefore they are also lost for V^0 analysis.

We expect, that the first class of tracks will be produced by fast Λs. Fast Λs can travel several meters before they decay, and since Λs are neutral, they are not bent in the magnetic field. Therefore the effective bending power of the magnetic field observed by the daughters is much smaller. In addition, due to the mass asymmetry between the two daughters of the Λ ($m_p = 0.938$ GeV, $m_\pi = 0.139$ GeV) the proton will carry most of the momentum of its parent, and will have therefore a trajectory, which is much less curved in the magnetic field. Therefore the proton has a bigger chance to avoid being detected in the VTPCs. The lower-momentum pion will be swept into VTPC-2 by the magnetic field with a higher probability. Figure 4.2 shows the decay products of a Λ with rapidity[1] in the center-of-mass system $y_{cm} = 1.2$ (simulation).

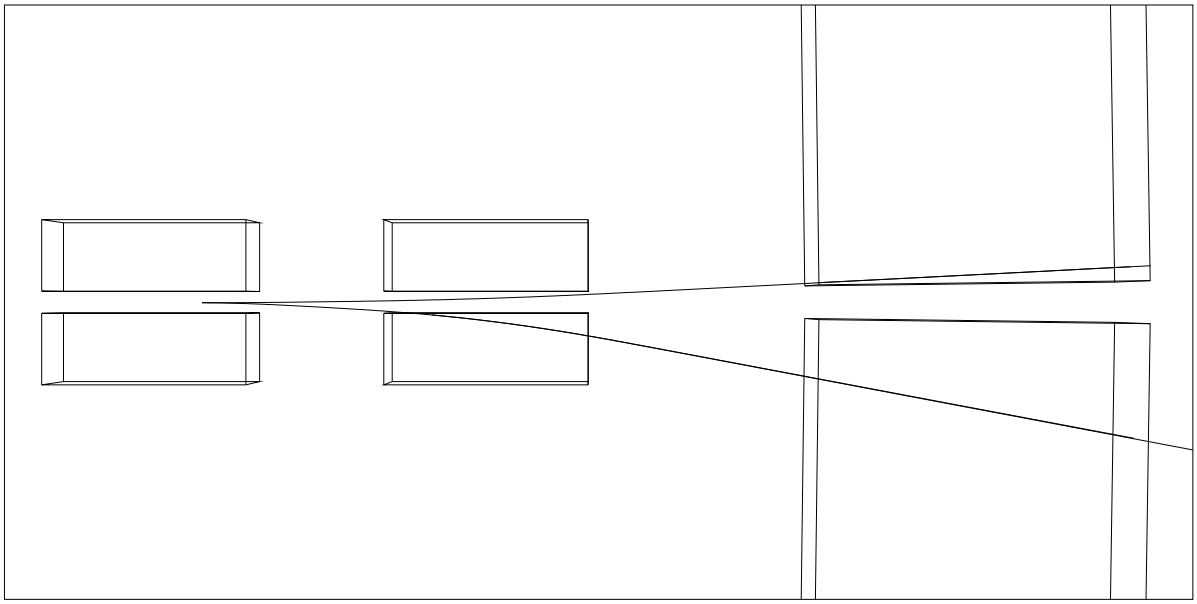

Figure 4.2: Illustration of a Λ producing a MTPC-only proton (simulation)

The second class of lost tracks (b.) is produced by low-energy V^0s in the lab-frame (fast backwards going particles in the CM-system).

A further limitation is an applied cut on the number-of-points of the daughter tracks at the reconstruction level: only tracks having more than 20 points in at least one of the VTPCs are used for the analysis. Low-momentum tracks are often so much bent by the magnetic field, that they exit the VTPCs at their side before they would leave 20 points.

Simulation studies showed, that in certain rapidity regions a large fraction of Λs produce the above two configurations. In these studies only those Λs were treated,

[1]For the definition of rapidity and other kinematical variables see Appendix B

which decayed into the charged channel, and both daughters of which were detected and reconstructed. In the case of 30% of the Λs emitted in the rapidity range -1.5< y_{cm} <-0.5 one of the daughters (the lower-momentum pion) had no momentum (the reason given by the momentum-fitting module `r3d` was that it exceeded the limit for the number of iterations during the fit). In the case of 33% percent of the Λs emitted in the forward rapidity range 0.5< y_{cm} <1.5 the proton daughter was a MTPC-only track.

4.2 The New Method

The new method for V^0-finding (`MTV0`) was developed as an attempt to use MTPC-only tracks in the V^0 analysis as well. MTPC-only tracks don't have a fitted momentum, therefore the definition of the task can be formulated the following way:

Search for V^0s without using the momentum of one of the tracks

This method would recuperate for the V^0 analysis both configurations listed in points (a) and (b) before, though the problem with the low-momentum tracks, point (b) was not yet known at that time. Such a method is a combined procedure of V^0-finding and momentum fitting at the same time. This method can of course be used also for such track-pairs, where both tracks have a fitted momentum. In this case the momentum of the "better" track (which has more points, or fulfills other requirements) is used, and the momentum of the other track is dropped and re-fitted by the method.

4.2.1 V^0 Reconstruction

If two tracks really come from a V^0 decay, and one of them has a known momentum (and therefore a known trajectory in the magnetic field), then the decay vertex has to be somewhere on this known trajectory. This constraint leaves 1 free parameter for the vertex position: the z coordinate.

There are 3 more parameters of the problem: the momentum components of the track with unknown momentum (which will be referred to as *no-momentum track* in the following, even if its momentum is known, but not used) at the decay vertex. One has to find

the best set of these 4 parameters[2] (make a fit), which give the best predicted trajectory for the no-momentum track (being close to its points). The method is sketched in fig. 4.3.

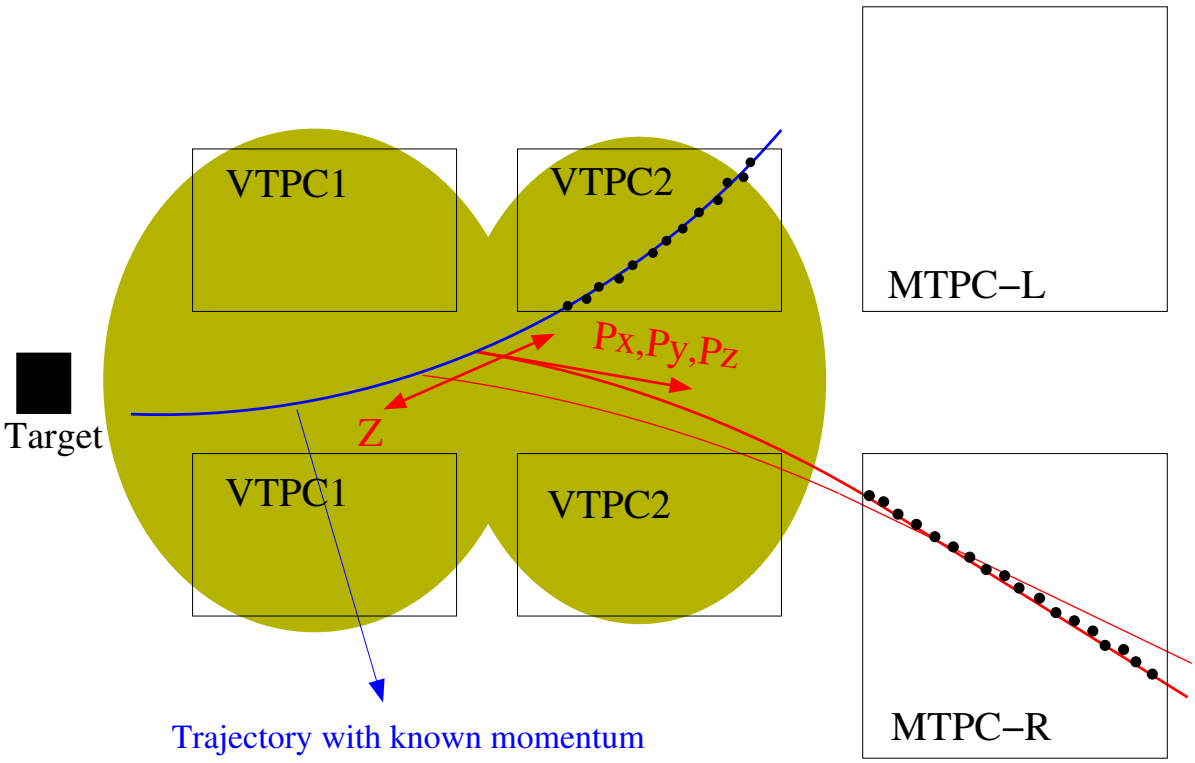

Figure 4.3: Sketch of the new V^0-finding method (top view; not to scale). The shaded area represents the region with magnetic field

The first step of this method is looking for initial values for the fit. This step uses the advantage of the magnetic field of NA49: the magnetic field is parallel to the y axis in the sensitive volume of the TPCs[3]. Therefore the projection of tracks onto the y-z plane (side view) is a straight line to a good approximation.[4] Therefore in the first step `MTV0` searches for a crosspoint of the projections of the two tracks in the y-z plane (this is an easier task than looking for a crosspoint in 3 dimensions):

[2] In practice a different set of parameters is used. Instead of p_x,p_y and p_z (the momentum components of the no-momentum track) the used parameters are: $q = Q/p_{xz}$, $t = p_y/p_{xz}$ and $\phi = \arctan(p_x/p_z)$, where Q is the charge of the particle, and p_{xz} is the component of the momentum vector in the $x-z$ plane. These parameters are much less correlated.

[3] Exceptions are the edges of the TPCs, where the magnetic field has a small horizontal component

[4] To be more precise: if we assume that the magnetic field is homogenous, and it has no B_x and B_z components, the particle trajectories are a helix around the y axis. The projection of such a helix onto the y-z plane is clearly not straight, but since the characteristic radius of the helix is large enough, the deviation from a straight line is negligible. Exceptions are low-momentum tracks, and tracks which pass through regions with a magnetic field having non-vanishing B_x or B_z components.

a.) **If one of the tracks has no momentum**: a straight line is fitted to the projection of the points of the track in the y-z plane. The other track is followed in the magnetic field (using its momentum).

b.) **If both tracks have momentum**: both tracks are followed in the magnetic field, using their momentum. If no crosspoint is found in the $y-z$ plane, then the search is repeated using method a.). (The track with less points in both VTPCs together is taken to be the no-momentum track).

Since all tracks originating from the primary vertex would have a crosspoint with one another, if we allow any z position for the crosspoint, therefore a cut is required on the z coordinate of the crosspoint: $z >$`cross_zmin` (where `cross_zmin`$=-570$ cm, see Table 4.1). Tracks are not followed more upstream than this z coordinate.

Having determined the initial value of the vertex position along the trajectory of the VTPC-track, the initial values of the 3 momentum-components of the no-momentum track are calculated in the following way:

- If the track had a fitted momentum, and the initial vertex-position has been determined by following it upstream, the calculated momentum components at this point are used as the initial values.
- If the track had no fitted momentum, or following the track using its momentum gave no crosspoint in the $y-z$ plane (so a straight line was used instead), then the momentum components p_x, p_y and p_z are set to give $p_x^2+p_y^2+p_z^2 = (30\text{ GeV})^2$, and the momentum vector (p_x, p_y, p_z) points from the initial crosspoint towards the last measured point of the track. This proved to be a useful choice of the initial parameters (being really simple, and giving a convergent fit, whenever possible).

The next step is the 4-parameter fit, the procedure being the Levenberg-Marquardt method [73]. The error function to be minimized is defined as follows:

$$\chi^2 = \sum_i^N (x_i - x_i^{\text{pred}})^2 + (y_i - y_i^{\text{pred}})^2 \tag{4.1}$$

where x_i and y_i are the x and y coordinates of the ith point of the no-momentum track, x_i^{pred} and y_i^{pred} are the predicted coordinates of the trajectory

at the same z coordinate with the current values of the parameters, and the sum runs over all points of the no-momentum track. The iteration stops if in the last step χ^2 has changed by less than 0.1% and χ^2/N (the average squared distance of the points from the fitted track) is smaller than 0.1 mm^2. The iteration also stops if the number of iterations exceeds `nstep` (=40). After the iteration has been finished, the current value of $\sqrt{\chi^2/N}$ is examined, and the candidate is rejected if it is larger than `maxres` (=0.3 cm). The candidate is also rejected, if the fitted z coordinate of the vertex is less than `zmin` (=−570 cm) (for the summary of the applied cuts see table 4.1).

4.2.2 Cascade Reconstruction

Cascade finding is done in exactly the same way. In this case the straight line of flight of the Λ (or $\overline{\Lambda}$) plays the role of the known trajectory, and the charged daughter ($\pi^{\pm}$ or $K^{\pm}$) is taken to be the no-momentum track, the momentum of which is determined by the method.

4.2.3 Outlier Removal

Many people from the collaboration have made a lot of effort to make the simulation of the detectors of NA49 as realistic as possible. The particles passing through the detectors are followed by `GEANT` [75], and the signals of the electronics are simulated, taking into account geometrical distortions due to the magnetic and electric fields. However good this simulation might be, there will always be differences between the reality and the simulation:

- Particles not originating from the primary collision (from the beam halo, or cosmic particles) pass through the detectors. They are not synchronized with the trigger, therefore they will be geometrically distorted, and present a background.
- The noise of the electronics can produce signals, which sometimes are reconstructed as space points.
- Knock-out electrons in the TPC sensitive volumes (electrons hit very strongly by the particle) can travel as much as several centimeters, and produce high ionization in the gas volume far from the track.

These situations are not described by the simulation, which provides always a much clearer picture. The data contain a lot of garbage points or tracks. As an illustration of this see fig 4.5.

This is very well reflected in the distribution of the distance of points from the fitted `rtrack`s (an `rtrack` is the data structure holding information, such as momentum components, etc, about a track fitted *without* vertex constraint) – see fig. 4.4a. The effect is even more pronounced, if we plot the distribution of the distance of the farthest points (fig. 4.4b).

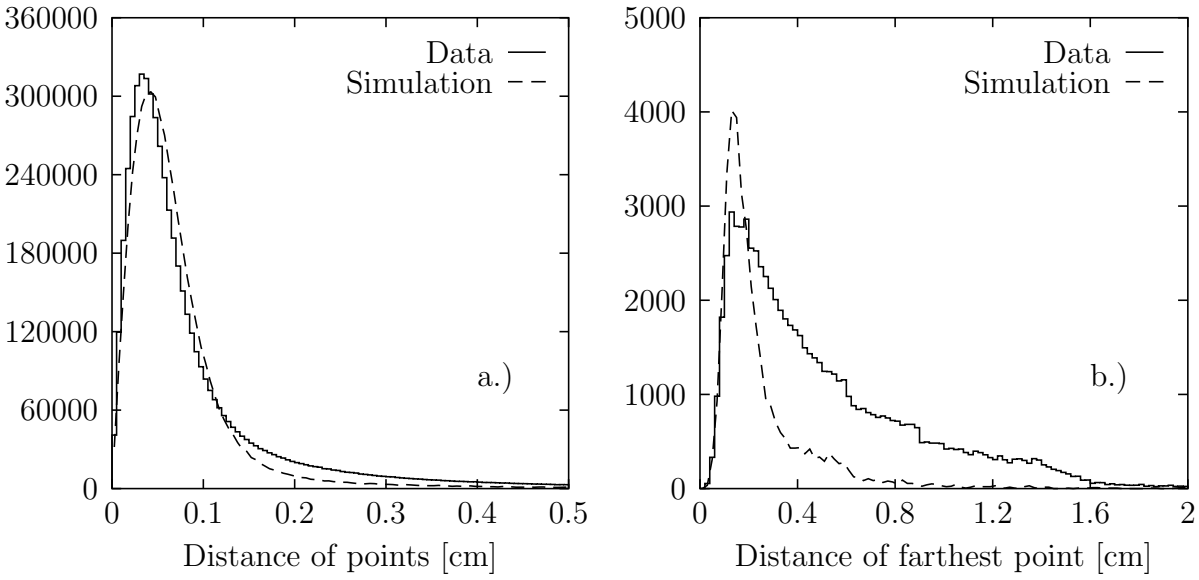

Figure 4.4: Distribution of the distance of points from the fitted `rtrack`s: a.) all points b.) farthest points

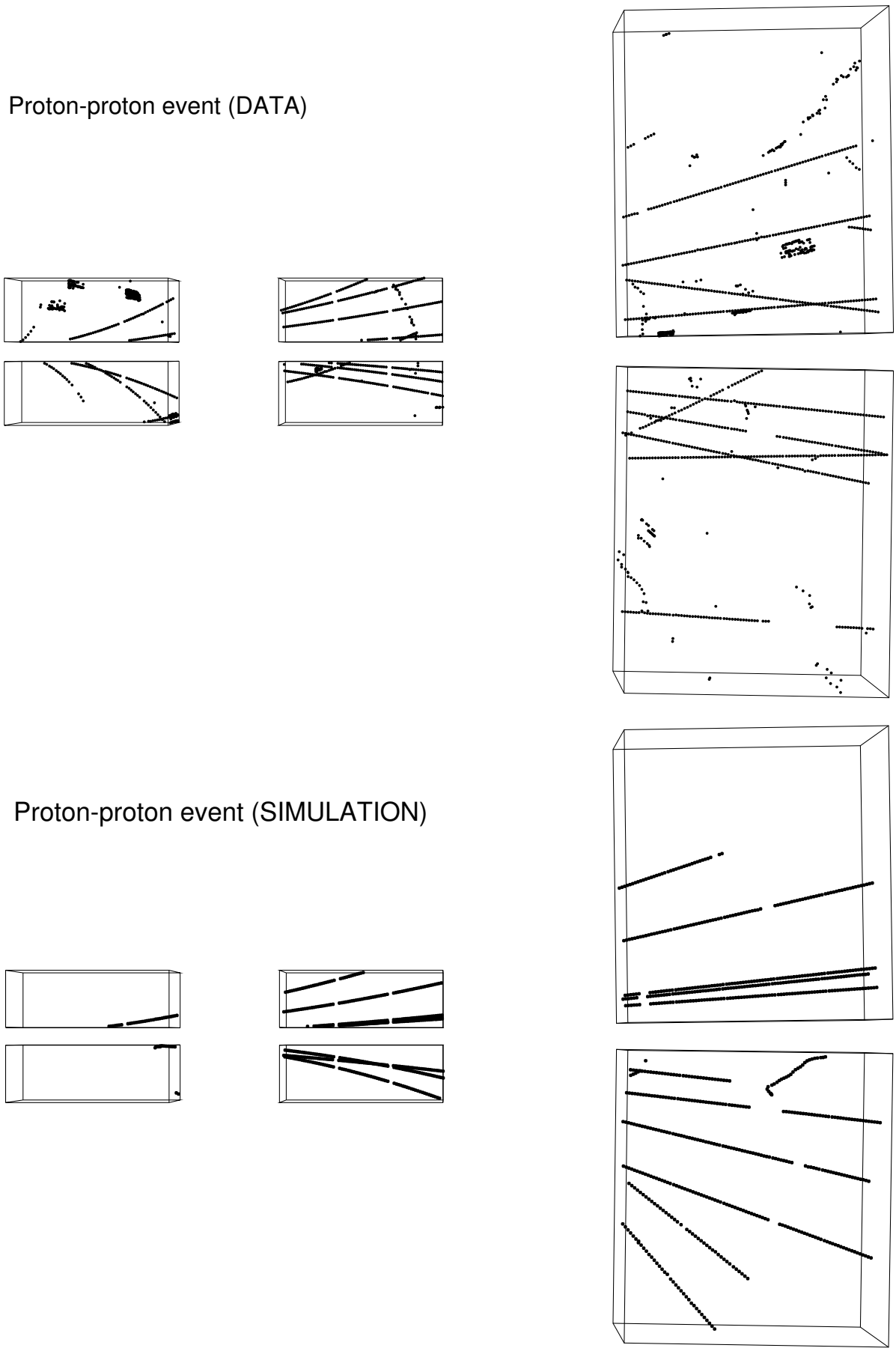

Figure 4.5: Comparison of a typical Monte Carlo event with a proton-proton event taken from the data

The long tail of this distribution clearly shows, that sometimes the tracking routines attach points to the tracks lying as far as a few centimeters. Such an outlier can pull the slope of the fitted track (especially if the outlier is at either end of the track). This will result in a worse momentum-, vertex-position- and invariant-mass resolution in the data. In the simulation – since there are no outliers – this effect is not present. In order to make our reconstruction more precise, and to bring the simulation and reality closer, these outliers have to be removed. In `MTV0` this is implemented as follows:

a.) If the track has a segment in either of the MTPCs (where the track must be straight), a straight line is fitted to the points of this segment. The point, which is the farthest from the fitted line, is removed from the list of points, and the line is re-fitted. The iteration goes on until there are no points, which are farther than a certain cut (`outl_mt_c`=0.25 cm). No more than a certain fraction (`outl_mt_f`=8%) of all points are removed (for the values of these cuts used in the reconstruction see table 4.1).

b.) Tracks, which have segments in the VTPCs, need a different procedure. The iteration of the method's fitting procedure is suspended after `nstep`/2 steps. Since the predicted trajectory at the current stage of the fit is not necessarily the "ideal" one (for example due to possible outliers), we can not use the deviations between this curve and the measured points directly. Instead, these deviations are assumed to change smoothly as a function of z: deviations are fitted with a first order polynomial in the y direction, and a second order polynomial in the x direction. The points which are farther from these lines (either in the y or the x directions) than a cut (`outl_vt_c`=0.3 cm) are removed from the list of points. No more than a certain fraction (`outl_vt_f`=8%) of all points is removed.

Figure 4.6 shows the effect of the outlier removal: the distribution of $\sqrt{\chi^2/N}$ (the average distance of the points from the fitted track) is now clearly peaking at around 0.06 cm, and the long tail is suppressed. The cut on this quantity at the reconstruction stage was set to `maxres`=0.3 cm. The reason to apply such a large value was to not loose any candidate due to this cut: as fig. 4.6 demonstrates, the same distribution in the simulation is still narrower (even after the outlier-removal in the data). Therefore if any true candidate is rejected due to this cut, the rejection rate would be different (smaller) in the simulation, leading to an overestimated reconstruction efficiency.

Cut	Description	value
`nstep`	Max. number of iteration steps (page 36)	40
`cross_zmin`	Minimum of the initial z coordinate of the vertex (before the fitting procedure). (page 35)	-575 cm
`zmin`	Min. of the fitted z coordinate of the vertex (page 36)	-570 cm
`outl_mt_f`	Max. fraction of outliers in the MTPCs to be removed (page 39)	8%
`outl_mt_c`	Outliers in the MTPCs are removed if farther than this (page 39)	0.25 cm
`outl_vt_f`	Max. fraction of outliers in the VTPCs to be removed (page 39)	8%
`outl_vt_c`	Outliers in the VTPCs are removed if farther than this (page 39)	0.3 cm
`maxres`	Upper limit for the average distance of points from the fitted track, $\sqrt{\chi^2/N}$ (page 36)	0.3 cm

Table 4.1: Values of the cuts used by `MTVO`

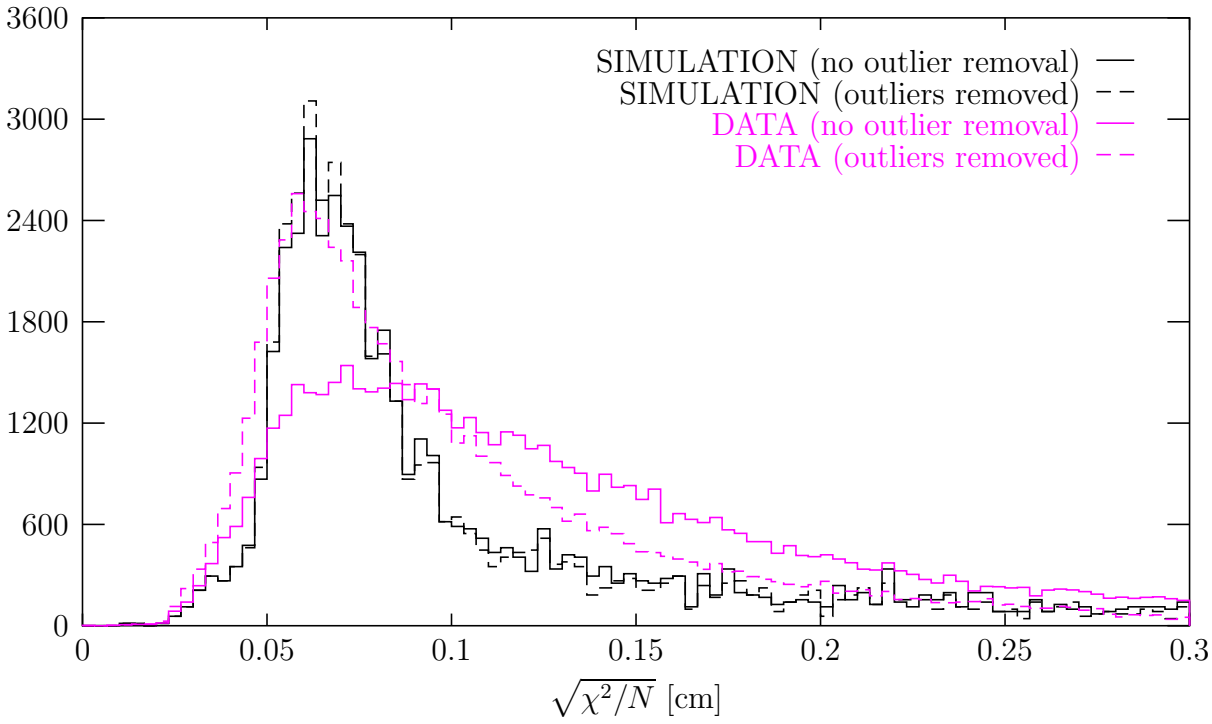

Figure 4.6: Result of the outlier removal: the average distance of the points from the track

4.2.4 Performance of MTV0

In the remaining part of this chapter we will study, how well the original goals of MTV0 are fulfilled:

- If it really succeeds to reconstruct V^0s using MTPC-only or unfitted (usually very short) tracks, and how much (and in which parts of the momentum space) we gain from its results
- If the price we have to pay for additional V^0s is acceptable (invariant-mass, momentum and vertex position resolutions)

For the studies of the performance of MTV0 reconstructed Monte Carlo events were used: VENUS-generated events (containing a particle of the studied species) were processed through GEANT and the complete reconstruction chain, as described in sec. 3.3. 130000 Λ and 50000 Ξ events were used for these studies.

At these energies baryons are produced in a wider kinematical range (they extend further in rapidity y or Feynman-x x_F), than antibaryons. The decay kinematics of Λ and $\overline{\Lambda}$ (or Ξ^- and $\overline{\Xi}^+$) are similar. Therefore performance studies were done for Λ and Ξ particles only.

The cuts presented in table 4.1 were applied at the reconstruction stage: only candidates satisfying these conditions were further processed or written out to tape. Different analyses might favor different further selections: some might want very clean samples, being happy with low statistics; others might want as many candidates as possible, accepting a lot of background, or bad invariant-mass resolution. (For example during the later physical analyses discussed in this thesis additional selections were done in order to exclude events not originating from a proton-proton collision within the target, or to make the signal/background ratio better). The input to all physics analyses is the data produced by the finders. Since this chapter describes the method to reconstruct V^0s (and not a specific physics analysis), in the following performance studies all V^0 candidates output by MTV0 were used, without applying any further cuts.

Reconstruction efficiency

When valuing a new method for V^0 finding, one has to consider its benefits (what are the extra candidates found by this method) and its drawbacks (what are the candidates, which were reconstructed by the old method, but not reconstructed by the new one).

MTVO was never meant to be a replacement of VOFIND. The original plan was to use the candidates found by VOFIND, and let MTVO look for additional candidates. Results obtained by this approach are shown in figure 4.7 for Λs: in panel a.) the black line represents the input VENUS rapidity distribution (in order to show the reconstruction efficiency of the finders, and not the acceptance of the detectors or the efficiency of the tracking, only those lambdas were treated, which decayed into the charged channel, and had both daughters reconstructed). The empty symbols show the rapidity distribution of the lambdas reconstructed by VOFIND alone; the filled symbols represent the rapidity distribution of the lambdas reconstructed by VOFIND and MTVO combined. The right panel of the same plot shows the reconstruction efficiency (the reconstructed rapidity distributions divided by the input rapidity distribution – the black line in the left panel).

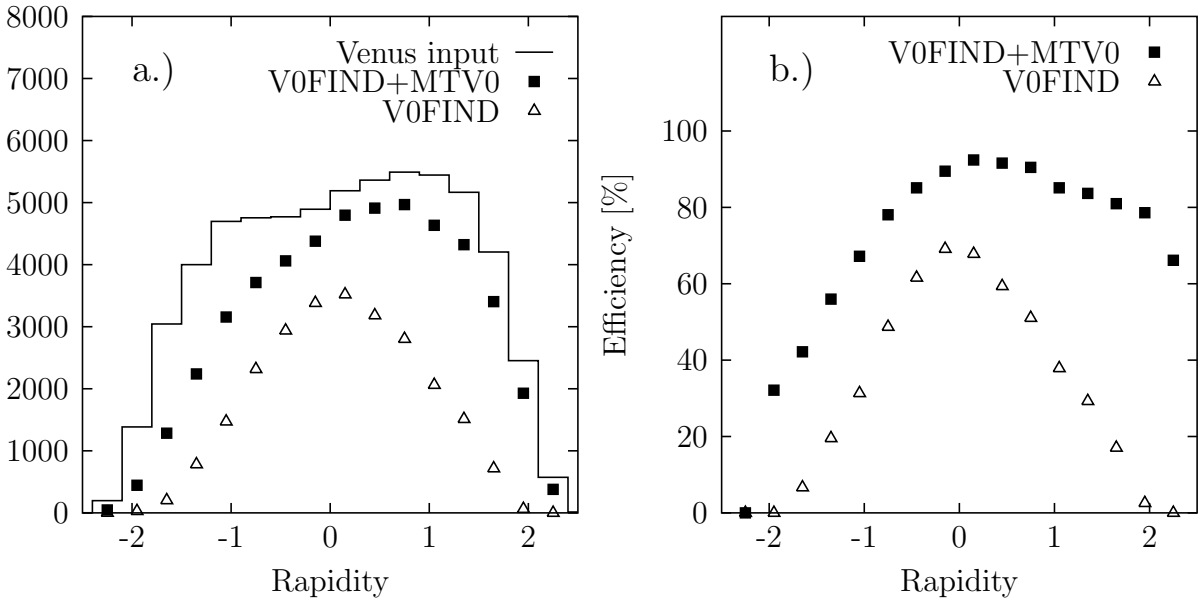

Figure 4.7: a.) Rapidity distributions of simulated Λs. See text for explanation. b.) Reconstruction efficiency as a function of rapidity, using only VOFIND or both (VOFIND and MTVO) finders.

The increased reconstruction efficiency for Λs in the whole rapidity range is clearly visible. At midrapidity the combined reconstruction efficiency approaches 100% (this is not a dramatic increase though). The increase is much more important in the backward and forward regions, where the efficiency is much lower. In these regions the efficiency has increased by more than a factor of 2.

As it was mentioned earlier, we expect this increase to have different reasons in different parts of the momentum space. In order to study these reasons, the momentum

space was divided into two hemispheres: the forward hemisphere ($0 < y_{\mathrm{cm}} < 1.75$) and backward hemisphere ($-1.75 < y_{\mathrm{cm}} < 0$). The lower and upper rapidity-limits were chosen to be the same as those applied later in the analysis. In the following paragraphs we will study the configuration of the extra candidates found by `MTVO`, without explicitly mentioning it every time.

In the backward hemisphere the reconstruction efficiency has increased by 67% (10968 candidates reconstructed by `VOFIND`, 7368 additional candidates reconstructed by `MTVO`). The additionally found lambdas can be classified as follows:

- The negative π daughter was (re-)fitted by `MTVO`: 83%
  - 88% of them: the π daughter was unusable for `VOFIND` (either had no momentum, or too few points):
    - 15% of them had no fitted momentum
    - 47% of them had less than 20 points in the two VTPCs
    - 38% had both reasons
  - 12% of them: though the π daughter was usable for `VOFIND`, it did not reconstruct the Λ.
- The positive proton daughter was (re-)fitted by `MTVO`: 17%
  - 76% of them: the proton had less than 20 points in the two VTPCs

These findings are in agreement with our expectations (see sec. 4.1.3). Finally we can conclude, that in the backward hemisphere the large increase in the reconstruction efficiency is indeed due to the additionally used tracks, which were not used by `VOFIND` (short tracks, or tracks with failing momentum).

In the forward hemisphere the reconstruction efficiency has increased by 92% (13794 lambdas reconstructed by `VOFIND`, 12744 additional lambdas reconstructed by `MTVO`). The additionally found candidates can be classified as follows:

- The positive proton daughter is re-fitted by `MTVO`: 75%[5]
  - 76% of them: the proton had no points in VTPC-1 or VTPC-2 (a real MTPC-only track)

[5]Selecting more and more forward regions this fraction approaches 100 %

  - 13% of them: the proton had a detected segment in the VTPCs, but less than 20 points in the two VTPCs (it was almost an MTPC-only track: it went through one of the inner corners of VTPC-2)

- The negative π daughter is re-fitted by `MTVO`: 25%

  - 30% of them: the π had less than 20 in in the two VTPCs.

These findings are again in agreement with our expectations (see sec. 4.1.3).

The reconstruction efficiency for Ξ^-s has also been studied using simulated particles. Figure 4.8 shows the increase of reconstruction efficiency for Ξs as a function of rapidity. Here again only those particles were treated, which had all 3 daughters reconstructed. The black line of the left panel shows the rapidity distribution of these particles, while the empty and filled symbols show the reconstructed rapidity distributions using only `V0FIND+XI_FIND`, or `V0FIND+XI_FIND`and `MTV0` combined, respectively. The right panel shows the reconstruction efficiencies (the reconstructed distributions divided by the input distribution). One can conclude, that the reconstruction efficiency has been more than doubled in the backward and forward regions.

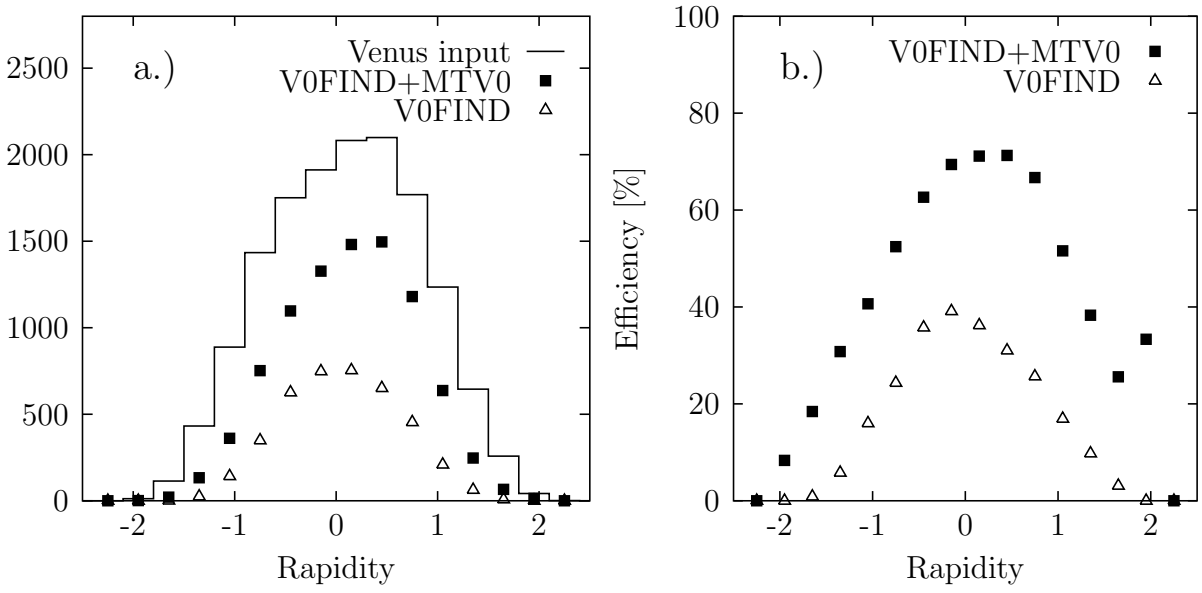

Figure 4.8: a.) Rapidity distributions of simulated Ξs. See text for details. b.) Reconstruction efficiency as a function of rapidity, using only `V0FIND+XI_FIND` or both (`V0FIND+XI_FIND` and `MTV0`) finders.

Invariant Mass Resolution

Reconstructing more V^0s or cascades does not necessarily mean a success: the reconstructed invariant mass distribution should not be much broader than before. Otherwise we loose our ability to fit and subtract the background from the invariant mass spectrum. Therefore performance studies of a new finder would not be complete without discussing the invariant mass resolution of the method.

The momentum space will be divided again into two hemispheres: forward ($0 < y_{cm} < 1.75$) and backward ($-1.75 < y_{cm} < 0$). For these studies `MTV0` was run independently from `V0FIND`. Figure 4.9 shows the invariant mass distributions obtained by `MTV0` and `V0FIND`. Left and right panels show the backward and forward hemisphere, respectively.

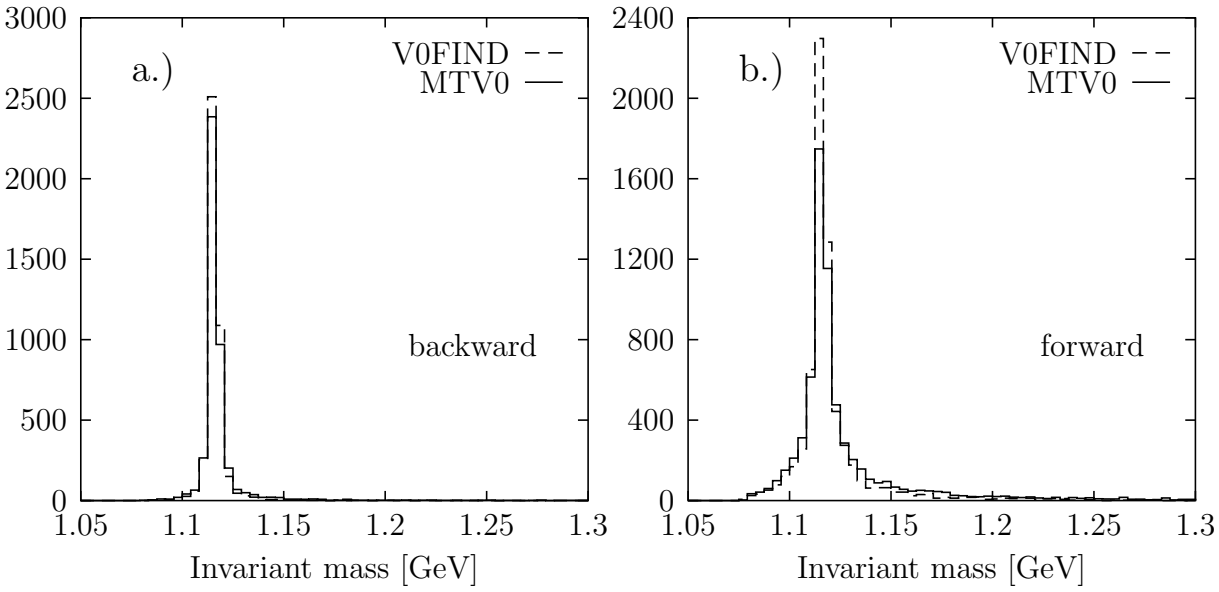

Figure 4.9: Invariant mass distributions obtained by `MTV0` and `V0FIND`. The histograms have been normalized to the same area.

The invariant mass distribution of `MTV0` is only slightly broader than that of `V0FIND`. This broadening does not influence the usability of `MTV0`. The mass peak of both finders is much broader in the forward hemisphere. This can be explained with the following arguments: the daughters of fast Λs will have a small opening angle. In this case the uncertainty of the reconstructed vertex position is bigger than in those cases, when the daughters have a large opening angle. Since tracks in the magnetic field are curved, they will have different directions at shifted z-positions of the reconstructed vertex; their opening angle will be therefore also different, which leads to a smeared invariant mass.

This is illustrated with simulated particles in figure 4.10: in the left panel the vertex position resolution is shown as a function of the rapidity of the Λ. The z position of the reconstructed vertex is indeed more and more smeared for faster lambdas. In the right panel the relation between the smearing of the reconstructed mass and the smearing of the reconstructed vertex position is shown. This plot clearly indicates a worse mass resolution for V^0s with misplaced vertex position.

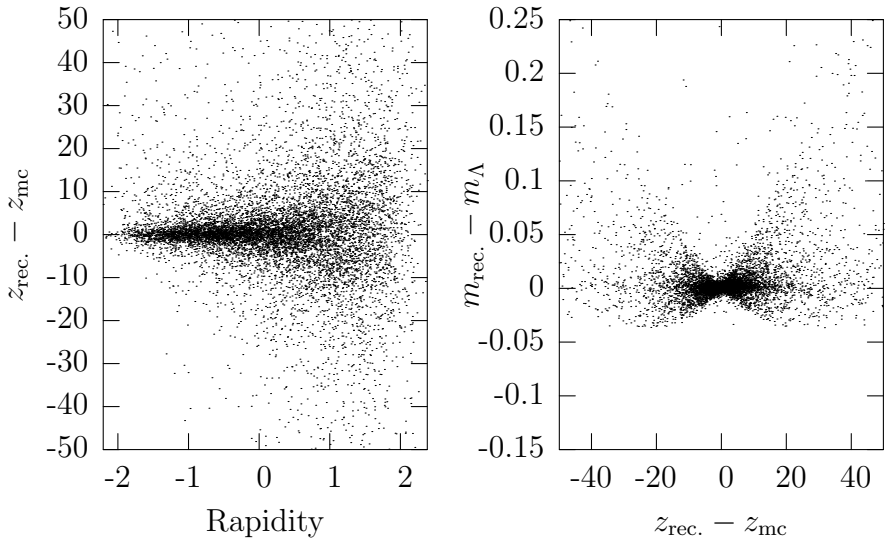

Figure 4.10: Explanation of the broadening of the invariant mass peak in the forward hemisphere. Left panel: the deviation of the reconstructed vertex z coordinate from the true value of the simulation, as a function of rapidity. Right panel: deviation of the reconstructed invariant mass from the nominal value ($m_\Lambda = 1.115$ GeV), as a function of the misplacement of the vertex.

If we want to avoid the broadening of the mass peak in the forward hemisphere, we have to select such V^0s, which decayed in a region with low magnetic field (where the tracks are straight, and a shift in the vertex position doesn't cause such a big difference in the opening angle). Figure 4.11 shows the y-component of the magnetic field along the beam axis, as a function of z. In the region $z < -530$ the strength of the magnetic field is low. If we select forward V^0s decaying in this region, the mass peak is indeed much narrower (fig. 4.12).[6]

[6]This is an unfortunate choice: fast Λs have a longer decay time, and decay farther from the primary vertex. This cut selects Λs decaying close to the primary vertex.

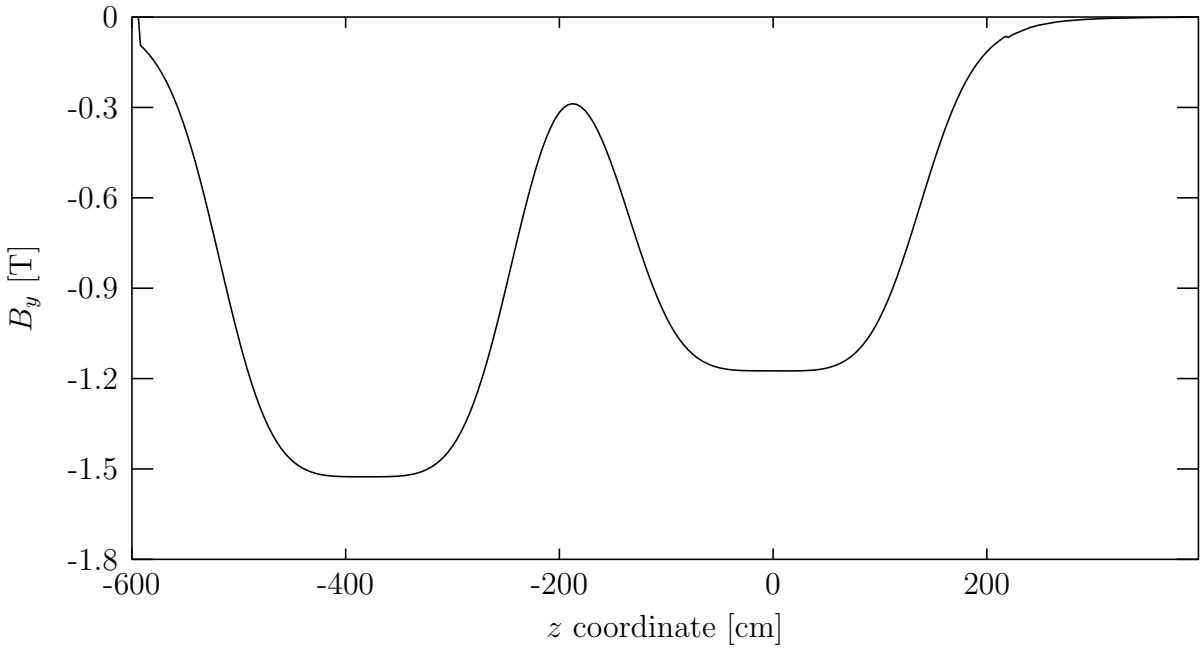

Figure 4.11: The y-component of the magnetic field along the beam axis, as a function of z.

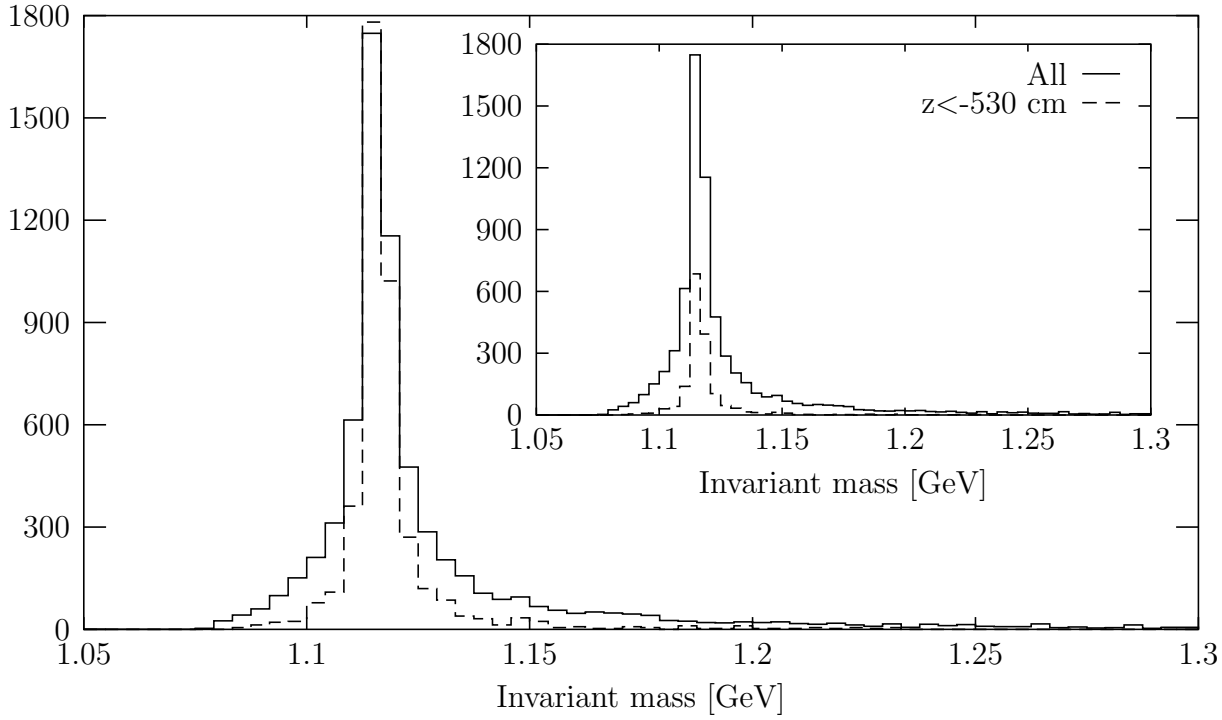

Figure 4.12: Invariant mass peak obtained by `MTVO` of forward ($y > 0$) Λs (simulation): accepting all lambdas (solid), and Λs decaying at $z < -530$ (dashed line). The two histograms have been normalized to the same maximum. The small panel shows the two histograms without normalization, in order to illustrate the effect of the cut.

Chapter 5

Analysis

In the previous chapters the new method for V^0 finding has been described, and its performance was studied. Simulated Λs and Ξs were used for these studies. Since in that case reconstructed tracks were matched with the Monte Carlo tracks, it was possible to study only those V^0 candidates, which corresponded to simulated Λs or Ξs: there were no background V^0s. Similarly, there were no *background* (or *empty target*) events[1] in this sample, which should be excluded from the analysis. Therefore in those studies no additional cuts were applied, only the ones present on the reconstruction level.

During the data analysis much care has to be taken to filter out empty-target events, and additional selections have to be done in order to keep only such candidates, which are adequate for these studies. The cuts applied for event- and candidate-selection will be described in this chapter, together with the discussion about cross-section determination, taking into account these cuts. The results of `MTVO` (rapidity, Feynman-x and p_T spectra) will be presented in the next chapter, together with `VOFIND` results. The stability of these results against the applied cuts will be also discussed there.

5.1 Selection of Candidates

Different analyses may need different selections of the candidates, therefore there is no general recipe, what kind of cuts one has to apply. The main results presented in this thesis are the inclusive spectra of strange and multi-strange baryons. During the analysis for these results the following cuts were used:

[1] Empty target events are those events, which fulfilled the trigger requirements, but do not originate from an interaction within the target, but from collisions of the beam particle with other materials, for example the mylar foils of the target tube (consisting mostly of carbon).

The background could be substantially suppressed with a cut on the dE/dx (specific ionization) of the daughters of the candidates (with this cut one selects the right particle species). For each individual track the dE/dx information (and its error) was provided by collaborators [21]. A 3σ cut was chosen around the Bethe-Bloch curves (a candidate was accepted only if the dE/dx value of all of its daughters fell closer to the Bethe-Bloch value (3.3) than 3 times the error of the dE/dx value). Only a negligible fraction of particles falls outside of this region; no correction for this cut was applied.

Only candidates reconstructed more than 12 cm away (`mvdz` cut) from the main vertex were accepted.

The *decay-plane* of a Λ ($\overline{\Lambda}$) is defined as the plane spanned by the two momentum-vectors of its daughters. The direction of the decay-plane also proved to be a useful quantity in increasing the signal/background ratio. Let us introduce a new coordinate system with axes x', y' and z' (see figure 5.1). z' is defined by the momentum-vector of the Λ. The y' axis lies in the plane spanned by the z' and y axes, and it is perpendicular to z'. The x' axis is defined to be perpendicular to both z' and y'. The angle ϕ is defined as the angle between the y' axis and n (the normalvector of the decay-plane).

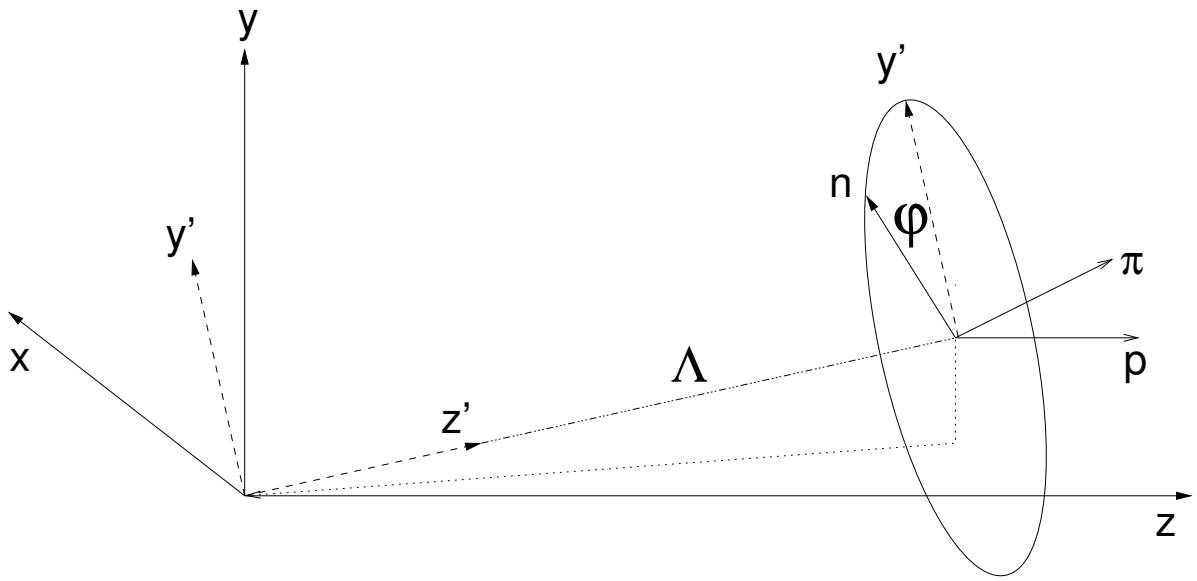

Figure 5.1: The definition of the ϕ angle

In those configurations, where ϕ is close to zero or $\pm\pi$ (the normalvector of the decay plane is close to the y' axis), the projections of the trajectories of the proton and pion daughters onto the $y-z$ plane (side-view) are also very close, their opening angle is small. Since in the NA49 magnetic field the particle trajectories in the $y-z$ plane are

approximately straight and independent from the momentum of the particle, variations in the momentum of the two daughters will essentially not change the $y-z$ projections of their trajectories; these variations will only modify the $x-z$ projections. That is, variations of the momenta will change the trajectories *within* the decay-plane. In this case a crossing point can be found even if the momenta are misaligned by a relatively large amount, leading to a smeared mass peak. On the contrary, if ϕ is close to $\pi/2$ (the two daughters have a large opening angle in the $y-z$ plane), the crosspoint is basically defined by the $y-z$ projections of the trajectories – which are unaffected by misaligned momenta. Variations of the momenta will now move the trajectories *out from* the decay plane, and incorrect momentum-determination will cause, that the two tracks miss each other, and the V^0 will not be reconstructed. As a rule of thumb we can conclude, that configurations having a ϕ angle close to zero or $\pm\pi$ will have a much more smeared invariant mass distribution. Similarly, the background is also significantly higher in these cases. This is demonstrated in figure 5.2. In order to increase the quality of the invariant mass spectra, a cut on th ϕ angle was introduced: only candidates having $25^\circ < |\phi| < 155^\circ$ were used in the analysis. These ranges are indicated with dashed line in figure 5.2a. Beyond the increasing number of Λ candidates at $\phi = 0, \pm 180^\circ$ in figure 5.2a, one can also observe a dip at $\phi = 0^\circ$. This has the following reason: as it was described in section 4.2, `MTVO` looks for the initial value of the z coordinate of the V^0 vertex by looking for a crosspoint of the $y-z$ projections of the two tracks. This method might fail, if the two projections are parallel – that is, if $\phi = 0$.

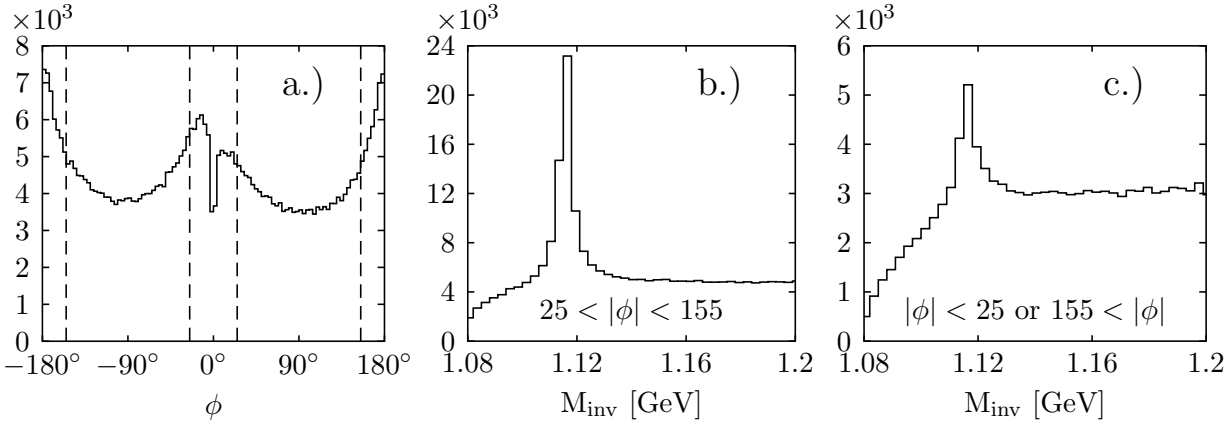

Figure 5.2: The behavior of the invariant mass spectrum as a function of ϕ: a.) – number of Λ candidates as a function of ϕ. b.) and c.) – Λ invariant mass spectra at different ϕ regions.

For `V0FIND` results only tracks having more than 20 points in either VTPC-1 or VTPC-2 were used. This cut was applied on the reconstruction level, and the effect of this cut could later not be checked. In order to study the effect of a cut on the number of points, no cut was applied for `MTV0` on the reconstruction level. During the data analysis several different number-of-points cuts were applied, and its effect was studied. This will be presented in section 6.

For Ξ-finding a cut was applied on the Λ ($\overline{\Lambda}$) mass. Only those candidates were accepted, where the invariant mass of the Λ daughter fell into the mass window $m_\Lambda \pm$`dm_v0`, where `dm_v0` was set to 10 MeV (m_Λ=1.115 GeV, the nominal mass of the Λ). The background below the mass peak could be substantially decreased by requiring that the two daughters of the V^0 have more than 20 points in at least one VTPC, and that the π daughter of the Ξ^- ($\overline{\Xi}^+$) has at least 20 points in the two VTPCs together. Additionally, it was required that the reconstructed vertex of the Ξ^- or $\overline{\Xi}^+$ be at least `mvdz`=12 cm from the main vertex. A 3σ cut around the Bethe-Bloch curves of the daughters was used to select the appropriate particle species.

The different cuts applied in the analysis of `MTV0` results are summarized in table 5.1. The mass spectra of the Λ, $\overline{\Lambda}$, Ξ^- and $\overline{\Xi}^+$ after these cuts are shown in figure 5.3.

Cut	Description	Λ and $\overline{\Lambda}$	Ξ^- and $\overline{\Xi}^+$
dE/dx	Specific ionization, applied for all daughters	3σ	3σ
`mvdz`	Minimum distance of the reconstructed vertex from the primary vertex	12 cm	12 cm
`phi`	The orientation of the decay plane	$25° < \phi < 155°$	—
`dm_v0`	Deviation of the invariant mass of the reconstructed Λ from the nominal mass of the Λ	—	10 MeV
`npoint`	Number of points of the daughters	several	>20 in at least one VTPC for V^0 daughters >20 in the two VTPCs together for the pion

Table 5.1: Cuts applied in the data analysis

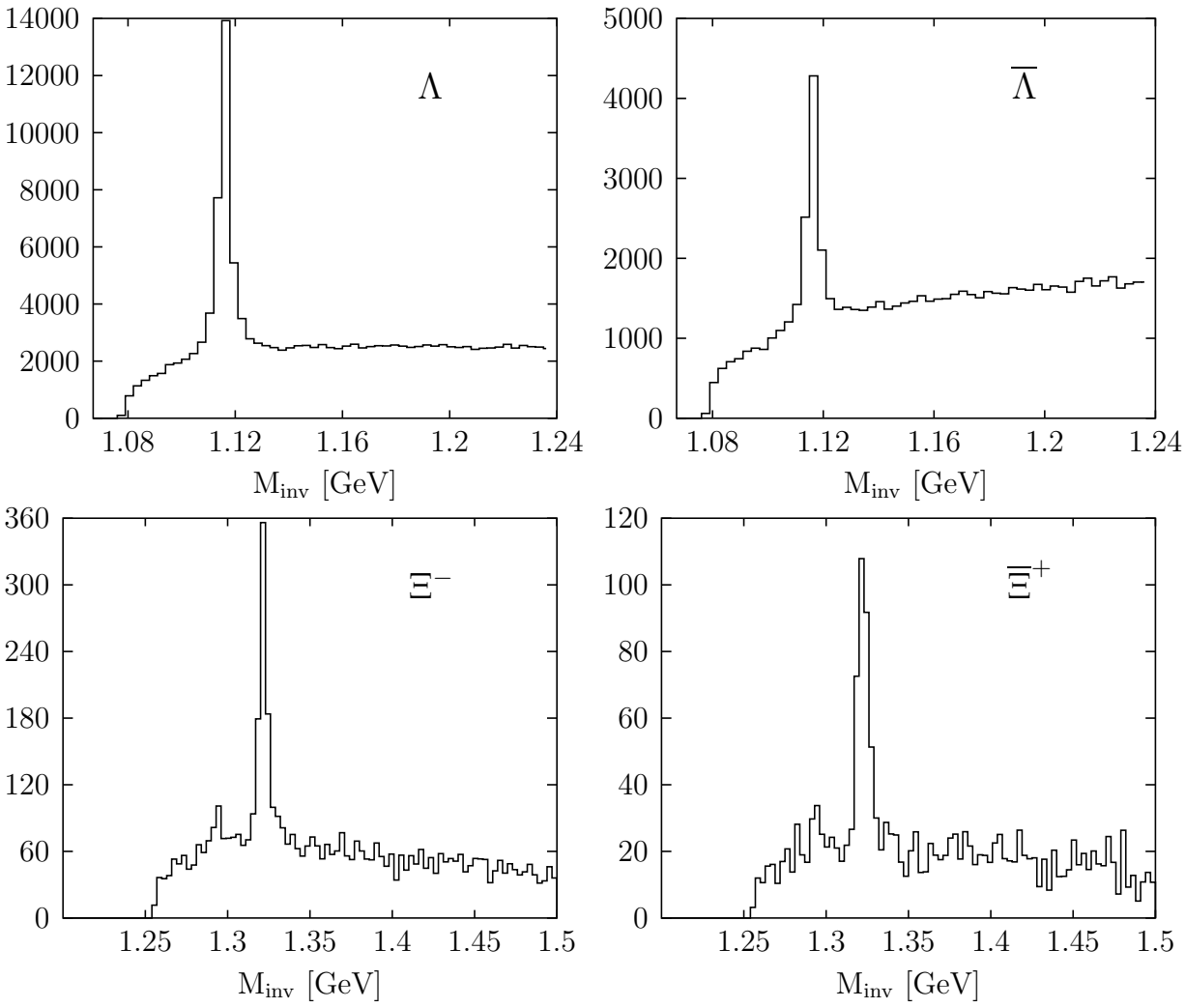

Figure 5.3: The mass distributions of Λ, $\overline{\Lambda}$ (Ξ^-, $\overline{\Xi}^+$) in the rapidity-range -1.75< y <1.75 (-1.25< y <1.25)

5.2 Event Selection and Cross Section Determination

5.2.1 Trigger Cross Section

Only those events are accepted and recorded, which fulfill the trigger conditions (see sec. 2.2.2). Most elastic events, and a small fraction of inelastic events are rejected by the trigger of the experiment. The trigger cross-section σ_{tr} is the total cross-section of all interactions accepted by the trigger system:

$$\sigma_{tr} = \frac{1}{\rho l N_A / A} \frac{N_{\text{ints}}}{N_{\text{beams}}^{\text{gated}}} \tag{5.1}$$

where $\rho = 7.08 \times 10^{-2}$ g/cm^3 is the density of the target, $l = 20$ cm is its length, $N_A = 6.022 \times 10^{23}$ mol^{-1} is the Avogadro number, and $A = 1$ g/mol is the atomic weight of the target material, N_{ints} is the number of interactions accepted by the trigger, and $N_{\text{beams}}^{\text{gated}}$ is the number of gated beam particles[2] traversing through the target (registered by the S1 counter, see sec. 2.2.1).

Unfortunately there are also empty-target events accepted by the trigger. In order to account for their presence in the recorded data sample, *empty-target runs* were also recorded during the runtime: the target tube was emptied, and events were recorded with the same trigger conditions. These collisions would also contribute to the trigger cross-section calculated in the above-mentioned naive way. Their contribution therefore has to be subtracted from the above naive formula:

$$\sigma_{tr} = \frac{1}{\rho l N_A / A} \left[\left(\frac{b_i}{b_g} \right)^{FT} - \left(\frac{b_i}{b_g} \right)^{ET} \right] \tag{5.2}$$

where b_i and b_g mean "interacted beam" and "gated beam" (they are a shorthand for the above N_{ints} and $N_{\text{beams}}^{\text{gated}}$, respectively). FT and ET refer to empty-target and full-target, respectively. The trigger cross sections for the '99 and 2000 p-p data were 28.57 and 28.49 mb.

5.2.2 Event Selection

Empty-target events can also contain strange baryons. Since these collisions are proton-nucleus collisions, the production probability of these particles might be different from that in proton-proton collisions. Therefore these events have to be excluded from the analyzed sample.

True proton-proton collisions happen somewhere within the volume of the hydrogen target. The position of the primary vertex can be reconstructed from the detected particles (see section 3.1.4). A cut on this position can be used to exclude empty-target events. The reconstructed position of the primary vertex will of course be smeared. The more tracks one uses for the vertex determination, the more accurate its position will be. The smearing of the reconstructed vertex position will therefore be dependent on the multiplicity of the event (should it be an empty-target event or a true proton-proton

[2]Those beam particles, which arrived during the "open" period of the detector system (outside of the *dead-time*, when the detector or the DAQ was busy). Beam particles arriving during the dead-time could in no way produce an interaction accepted by the trigger, so they are not counted.

interaction). This is demonstrated in fig. 5.4 for empty-target events (these are more illustrative, since in this case the vast majority of interactions happen at well-defined places – for example at the mylar windows of the hydrogen target).

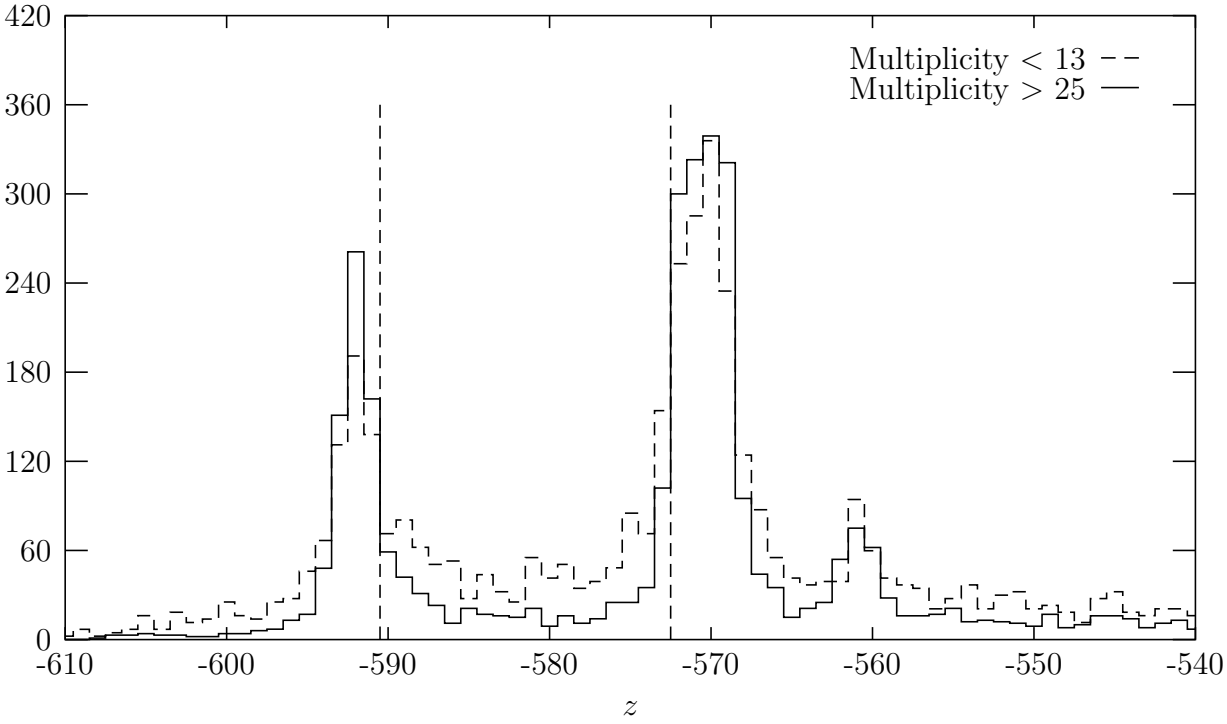

Figure 5.4: Distribution of the z coordinate of reconstructed primary vertices in empty-target runs, for two classes of multiplicity. The two peaks correspond to the mylar windows of the target tube, where many of the empty-target events occur. (Other peaks, corresponding to other materials in the beamline are excluded from the z-range of the plot)

In figure 5.4 only a limited z-range (around the target) is shown; many empty-target events happened in the z-range not shown here. Only a small fraction (7%) of empty-target events have a reconstructed main vertex within the z-range -590.5 cm$<$ z $<$-572.5 cm (which is indicated in the figure with dotted lines). In order to exclude empty target events, only those events were accepted, which had their primary vertex reconstructed within this fiducial volume, which corresponds to a $\pm$9 cm cut around the center of the target (which is 20 cm long). The ratio of the trigger cross sections in empty-target and full-target events is 18%, therefore the contamination by the empty-target events in our event sample is estimated to be 1.3%. Additional cuts on the primary vertex were applied in order to exclude garbage events: it was required that the main vertex fit succeeded and the resulting x and y coordinates of the primary vertex satisfy $\sqrt{x^2_{\text{primary}} + y^2_{\text{primary}}}$ $<$1 cm.

5.2.3 The Event Weighting Technique

Inclusive cross-sections in a momentum bin $\Delta p^3_{\rm bin}$ are determined from the following formula:

$$E \times \frac{d\sigma_{inc}}{dp^3} = E \times \frac{\sigma_{tr}}{\Delta p^3} \frac{N_{\rm part}}{N_{\rm events}} \tag{5.3}$$

where σ_{tr} is the trigger cross-section, $N_{\rm events}$ is the number of events in the analyzed data sample, $N_{\rm part}$ is the number of particles produced in the momentum-bin Δp^3. The way $N_{\rm part}$ and $N_{\rm events}$ were calculated will be described in this section below.

As it was described above, the rejection rate of events by the fiducial cut on the main vertex position is multiplicity dependent. If V^0 or cascade production is correlated with multiplicity, average events or events containing a V^0 or cascade might be rejected with a different rate. Therefore an event weighting technique was applied (which was suggested by [81]).

The fiducial cut on the primary vertex position rejects of course also true proton-proton events occurring within the target volume. In the ideal case (if the vertex position determination would be 100% accurate), this would reject 10% of all proton-proton events (the fiducial volume is 18 cm of the 20 cm-long target) – independently from the multiplicity of the event. But since the vertex position resolution is not that good, and depends on multiplicity, therefore low-multiplicity events will have a larger smearing, and a larger fraction of events will be outside of this accepted volume. Therefore multiplicity-dependent corrections have to be applied, to correct for the number of rejected proton-proton events. These corrections have been worked out by collaborators [78], and provide the information, how big fraction of the events of a certain class of multiplicity is rejected by this cut. These correction factors have been defined as

$$w_m = \frac{N_m^{\rm all}}{N_m^{\rm acc}} \tag{5.4}$$

where the index m refers to the multiplicity, $N_m^{\rm all}$ is the number of all triggered events (of multiplicity m), and $N_m^{\rm acc}$ is the number of events within the selected fiducial volume. These corrections are applied as event weights: when counting the number of events in the analyzed data sample, each event is weighted with the corresponding w_m factor:

$$N_{\rm events} = \sum_i w_{m_i} \tag{5.5}$$

where the sum runs over all events accepted by the fiducial cut (i indexes these events); m_i is the multiplicity of the ith event. This formula gives back the true number of proton-proton events.

In order to decrease the data volume processed during this analysis, a micro-DST was extracted from the big DSTs[3], which contained much less information (but still enough for this analysis). *Zero prong events* (events with no recorded tracks, no primary vertex) were not written to the micro-DST. These events do not contain Λ or Ξ particles, but they count into the trigger cross-section, therefore we have to account for them when counting N_{events} as well. This was obtained by a simple factor Z, which was derived by collaborators [78], analyzing the big DST:

$$N_{\text{events}} = Z \times \sum_i w_{m_i} \tag{5.6}$$

The nominator (number of produced particles, N_{part}) of eq. (5.3) also needs corrections: due to the limited acceptance of the detectors, the less-than-100% efficiency of the reconstruction software and the cuts applied to select adequate V^0 or cascade candidates, not all particles produced in a phase-pace bin are observed. These corrections were derived using a full simulation of the detectors, and applying the reconstruction chain to the simulated data, as it was described in sec. 3.3. The correction factors in a phase-space bin are defined as

$$C = \frac{N_{\text{MC}}}{N_{\text{rec}}} \tag{5.7}$$

where N_{MC} is the number of simulated particles emitted in the phase-space bin, and N_{rec} is the number of reconstructed particles (only particles decaying into the charged channel were treated). If the phase-space bins are reasonably small, the corrected results will be independent from the generated distribution of the simulated particles. The number of emitted particles in a phase-space bin is therefore

$$N_{\text{part}} = C \times N_{\text{obs}} \times \frac{1}{B} \tag{5.8}$$

[3]DST is a shorthand for Data Storage Tape, which is used in the jargon for all kinds of files storing the recorded or reconstructed data

where $N_{\rm obs}$ is the number of observed particles in that bin, the derivation of which will be described below, and B is the branching ratio of the examined particle into the charged final state.

The fiducial cut rejects also such events, which contain a V^0 or cascade candidate. If the total number of events was corrected for this effect, this has to be taken into account also at the counting of the number of observed particles. Assuming, that the smearing of the main vertex (and therefore the rejection rate of the fiducial cut) depends only on the multiplicity of the event, but not on the presence or absence of a Λ ($\overline{\Lambda}$, Ξ^-, Ξ^+)[4], we can apply the same w_m weights to the candidates: when collecting the invariant mass spectrum in a phase-space bin, every candidate is weighted by w_m, where m is the multiplicity of that event. The number of observed particles, $N_{\rm obs}$ is defined as the surface of the mass peak above the background in this weighted histogram.

As an alternative to presenting the cross section, one can also present the particle yields as the number of particles per inelastic event. In this case the cross section defined in eq. (5.3) has to be divided by the total inelastic cross section of p-p collisions, which is $\sigma_{\rm inel.}$=31.7 mbarn at $\sqrt{s}$=17.2 GeV.

5.3 Determination of the Number of Candidates

Weekly decaying particles, such as the Λ and Ξ^- have a very narrow mass peak. Its width is determined by the resolution of the equipment and the reconstruction software. In this case one usually selects two invariant mass regions around the peak, and fits the mass spectrum in these ranges with some function (usually a polynomial). This function defines the background below the mass peak. The number of observed particles can be calculated as the surface of the peak above this curve.

As it was demonstrated with simulation in figure 4.12, the invariant mass peak of the reconstructed lambdas becomes broader with increasing rapidity. The long tail reaches out to high values of the invariant mass. In the forward hemisphere this makes it not possible to use the above described method without additional selection criteria. As it

[4]This does not necessarily have to be true: at the time of the reconstruction of the primary vertex, we don't know a priori, which tracks are daughters of a V^0 or a cascade. These tracks are also used for the primary vertex reconstruction, and since they do not come from this vertex, they can pull the fitted position of the primary vertex. A Monte Carlo study has been done in order to check this effect, see section 6.5

was described in section 4.2.4, requiring the V^0 vertex to be in a region with relatively low magnetic field (for example at $z < -530$ cm) can help to make the mass peak narrower. This was the first approach to derive the number of observed candidates during the present analysis. However, this cut strongly decreased the number of accepted particles: fast Λs and $\overline{\Lambda}$s have a longer decay length in the laboratory frame, and this cut selected those, which decayed close to the primary vertex. Recently a new method was developed and used to extract the number of observed particles. Though this was done by [90] and not by the author, this method will be shortly described here, since it was used to derive the final results of the experiment. The basic idea is that the invariant mass spectrum of the reconstructed simulated particles can be used to estimate the broadening of the mass peak. As figure 4.6 demonstrates, there are still differences between the simulation and the data, concerning the quality of the reconstruction, but this will cause only a minor error in the results. In this method the observed invariant mass spectrum is fitted with a sum of a polynomial and the invariant mass spectrum resulting from the simulation, scaled by a number, which is also a parameter of the fit. The surface of the scaled Monte Carlo spectrum gives the number of observed particles.

Chapter 6

Results

This chapter presents the results obtained by the different finders, and the applied corrections. The stability of the results will be discussed, and the way from the results of the individual finders to the final, corrected spectra will be shown. A separate chapter is devoted to the presentation of the final results, without the technical details.

6.1 Λ and $\overline{\Lambda}$ Results

The available statistics of Λ and $\overline{\Lambda}$ candidates after the cuts shown in table 5.1 and the highest `npoint` cut (number of points of the daughters had to be larger than 20 in either VTPC-1 or VTPC-2) was 25000 and 6300, respectively. This statistics allowed to divide the phase-space into rapidity—p_T or Feynman-x—p_T bins. Correction factors were determined in each bin from the simulation. For the calculation of the correction factors for Λ ($\overline{\Lambda}$) 250000 (100000) `VENUS` [76]-generated Monte Carlo events were used.

6.1.1 Rapidity $-$ p_T binning

For Λs the rapidity range [-1.75;1.75] was divided into 7 bins. For $\overline{\Lambda}$s a smaller rapidity range was used: the range [-1.25; 1.25] was divided into 5 bins. The p_T range extended from 0 to 1.4 GeV. For Λs in the central region (-0.75$< y <$0.75) 0.1 GeV wide p_T bins were used. For the remaining bins, and for $\overline{\Lambda}$s the size of the p_T bins was 0.2 GeV. Depending on rapidity, the statistics was not always enough to derive results in the whole p_T range shown above. This will be visible on the plots.

As it was mentioned earlier, several `npoint` cuts were applied during the analysis of `MTVO` results (`npoint`=0, 10 and 20. Note, that in the case `npoint`=0 the MTPC-only

tracks are also included in the analysis). Figures 6.1 and 6.2 show the p_T distributions of Λ and $\overline{\Lambda}$ at different rapidities, with several `npoint` cuts. `VOFIND` results are also shown for comparison. `MTVO` results are stable against the varied `npoint` cuts, and agree within errors with the results obtained by `VOFIND`. The symbols in these figures are often very close, and can not be distinguished – the main message of these figures is the stability of the results against the `npoint` cut.

The yield in a rapidity bin was calculated by summing up the yields in the p_T bins. The yields in such p_T regions, where no results could be obtained, were estimated by fitting the transverse momentum distribution with the function

$$\frac{dN}{dp_T} = A \cdot p_T \cdot e^{\frac{-m_T}{T}} \tag{6.1}$$

and integrating this function over the unmeasured p_T regions. In this formula A and T were the parameters of the fit, and m_T is the *transverse mass* of the particle: $m_T = \sqrt{m^2 + p_T^2}$. (Statistical models predict the shape of the m_T spectra to be of the form (6.1), which well describes the observed m_T spectra in p-p collisions as well) The rapidity distributions of Λ and $\overline{\Lambda}$ are shown in figure 6.3. The rapidity spectrum of Λ has a minimum at $y_{cm} = 0$. See page 89 for a discussion about the shape of baryon rapidity distributions.

Observed Λs and $\overline{\Lambda}$s include not only those, which are primarily created in the collision: decay products of Ξ^-s (and Ξ^0s) and $\overline{\Xi}^+$s (and $\overline{\Xi}^0$) or other higher-mass states (for example $\Sigma^0 \to \Lambda\gamma$ with a branching ratio of 100%, $\Sigma^{\pm}(1385) \to \Lambda\pi^{\pm}$ with a branching ratio of 88%) also contribute to the observed sample. Since feeddown corrections need the knowledge of the phase-space distribution of Ξs, this topic will be postponed to a later section, after the presentation of the Ξ results.

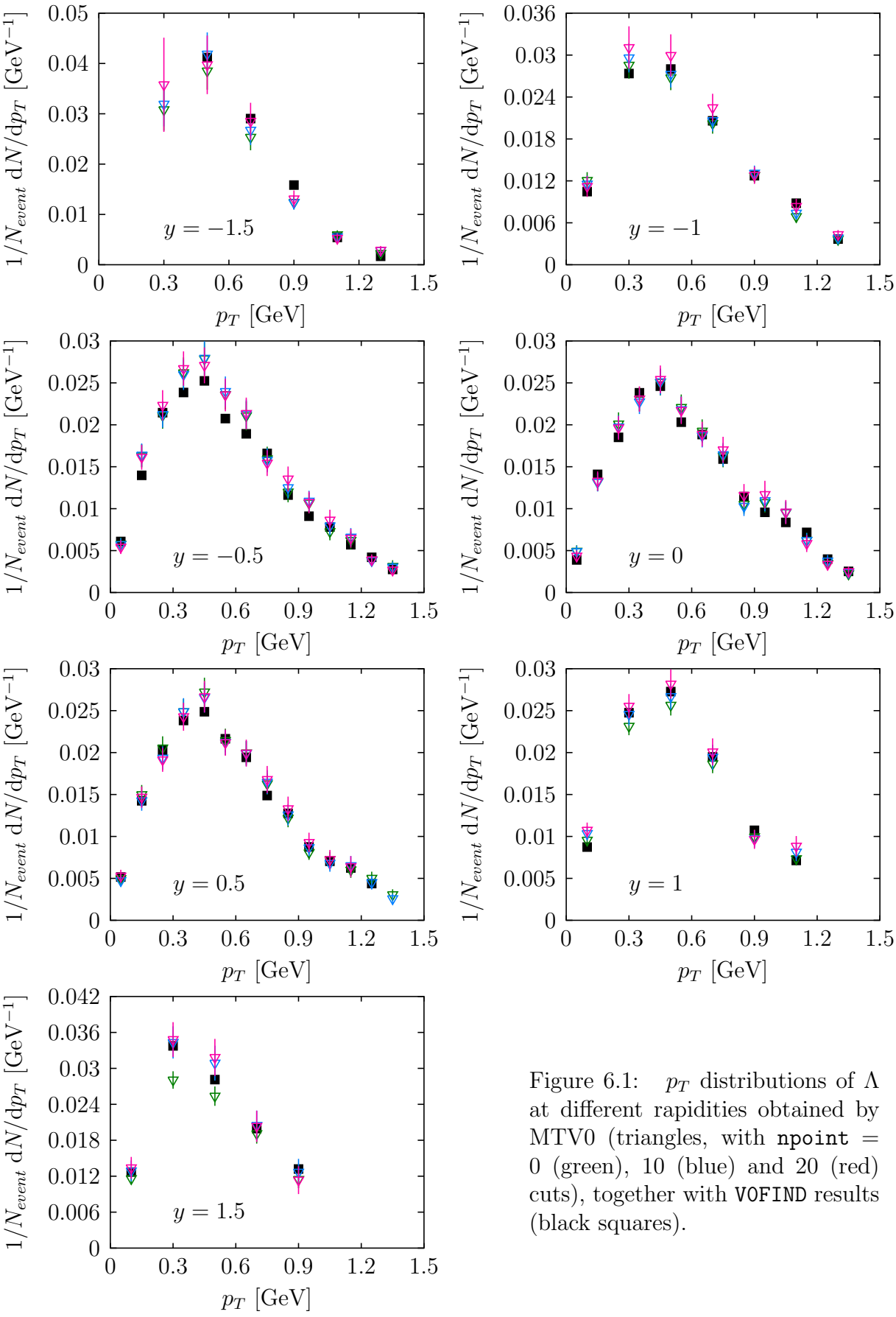

Figure 6.1: p_T distributions of Λ at different rapidities obtained by MTV0 (triangles, with `npoint` = 0 (green), 10 (blue) and 20 (red) cuts), together with `VOFIND` results (black squares).

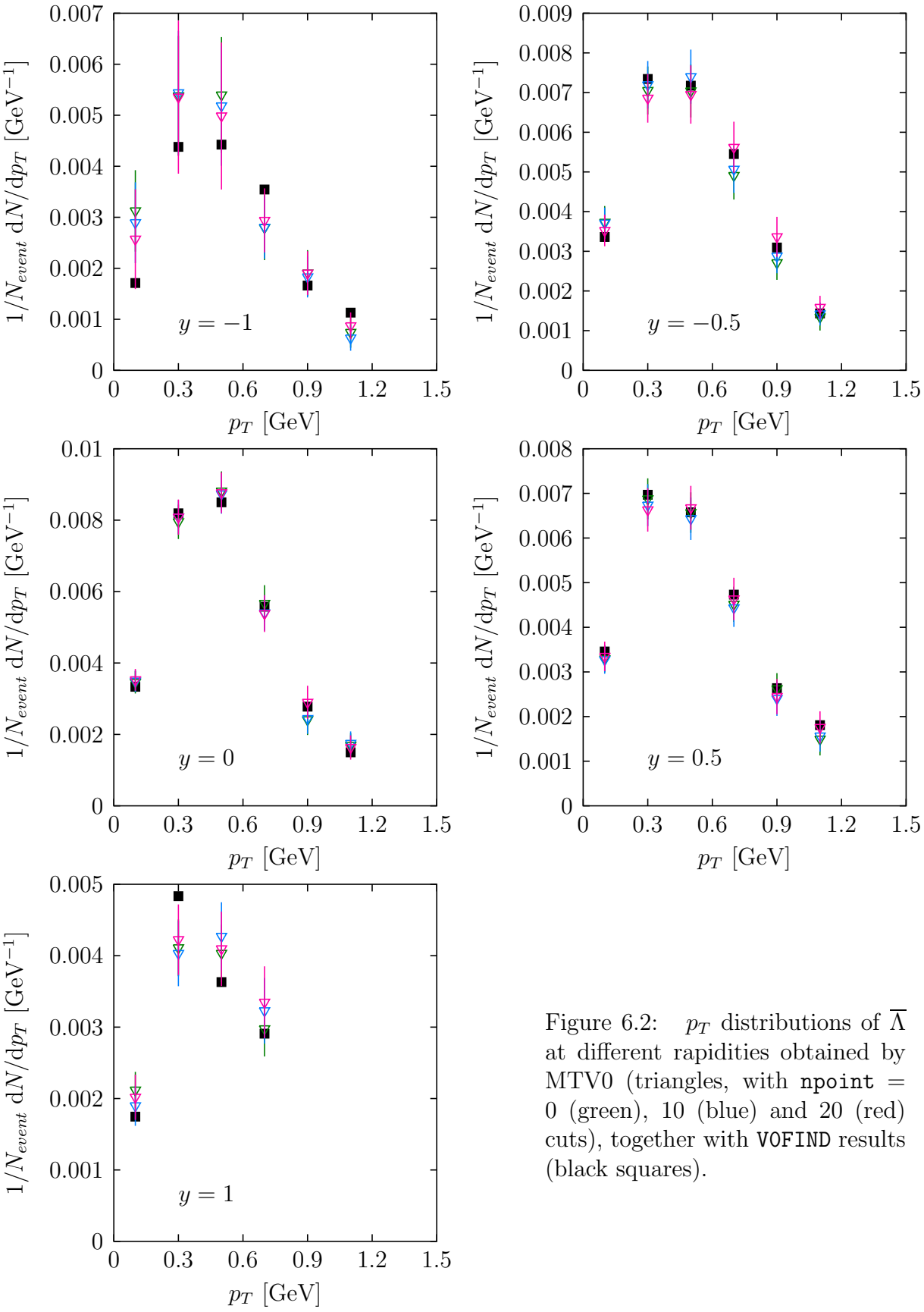

Figure 6.2: p_T distributions of $\overline{\Lambda}$ at different rapidities obtained by MTV0 (triangles, with `npoint` = 0 (green), 10 (blue) and 20 (red) cuts), together with `VOFIND` results (black squares).

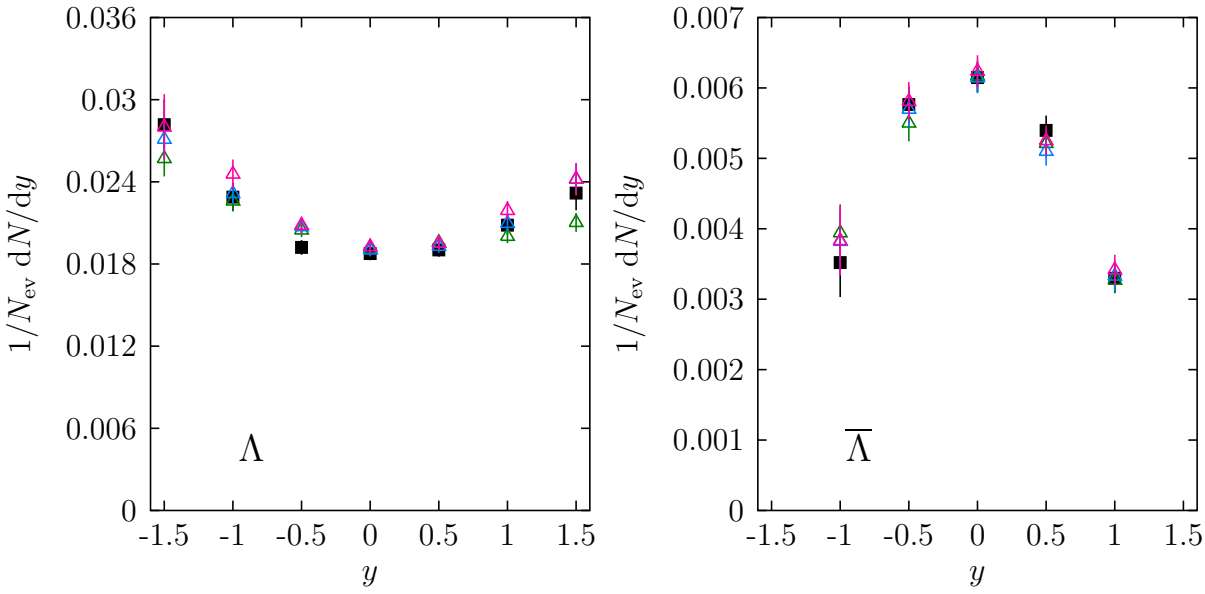

Figure 6.3: Λ and $\overline{\Lambda}$ rapidity distributions obtained by `MTVO` (with `npoint` = 0 (green), 10 (blue) and 20 (red) cuts), together with `VOFIND` results (black)

6.1.2 Feynman-x – p_T binning

For Λs the Feynman-x range [-0.35; 0.35] was divided into 7 bins. For $\overline{\Lambda}$s a smaller range was used: [-0.25; 0.25], divided into 5 bins. The studied p_T range was [0;1.4] GeV. For Λs in the central bins (x_F=-0.1, 0 and 0.1) small p_T bins were used (0.1 GeV wide), while for the remaining bins, and for $\overline{\Lambda}$s the size of the p_T bins was chosen to be 0.2 GeV, due to the smaller statistics available here. Figures 6.4 and 6.5 show the p_T distributions of Λ and $\overline{\Lambda}$ at different Feynman-x values, together with `VOFIND` results.

The Feynman-x distributions were obtained in the same way as described for rapidity–p_T binning. The Feynman-x distributions of Λ and $\overline{\Lambda}$ are shown in figures 6.6 and 6.6. The invariant Feynman-x distribution (see appendix B) is defined as

$$F(x_F) = \frac{1}{\pi} \int \frac{E}{p^{\mathrm{cm}}_{\mathrm{beam}}} \cdot \frac{\mathrm{d}N}{\mathrm{d}x\ \mathrm{d}p_T}\ \mathrm{d}p_T \tag{6.2}$$

where the energy E is expressed as a function of x_F and p_T:

$$E = \sqrt{m^2 + (x_F \cdot p^{\mathrm{cm}}_{\mathrm{beam}})^2 + p_T^2} \tag{6.3}$$

(for more details see appendix B). In a Feynman-x bin $F(x_F)$ was calculated as the sum $\sum_i E_i/p^{\mathrm{cm}}_{\mathrm{beam}} \cdot N_i/\mathrm{d}x_F$, where the index i runs over the measured p_T bins, and E_i is the energy of lambdas calculated at the center of the x_F–p_T bin, plus the integral of the fitted curve (6.1) multiplied by $E/p^{\mathrm{cm}}_{\mathrm{beam}}$, over the unmeasured p_T bins. These distributions are shown in figure 6.7. `VOFIND` and `MTVO` results are again in nice agreement, and `MTVO` results are stable against the varied `npoint` cut.

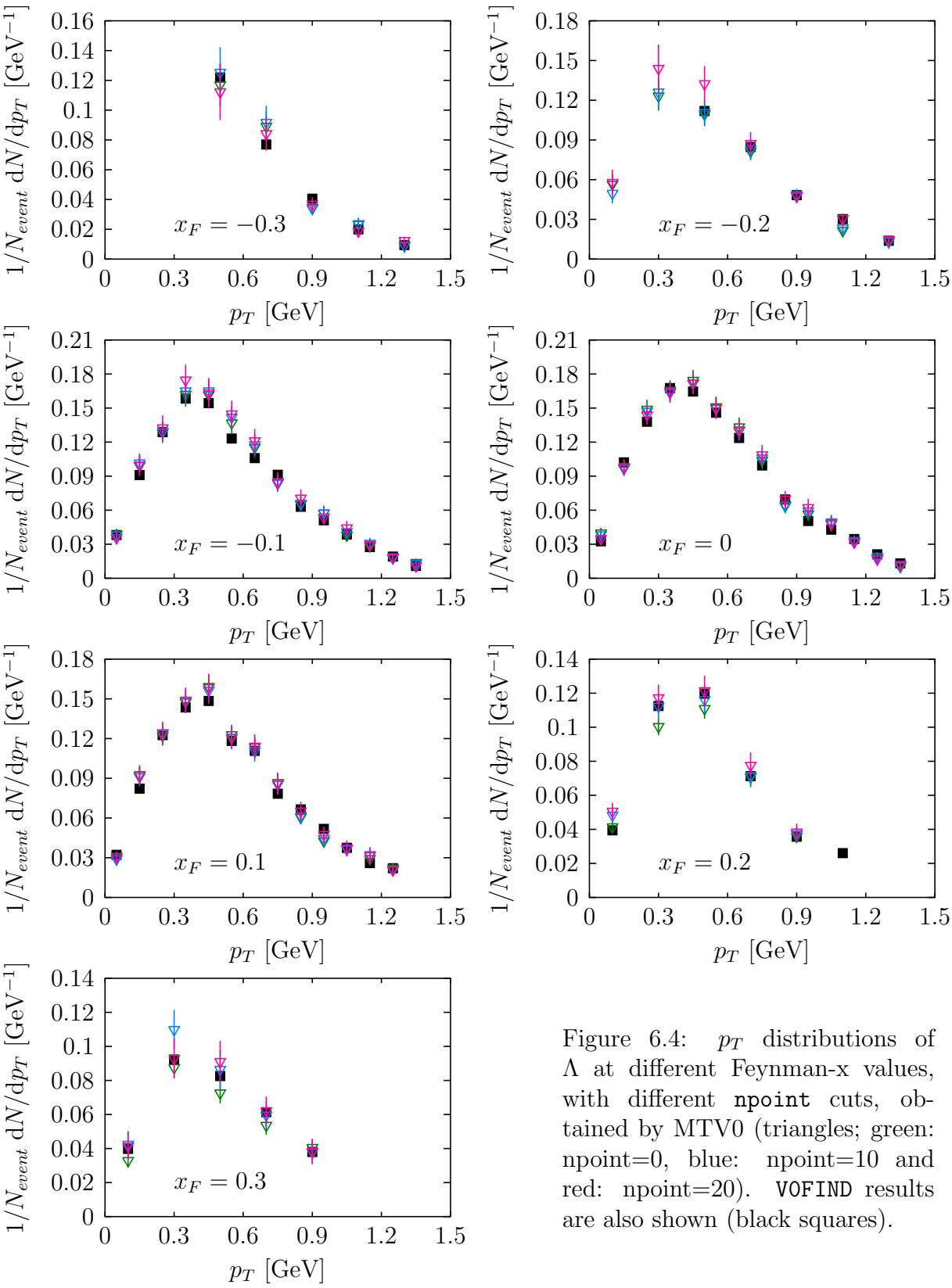

Figure 6.4: p_T distributions of Λ at different Feynman-x values, with different `npoint` cuts, obtained by MTV0 (triangles; green: npoint=0, blue: npoint=10 and red: npoint=20). `VOFIND` results are also shown (black squares).

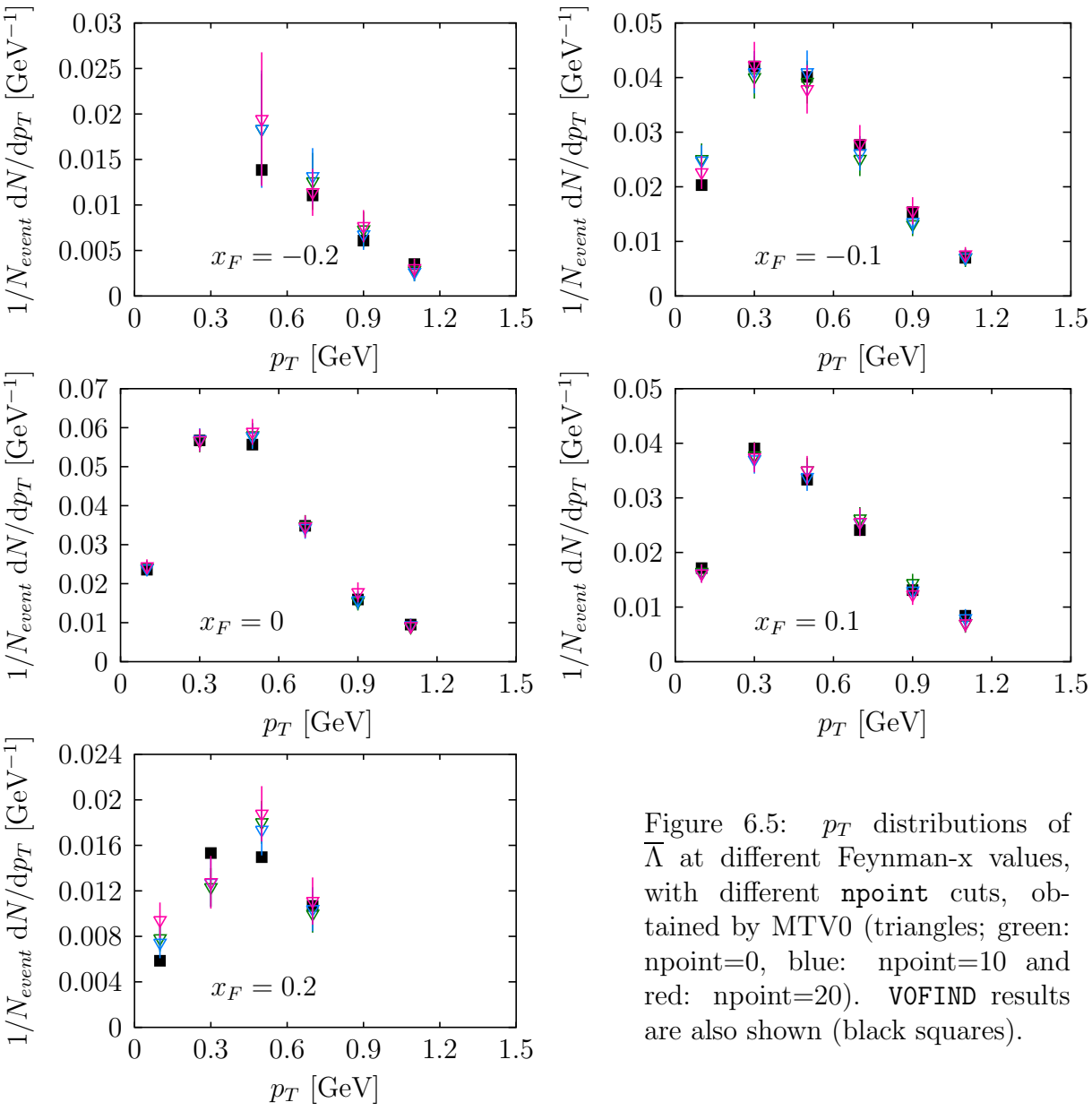

Figure 6.5: p_T distributions of $\overline{\Lambda}$ at different Feynman-x values, with different `npoint` cuts, obtained by MTV0 (triangles; green: npoint=0, blue: npoint=10 and red: npoint=20). `VOFIND` results are also shown (black squares).

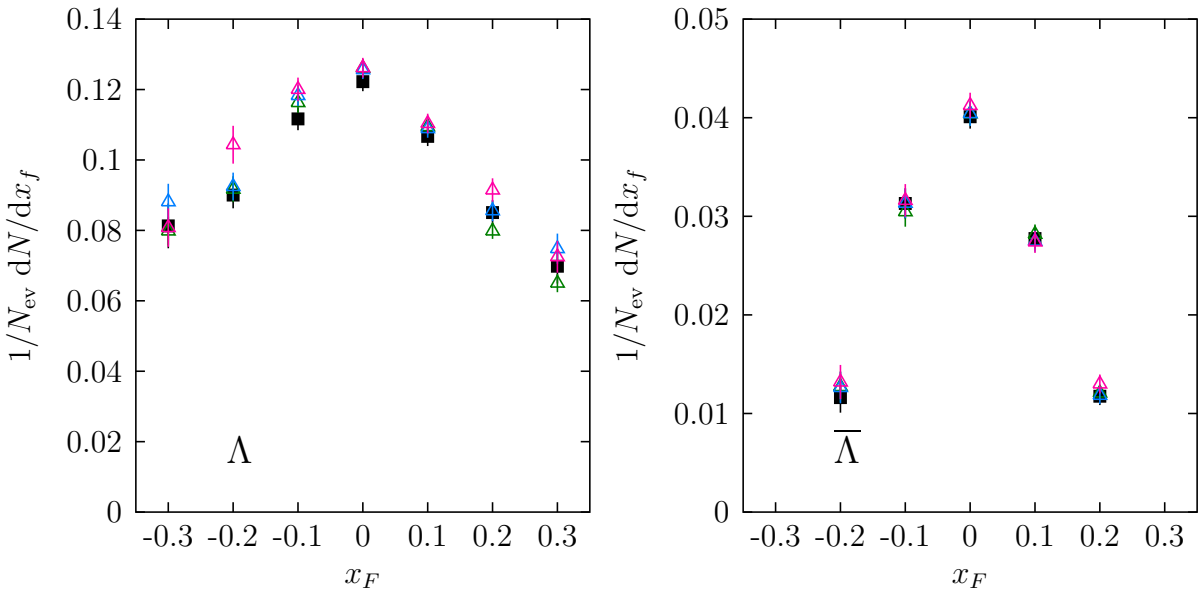

Figure 6.6: Λ and $\overline{\Lambda}$ Feynman-x distributions obtained by `MTVO` (with `npoint` = 0 (green), 10 (blue) and 20 (red) cuts), together with `VOFIND` results (black)

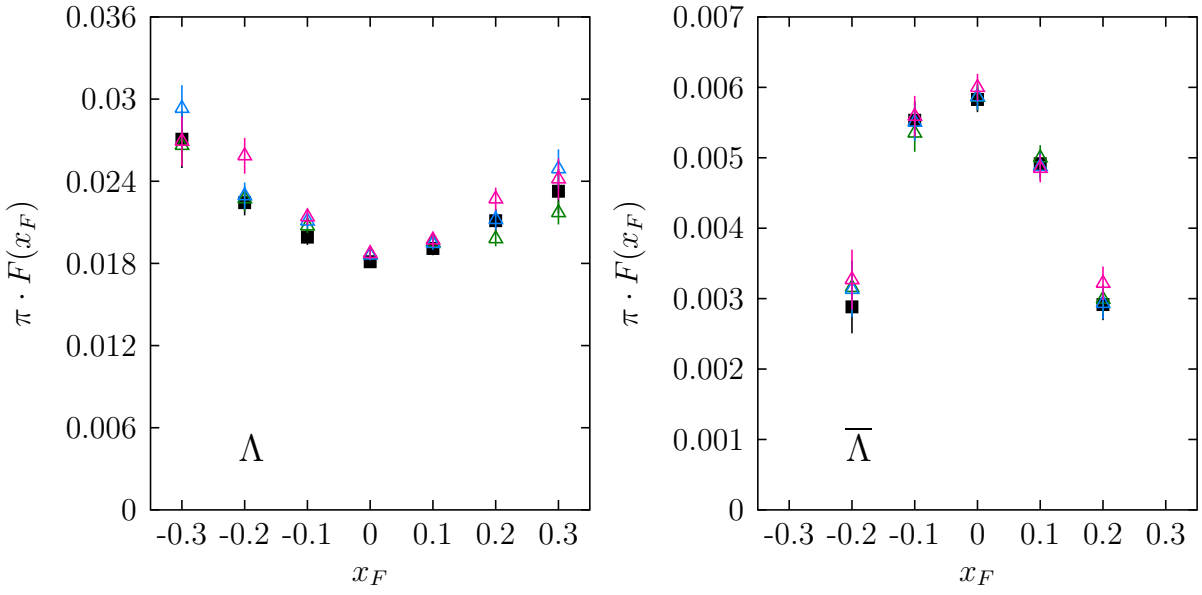

Figure 6.7: Λ and $\overline{\Lambda}$ invariant Feynman-x distributions obtained by `MTVO` (with `npoint` = 0 (green), 10 (blue) and 20 (red) cuts), together with `VOFIND` results (black)

6.2 Ξ Results

The studied Feynman-x range for Ξ^- ($\overline{\Xi}^+$) particles extended from -0.25 to 0.25 (-0.15 to 0.15); the rapidity range was [-1.25:1.25] ([-0.75:1.25]). The available statistics for Ξ^- and $\overline{\Xi}^+$ was much lower than the Λ- or $\overline{\Lambda}$-statistics. In the studied Feynman-x and rapidity ranges there were 690 and 660 Ξ^- and 270 and 260 $\overline{\Xi}^+$ candidates over the background. Such a low statistics did not allow to divide the momentum space into rapidity–p_T or Feynman-x–p_T bins simultaneously. Therefore in order to obtain the longitudinal spectra (rapidity or Feynman-x), the number of candidates was determined within a rapidity or Feynman-x bin using the whole p_T range. Correction factors were also determined for each rapidity or Feynman-x bin without subdividing these bins in p_T. Similarly the transverse momentum distributions were derived using a wide rapidity range. The yields obtained by this approach might of course depend on the physics model behind the simulation. This will be discussed in section 6.5.

6.2.1 Rapidity and Feynman-x Distributions

Figures 6.8 and 6.9 show the measured rapidity and Feynman-x distributions of Ξ^- and $\overline{\Xi}^+$.

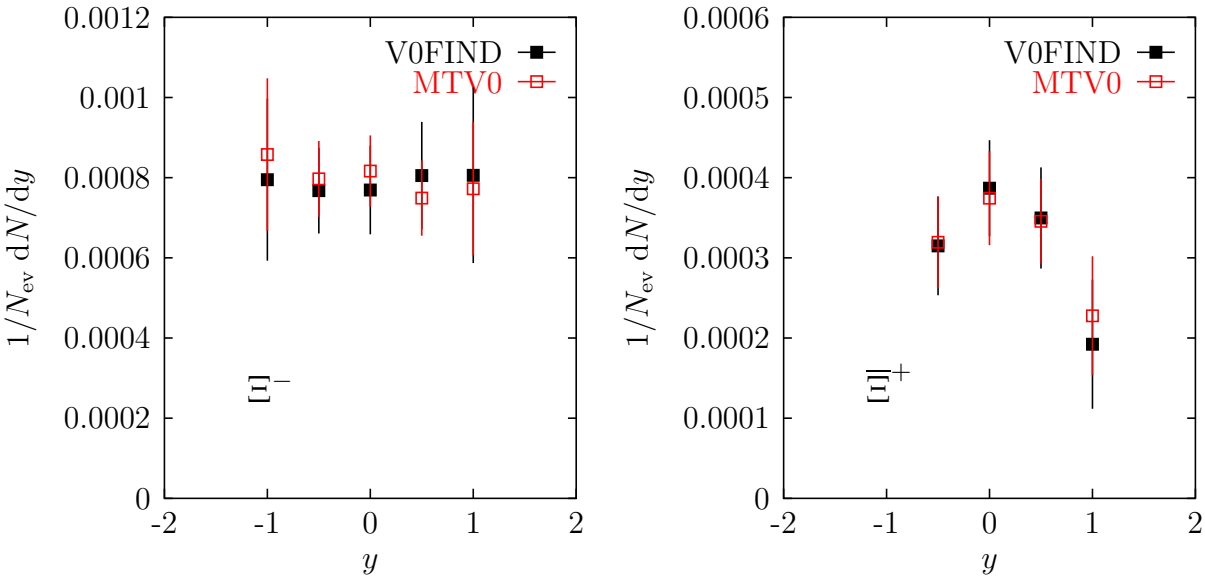

Figure 6.8: The measured rapidity spectra of Ξ^- and $\overline{\Xi}^+$ particles using `VENUS`-generated Monte Carlo events to calculate the correction factors

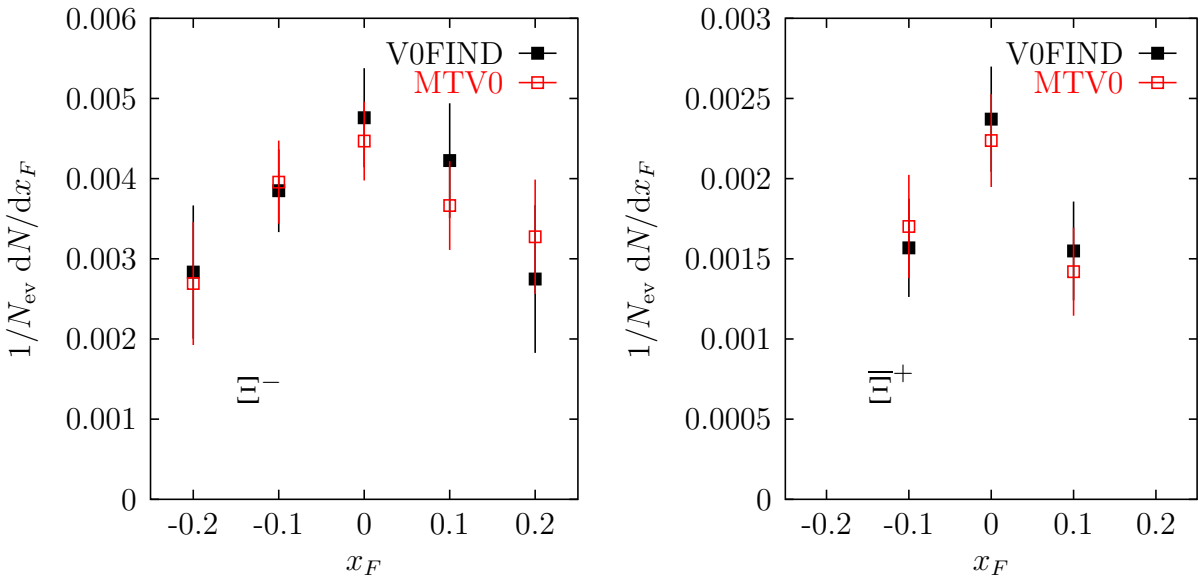

Figure 6.9: The measured Feynman-x spectra of Ξ^- and $\overline{\Xi}^+$ particles using VENUS-generated Monte Carlo events to calculate the correction factors

6.2.2 Transverse Spectra

Figure 6.10 the measured p_T distributions of Ξ^- and $\overline{\Xi}^+$ in a wide rapidity range [-0.75:0.75]. The available statistics of Ξ^- and $\overline{\Xi}^+$ particles was sufficient to create p_T distributions only in this wide rapidity range. VOFIND+XI_FIND and MTV0 results are again in agreement.

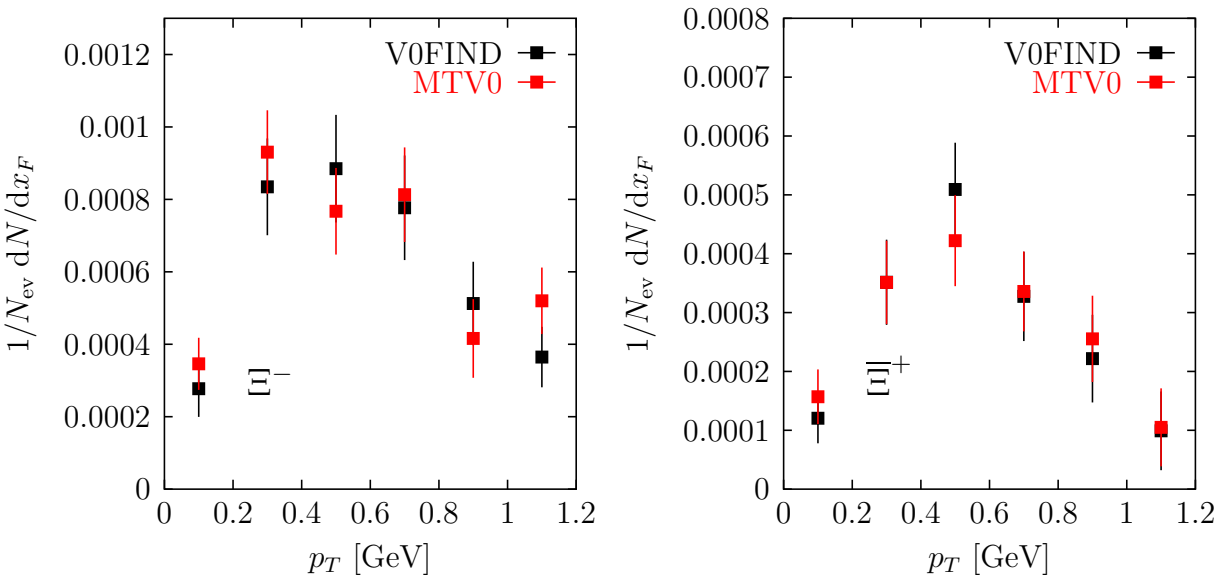

Figure 6.10: p_T spectrum of Ξ^- (left) and $\overline{\Xi}^+$ (right) particles in the rapidity range [-0.75;0.75]

6.3 $\Xi \rightarrow \Lambda$ Feeddown Correction

The Λ and $\overline{\Lambda}$ results presented so far are not the phase-space distributions of primarily created particles; they contain the contributions of Λs and $\overline{\Lambda}$s originating from the decay of Ξs or other resonances (Σs). Feeddown-correction means the subtraction of the estimated contribution by these particles.

Short-lived resonant states (the Σ resonances) do not have an observable decay length; they decay immediately at the primary vertex, and their contribution should be estimated by creating the invariant mass spectra of $\Lambda\gamma$ (for Σ^0) or $\Lambda\pi^{\pm}$ pairs (for $\Sigma^{\pm}(1385)$). In these studies one should take into account the probability of detecting both daughters of the sigma as well, which would require detailed simulations. The detection of γ particles is also not a simple task. Estimation of the contribution to the Λ and $\overline{\Lambda}$ spectra by the Σ^0 and $\Sigma^{\pm}(1385)$ resonances exceeded the framework of this thesis. The final results presented here contain the contribution by these resonances.[1]

Since the study of Ξ^- and $\overline{\Xi}^+$ particles was one of the topics of this thesis, the estimation of their contribution was a much smaller effort for the author – though this procedure is not simply the subtraction of Ξ^- or $\overline{\Xi}^+$ spectra from that of the lambdas.

[1]Most published results on lambda production contain the contribution by the Σ resonances. Only a few have an estimation about the Σ feeddown correction [26,30,37,42,43]

Lambdas, which are decay products of Ξ^-s, travel "within the Ξ", until it decays; their clock of life begins to turn back only from this moment. Such Λs will therefore decay farther from the primary vertex in average. The applied cuts (especially the cuts applied for the z coordinate of the vertex) will have different effects on them.

In order to derive the number of detected Λs and $\overline{\Lambda}$s originating from Ξ^-s and $\overline{\Xi}^+$s, the measured Ξ^- and $\overline{\Xi}^+$ distributions and the Ξ^- and $\overline{\Xi}^+$ Monte Carlo files were used. The momentum space was divided into rapidity–p_T (or x_F–p_T) bins. Since the low statistics of Ξ^-s and $\overline{\Xi}^+$s did not allow to measure the Ξ^- and $\overline{\Xi}^+$ yields in rapidity–p_T (or x_F–p_T) bins, it was assumed that the p_T distribution has a universal shape at different rapidities (or Feynman-x values):

$$\left.\frac{\mathrm{d}N}{\mathrm{d}p_T}\right|_{(y|x_F)} = A(y|x_F) \cdot p_T \cdot \exp\left(-\frac{\sqrt{p_T^2 + m_\Xi^2}}{T}\right) \tag{6.4}$$

where the T parameter is independent from rapidity or Feynman-x (but depending on what is used as the longitudinal variable – x_F or y – it has different values, see the following table), and $A(y|x_F)$ is a rapidity- (or Feynman-x) dependent normalization factor chosen in such a way that the integrated p_T distribution, eq. (6.4) gives the measured yield (per inelastic event) in that rapidity or Feynman-x bin. The measured Ξ^- and $\overline{\Xi}^+$ yields (per inelastic event) in the rapidity and x_F bins were derived by smoothing the averaged results of `VOFIND` and `MTVO`, and will be denoted by $Y(y|x_F, p_T)$ (the method to average the results of the two finders, and the averaged results will be presented in a later section: 7.1). The T parameters were chosen to be

Ξ^-		$\overline{\Xi}^+$	
Rapidity	Feynman-x	Rapidity	Feynman-x
170 MeV	150 MeV	150 MeV	130 MeV

(The sensitivity of the feeddown correction to the T parameter was checked by varying T by up to 30 MeV. The change caused by this was on the level of half a percent).

Let $M(y|x_F, p_T)$ denote the number of the simulated Ξ^- or $\overline{\Xi}^+$ particles in the y–p_T or x_F–p_T bin, and let $R(y|x_F, p_T)$ be the ratio between this number and the measured Ξ^- or $\overline{\Xi}^+$ yield in the same bin:

$$R(y|x_F, p_T) = \frac{Y(y|x_F, p_T)}{M(y|x_F, p_T)} \tag{6.5}$$

These factors account for the difference between the momentum-distributions of the measured and simulated cascade particles, and give a direct way to scale the absolute number of simulated particles to the measured number of particles per inelastic event.

As the next step all simulated Λs ($\overline{\Lambda}$s) originating from Ξ^-s ($\overline{\Xi}^+$s) were counted, which were reconstructed and fulfilled the same selection criteria applied for the real lambdas. During this counting the Λs were weighted by the previously calculated $R(y|x_F, p_T)$ factors corresponding to the rapidity (or Feynman-x) and p_T of their *parent* Ξ^- ($\overline{\Xi}^+$) particle. This method gives the number of detected Λs or $\overline{\Lambda}$s per event, originating from cascades in a $y - p_T$ or $x_F - p_T$ bin. These numbers were then multiplied by the correction factors defined in equation (5.7), and then subtracted from the Λ or $\overline{\Lambda}$ yields in the corresponding momentum bin. Since Ξ^0 has a different lifetime than Ξ^- ($c_\tau(\Xi^0) = 8.7$ cm, $c_\tau(\Xi^-) = 4.9$ cm), extra Monte Carlo events, containing Ξ^0 (or $\overline{\Xi}^0$) particles had to be generated as well, in order to study the detection efficiency of Λs ($\overline{\Lambda}$s) originating from a Ξ^0 ($\overline{\Xi}^0$). The same procedure (as described above for Ξ^-s) was applied. Since Ξ^0 particles have not yet been measured in proton-proton collisions, their momentum distribution could only be estimated. The following approaches were used:

Ξ^0: As a rough estimation the Ξ^0 yield can be taken to be the same as the Ξ^- yield. Another approach is to use simple-minded quark counting arguments: both the Ξ^- and Ξ^0 have two strange quarks (which are newly created in the interaction). The third quark (d or u) of the Ξ^- and Ξ^0 particles, can originate from the projectile or target proton. Since the proton consists of 2 u and 1 d quarks, it is 2 times more probable, that the two s quarks will be accompanied by a u quark (forming a Ξ^0), rather than by a d quark (forming a Ξ^-).

$\overline{\Xi}^0$: Consisting of antiquarks, none of the $\overline{\Xi}^-$ and $\overline{\Xi}^0$ have common quarks with the target or projectile proton. All of their constituents have to be newly created in the collisions. They differ by their non-strange $\overline{u}$ and $\overline{d}$ quarks. Assuming that the production probabilities of these antiquarks are the same, a simple approach is to take the $\overline{\Xi}^0$ yield to be the same as the $\overline{\Xi}^+$ yield. On the other hand, one can also assume, that $\overline{u}$ production is less probable than $\overline{d}$ production: the phase space is initially populated with more u quarks than d quarks, and therefore $d\overline{d}$ production might be favored over $u\overline{u}$ creation. As an extreme one can assume, that the $\overline{\Xi}^0$ production cross section is 0.

Considering these arguments, the following assumptions were made on the neutral cascade production:

$$\Xi^- < \Xi^0 < 2 \cdot \Xi^- \tag{6.6a}$$

$$0 < \overline{\Xi}^0 < \overline{\Xi}^+ \tag{6.6b}$$

and the longitudinal and transverse distributions of them were assumed to be the same as those of the Ξ^- and $\overline{\Xi}^+$.

In order to get the feeddown-corrected longitudinal spectra, the original procedure was applied again: in each rapidity or Feynman-x bin the feeddown-corrected yields in the measured p_T-bins were summed up. The yields in the unmeasured p_T bins were estimated as the integral of the function (6.1) fitted to the measured points. The resulting rapidity– and Feynman-x–distributions of Λs and $\overline{\Lambda}$s obtained by `MTV0` and `V0FIND` are shown in figures 6.11 and 6.12. For the shown `MTV0` result the `npoint`=20 cut was applied. Results obtained by the other `npoint` cuts agreed with the presented one within errors. For simplicity `V0FIND` results are presented only with symbols (instead of the uncertainty band) at the average between the two extremes (eq. 6.6)

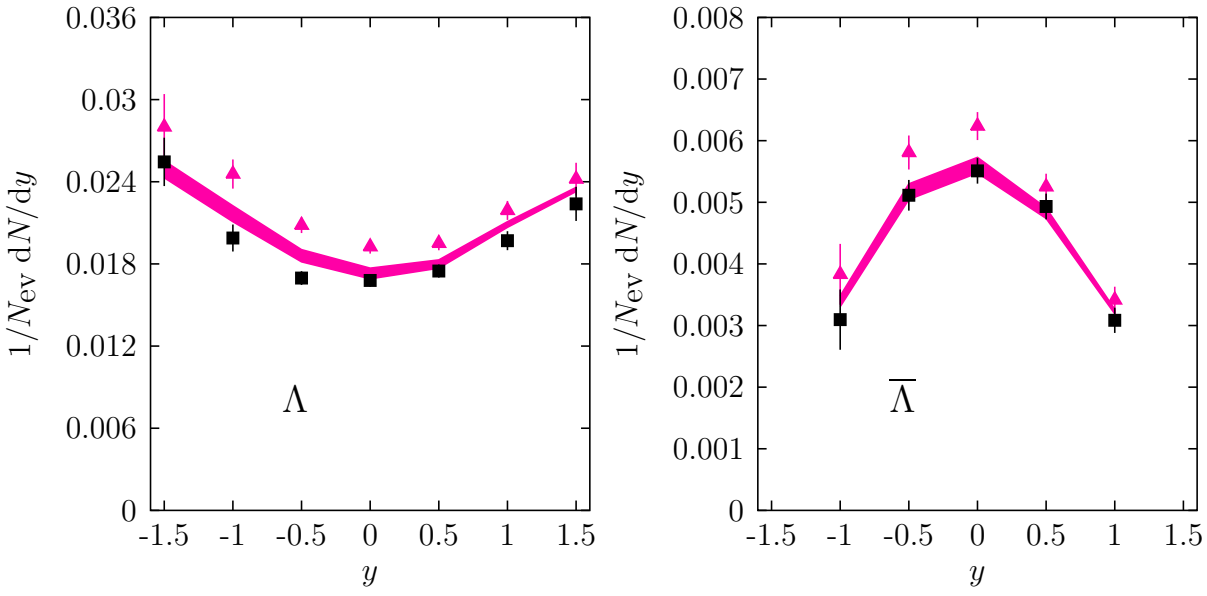

Figure 6.11: Feeddown-corrected rapidity distribution of Λs and $\overline{\Lambda}$s. MTV0 results are shown in red: triangles represent the result without feeddown correction, and the shadowed band represents the uncertainty due to the unknown Ξ^0 ($\overline{\Xi}^0$) distribution, see text for details. Feeddown-corrected V0FIND results are shown in black.

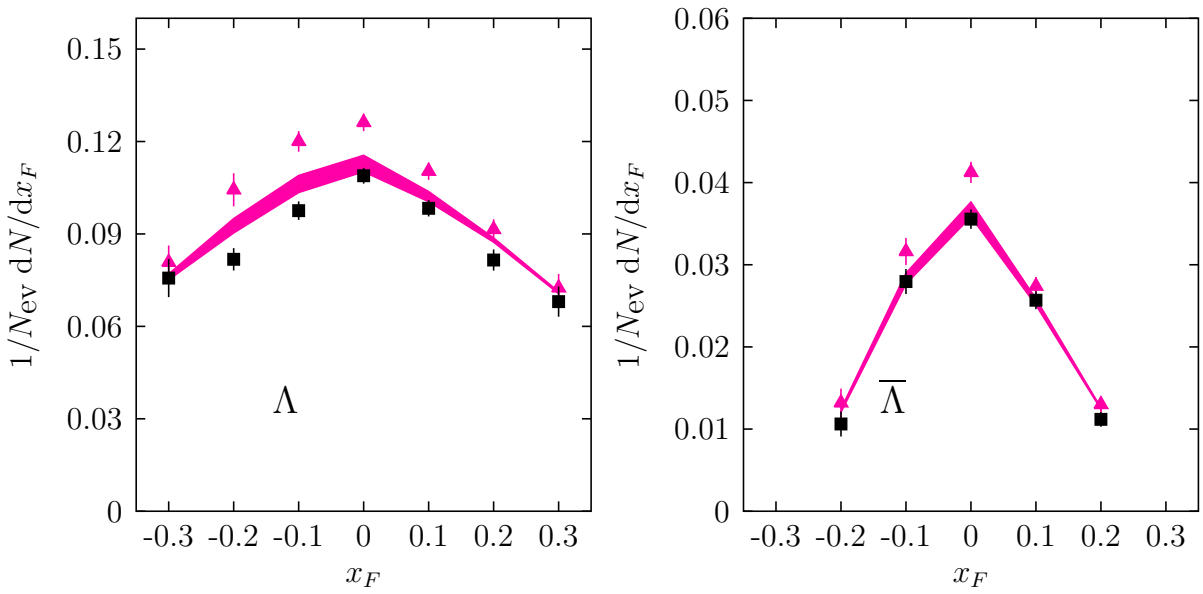

Figure 6.12: Feeddown-corrected Feynman-x distribution of Λs and $\overline{\Lambda}$s. `MTVO` results are shown in red: triangles represent the results without feeddown correction, and the shadowed band represents the uncertainty due to the unknown Ξ^0 ($\overline{\Xi}^0$) distribution, see text for details. Feeddown-corrected `VOFIND` results are shown in black.

The feeddown correction is increasing towards the backward hemisphere, and there slightly exceeds 10%. Feeddown-corrected results obtained by `MTVO` and `VOFIND` are found to be consistent.

6.4 Ω Results

Ω particles are created so rarely in proton-proton collisions, that measuring their phase-space distribution could not be done. The applied cuts had to be tuned in order to reach the clearest Ω peak. The following cuts were applied: only candidates with rapidity between -0.7 and 0.7 were used. The backwards extrapolated Ω trajectory had to approach the primary vertex (*impact parameter*) in the x and y directions (b_x and b_y) by less than 1.2 cm and 1 cm, respectively. The invariant mass of the Λ ($\overline{\Lambda}$) daughter had to be in the range $m_\Lambda \pm 0.02$ GeV. In order to exclude combinations of kaons, the V^0 daughter's invariant mass with a K^0_S hypothesis had to be outside of the range $m_K \pm 0.01$ GeV. The V^0 and the Ω decay vertices had to be separated from each other by at least 4 cm in the z direction, and the Ω vertex had to be at $z > -570$ cm. These cuts are summarized in the following table.

Rapidity range	-0.7 $< y <$ 0.7
Impact parameter of extrapolated trajectory at the main vertex	$\lvert b_x \rvert <$ 1.2 cm $\lvert b_y \rvert <$ 1 cm
V^0 daughter's mass (Λ)	within $m_\Lambda \pm 0.02$ GeV
V^0 daughter's mass (with K^0_S hypothesis)	outside of $m_K \pm 0.01$ GeV
V^0 and Ω vertex separation	4 cm
z coordinate of Ω vertex	> -570 cm

In addition the statistics was so low, that it had no sense to make a separate analysis of the Ω particles with `VOFIND` and `MTVO`. Therefore `MTVO` was operated in *additional* mode, and looked only for such combinations, which were not found by `VOFIND`. Figure 6.13 shows the omega and antiomega mass spectra. For the Ω^- the results of both finders are shown separately as well; a small signal is visible in the case of both finders, which are only slightly larger than the fluctuations. The signal in the combined spectrum is much more significant. This is the first time that the Ω^- particle observed in proton-proton collisions, with sufficient statistics for a cross section determination. The $\overline{\Omega}^+$ mass spectrum is compatible with the absence of the antiomega peak. The Ω^- cross section and the estimation of the upper limit of the $\overline{\Omega}^+/\Omega^-$ ratio will be presented in the following chapter ('Discussion'; see section 7.3 on page 105).

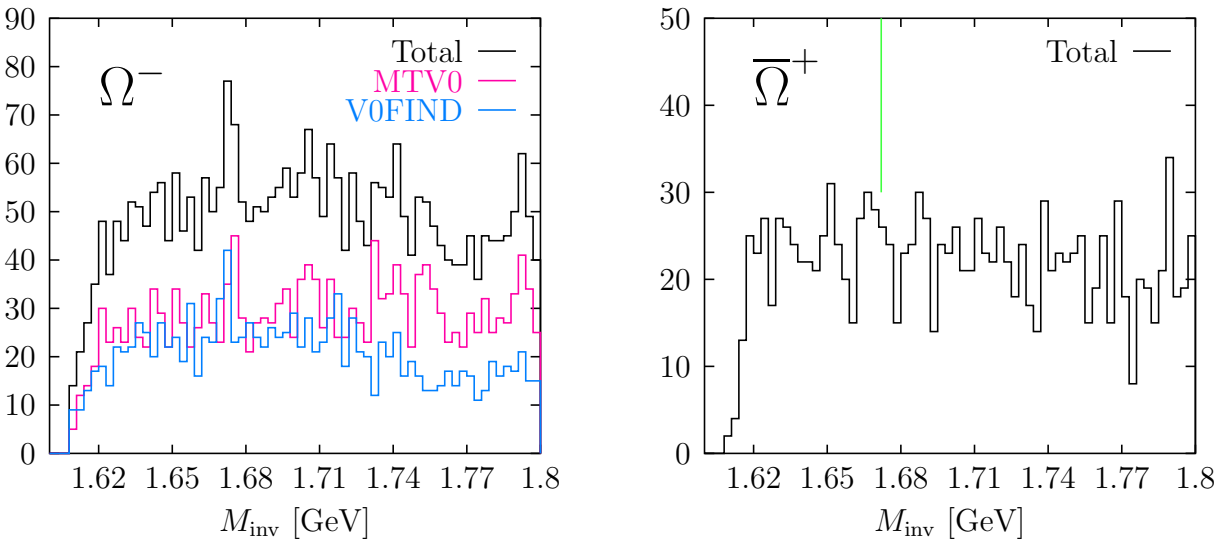

Figure 6.13: Mass spectra of Ω^- and $\overline{\Omega}^+$, using both finders

6.5 Stability of MTV0 Results

6.5.1 Stability Against the Cuts

In order to check the stability of these results against the applied `mvdz` cut (see page 49), several different values for this cut were checked (`mvdz` = 17 and 22 cm). Results were tested with no ϕ cut as well. Differences in the results did not exceed 1-2%. The effect of the number-of-points cut for the Λs and $\overline{\Lambda}$s (see page 51) was already discussed when the results were presented. The results were stable against varying the `npoint`-cut. From these results we can conclude here, that no systematic error was introduced due to the applied selection criteria.

6.5.2 Stability of the Event Weighting Procedure

The event weighting procedure described in section 5.2 (page 56) was used to eliminate the effects of the fiducial cut. As it was mentioned there, the same weights were used to create the weighted mass spectrum, and to count the number of weighted events. This assumes, that the presence of a V^0 or a cascade does not change the main vertex resolution, and therefore the effect of the fiducial cut. The same simulated events were used to check this assumption, which were used to derive the reconstruction and detection efficiency of Λs. These events were generated by `VENUS`, and each of them contained a Λ.

In order to calculate the rejection rate of events by the fiducial cut in such events, where there was a visible lambda (R^{Λ}), those simulated events were used, where the Λ decayed into the charged channel. These ratios are shown in red in figure 6.14 as a function of the detected charged multiplicity. The subpanels of this figure correspond to different rapidity regions of the Λ in the event.

In order to calculate the rejection rate of events by the fiducial cut for events not containing a Λ, those simulated events were used, where the Λ decayed into the neutral channel (and thus there was no V^0 visible in the event configuration). The ratio of all events to the number of events accepted by the fiducial cut in this subsample, $R^{\mathrm{no}\Lambda)}$ is shown in blue in figure 6.14 (this line is the same in all subpanels).

The black triangles represent the rejection rate derived from the data (by collaborators [78]; these weighting factors were used in the data analysis, see section 5.2.3). These weighting factors fall very close to the results derived from the simulation without a Λ in the events. They are slightly higher, reflecting the fact, that average p-p events contain sometimes V^0s and cascades. The green line shows the distribution of the detected charged multiplicity in the simulation (on arbitrary scale).

The increasing deviation between the red and blue lines towards low multiplicities means, that the presence of a V^0 has more effect on the main vertex reconstruction, if the number of tracks used to determine the main vertex is lower. In principal the weights corresponding to events containing a Λ (the red line) should be used for the weighted mass histogram of the Λs. That is, if we use the the same (smaller) weighting factors (the triangles) for Λs, which were derived from minimum-bias events, we underestimate the Λ cross section. In order to estimate the overall effect, the two sets of weighting factors (the red line, obtained from the simulation: $R^{\Lambda}(m)$, and the black triangles, obtained from the minimum-bias p-p events: R^{data}) were weighted with the detected charged multiplicity distribution (green line) in the simulated `VENUS`-events, in each rapidity region:

$$F^{\Lambda} = \frac{\sum_m R^{\Lambda}(m) \cdot D(m)}{\sum_m D(m)} \tag{6.7}$$

$$F^{\mathrm{data}} = \frac{\sum_m R^{\mathrm{data}}(m) \cdot D(m)}{\sum_m D(m)} \tag{6.8}$$

where the sum runs over multiplicity m, and $D(m)$ is the the prevalence of the multiplicity m (the value of the green curve at multiplicity m). The differences between these

y	-1.5	-1	-0.5	0	0.5	1	1.5
Λ	4.5±2.3	2.7±1.1	2.3±0.8	2.4±0.7	4.3±0.7	5.7±0.8	9.0±1.2
$\overline{\Lambda}$		4.9±1.5	3.7±0.8	3.4±0.7	5.0±0.7	8.1±1.1	
Ξ^-		11.2±1.4	8.7±0.8	6±0.7	6.5±0.8	6.2±1.5	
$\overline{\Xi}^+$			12.9±1.1	10.0±0.9	10.1±1.1	17.5±2.8	

x_F	-0.3	-0.2	-0.1	0	0.1	0.2	0.3
Λ	2.5±2.3	2.8±1.4	2.3±0.8	3.6±0.6	4.8±0.7	7.1±1.0	8.2±1.4
$\overline{\Lambda}$		3.6±1.9	4.5±0.9	4.1±0.6	4.8±0.7	9.1±1.3	
Ξ^-		10.5±1.6	9.7±0.9	6.9±0.7	6.6±0.8	4.9±1.5	
$\overline{\Xi}^+$			13.6±1.2	10.6±0.9	10.8±1.2		

Table 6.1: Summary of the systematic error estimations (in %) of the event weighting procedure (the errors indicate the uncertainty due to the limited statistics of the simulated events)

two results are systematic errors (underestimation) of the production cross sections. These are summarized in table 6.1.

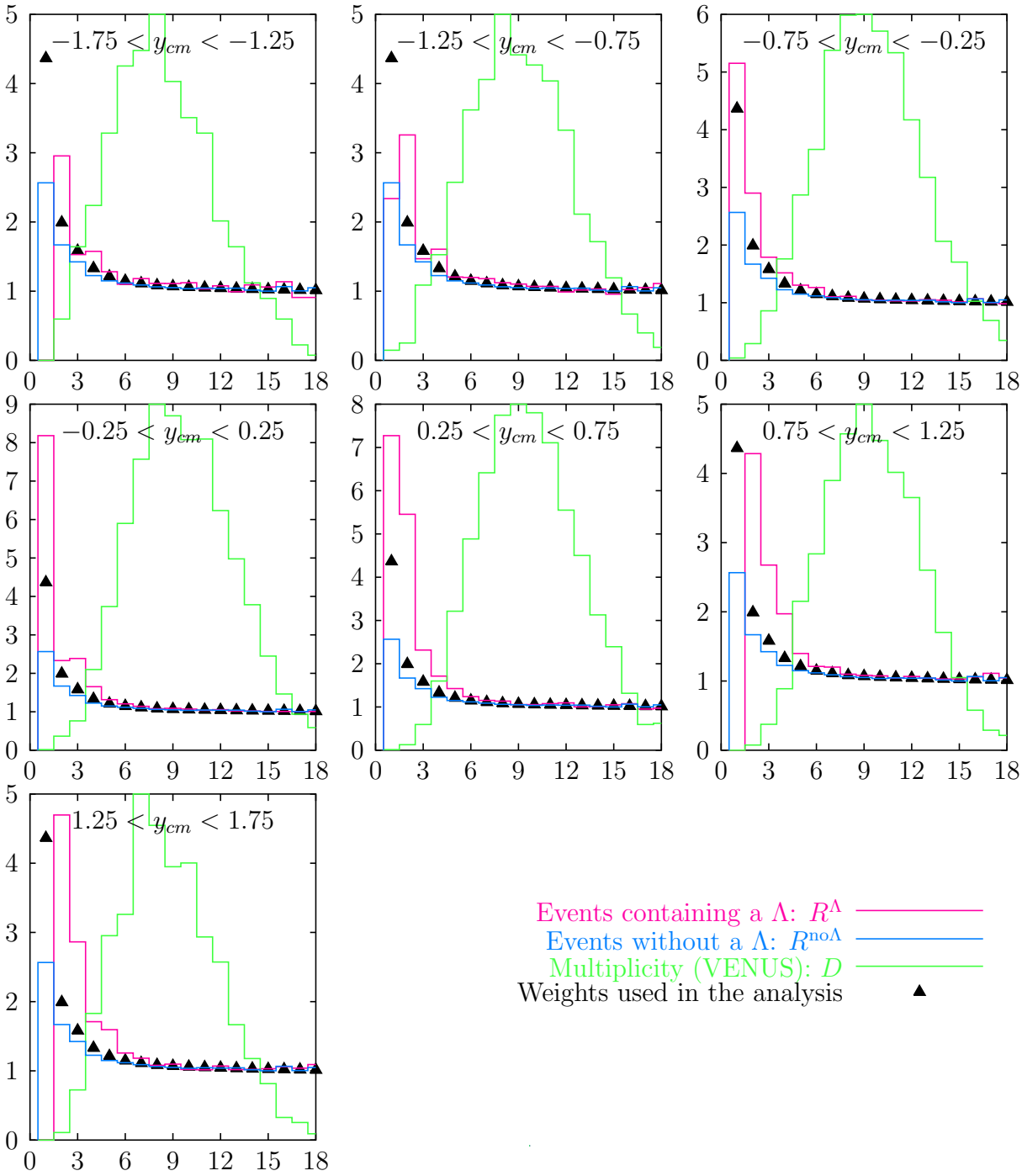

Figure 6.14: The ratio of all events to the number of accepted events by the fiducial cut (the event weight, vertical axis), as a function of detected charged multiplicity (horizontal axis) – simulation. The red line shows the results for events containing a Λ, the blue line shows the same ratio for events without a Λ (see text for details). The black symbols represent the weights derived from the data, which were used to calculate the cross sections. The green line is the multiplicity distribution for such events in the simulation, which had an accepted Λ candidate.

6.5.3 Stability of the Ξ^- Results

Since the low statistics of Ξ^- and $\overline{\Xi}^+$ was not enough to make a rapidity–p_T or x_F–p_T binning, the *overall* correction factors (derived in a rapidity or x_F bin without subdivision in p_T, or vice versa) will depend on the momentum distribution of the simulated particles. For example different transverse distributions of the simulated particles will give different weight to the various p_T regions within a rapidity– or x_F-bin, and if the acceptance is not flat within this bin, this will lead to different correction factors. Figure 6.15 shows the correction factors for Ξ^- obtained from the VENUS simulation at different rapidities and Feynman-x values, as a function of p_T. The figure indicates, that the acceptance is least uniform as a function of p_T at midrapidity and x_F=0: from p_T=0 GeV to p_T ≈1.4 GeV it increases by more than a factor of 2. A simulation with a smaller average p_T of the generated particles will therefore predict a smaller correction factor (and smaller yield) at midrapidity and x_F=0, than a simulation using a larger average p_T. The non-uniformity of the acceptance as a function of p_T is less striking at other rapidities and x_F values.

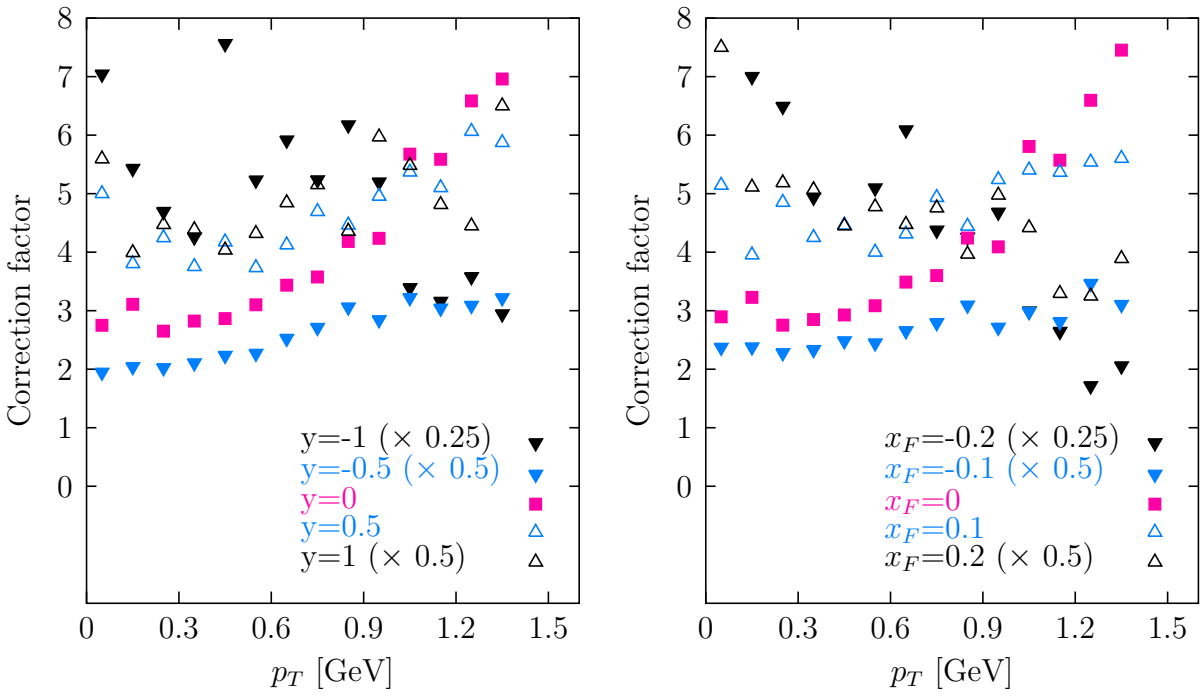

Figure 6.15: Correction factors for Ξ^- as a function of p_T at different rapidities (the correction factors for $\overline{\Xi}^+$s are the same within errors; correction factors are scaled at some rapidities and x_F values.)

In order to estimate the sensitivity of the results to the transverse distribution of the simulated particles, another event generator (FRITIOF, [77]) was used. As figure 6.16 shows, the transverse distributions generated by the VENUS and FRITIOF models were rather different, and the experimental results are not accurate enough to determine the real transverse momentum distribution of them. The sensitivity of the results in a rapidity or Feynman-x bin was determined as follows: let F_i^{gen} denote the number of particles generated by FRITIOF in the ith p_T bin. The number of reconstructed and accepted particles in this bin is calculated as $F_i^{\mathrm{acc}} = A_i^{\mathrm{V}} F_i^{\mathrm{gen}}$, where A_i^{V} is the acceptance in the ith p_T bin, previously calculated using the VENUS Monte Carlo file. The "FRITIOF correction factor" in the rapidity or Feynman-x bin is then defined as $C^{\mathrm{F}} = \sum_i F_i^{\mathrm{gen}} / \sum_i F_i^{\mathrm{acc}}$. This approach made it possible to use only a small sample of FRITIOF-generated events, without even reconstructing them. Figure 6.17 shows the ratio of the "FRITIOF–" and "VENUS correction factors". As the plot shows, using the FRITIOF model as input to the simulation, we would get by approximately 15% lower correction factors at midrapidity (or x_F=0), and slightly higher correction factors at the edges of our longitudinal acceptance. This has no serious consequences concerning the shape of the $\overline{\Xi}^+$ distributions: they would anyway be peaked at midrapidity or x_F=0. The Ξ^- rapidity distribution (which is consistent with being flat) would however show a minimum at midrapidity.

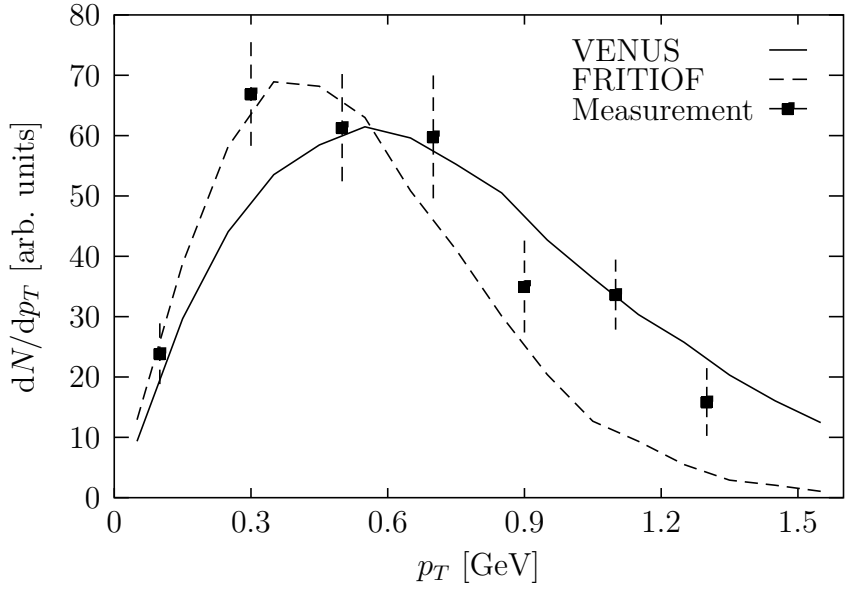

Figure 6.16: p_T distributions of Ξ^- particles generated by VENUS and FRITIOF.

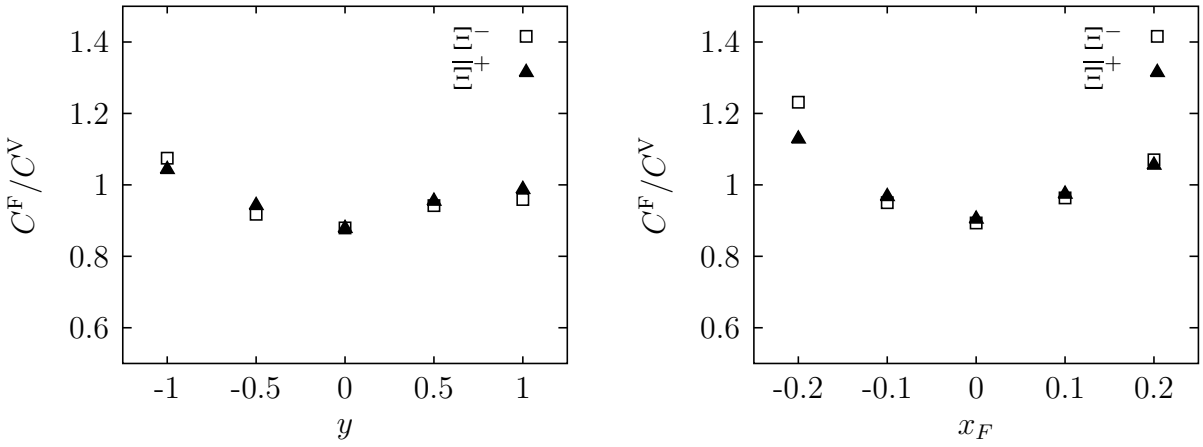

Figure 6.17: Ratio of correction factors derived from a FRITIOF (C^{F}) and VENUS (C^{V}) simulation for Ξ^-s and $\overline{\Xi}^+$s as a function of rapidity (left panel) and Feynman-x (right panel)

6.5.4 Averaging Between the two Finders

Having two (to some extent independent) finders to derive the same physical quantities is not only useful to make cross-checks; differences between the two results can also be used for the estimation of the errors of the results. The method used to derive the final results (presented in the following chapter) is based on [74], and will be shortly described here, together with an illustrative example.

Let $\{x_i\}$ be a set of n measurements of a parameter μ with expectation values and covariance matrix

$$\langle x_i \rangle = \mu \tag{6.9}$$

$$C_{ij}(x) = \langle (x_i - \mu)(x_j - \mu) \rangle = \langle x_i x_j \rangle - \mu^2 \tag{6.10}$$

From the measured values $\{x_i\}$ an estimator $\overline{x}$ for μ can be constructed by minimizing

$$\chi^2 = \sum_{i,j} (x_i - \overline{x})(x_j - \overline{x}) C_{ij}^{-1}(x) \tag{6.11}$$

Note that χ^2 is by construction invariant with respect to an arbitrary linear transformation of the variables x_i. In case the $\{x_i\}$ values are independent, the covariance matrix

becomes diagonal: $C_{ij}(x) = \sigma_i^2 \delta_{ij}$, and equation (6.11) simplifies to

$$\chi^2 = \sum_i \frac{(x_i - \overline{x})^2}{\sigma_i^2} \tag{6.12}$$

The value $\overline{x}$, which minimizes χ^2 is found to be

$$\overline{x} = \sum_i w_i x_i \quad \text{with} \quad w_i = \frac{1/\sigma_i^2}{N} \quad \text{and} \quad N = \sum_k \frac{1}{\sigma_k^2} \tag{6.13}$$

The variance of $\overline{x}$ is obtained by standard error propagation:

$$C(\overline{x}) = \sigma^2(\overline{x}) = \sum_{i,j} w_i w_j C_{ij} = \sum_i w_i^2 \sigma_i^2 = 1/N \tag{6.14}$$

The expectation value of χ^2 at the minimum ($\overline{x}$) is found to be

$$\left\langle \chi^2_{\text{min}} \right\rangle = \sum_i \left\langle \frac{(x_i - \overline{x})^2}{\sigma_i^2} \right\rangle = \sum_i \frac{\langle x_i^2 \rangle}{\sigma_i^2} - N \left\langle \overline{x}^2 \right\rangle = n - 1 \tag{6.15}$$

Note that although the value of $\langle \chi^2 \rangle$ has been derived for a diagonal covariance matrix, this expression is valid in general since one can always diagonalize C_{ij}, and χ^2 is by construction invariant to such a transformation.

A weighted average as defined in (6.13) with the weights w_i (which are subject to the constraint $\sum_i w_i = 1$) has a variance as defined in eq. (6.14). The choice of the w_i weights shown in eq. (6.13) does not only minimize the χ^2 in (6.11), but also the variance of $\overline{x}$ in eq. (6.14), if the individual measurements are uncorrelated.

In case there are correlations present, the formally optimal result (obtained by minimizing eq. 6.11) requires the knowledge of C_{ij}^{-1} and therefore the off-diagonal elements of C_{ij} have to be known precisely. Therefore in practical applications one might prefer the robust average eq. (6.13), even if it's no longer the value, which minimizes (6.11). This will be used as an estimator of μ.

While it is meaningful to calculate a weighted average ignoring off-diagonal elements of the covariance matrix, the full matrix C_{ij} should be taken into account for the variance of the average. Since the correlation between measurements is often difficult to quantify, a different approach is used.

In order to estimate the variance of $\overline{x}$, the actual value of χ^2 (as defined in equation 6.12) is compared to its expectation value (6.15).

A value χ^2 larger than its expectation value can result if anti-correlations are present, or if the measurement errors are underestimated. In case of the latter, $1/N$ from eq. (6.14) underestimates the variance of $\overline{x}$; in the former case it is overestimated. In order not to derive a variance, which underestimates the real error of our result, the common practice is to take the more pessimistic choice; that is, to assume, that the too large value of χ^2 is a consequence of too small measurement errors, and apply a common scaling factor $\chi^2/(n-1)$ to all errors in order to obtain a χ^2 identical to its expectation value. The variance of $\overline{x}$ then gets $\sigma^2(\overline{x}) = C(\overline{x}) = 1/N \cdot \chi^2/(n-1)$.

A value χ^2 smaller than its expectation value can indicate, that the measurement errors are overestimated, or there are positive correlations between the data. While the former would imply that the error of $\overline{x}$ in reality is smaller then the estimate $1/N$, the latter would require a larger error. Taking again the more pessimistic approach, we try to derive an estimate for the larger error. Without loss of generality we can assume that $\langle x_i \rangle = \langle \overline{x} \rangle = 0$. This implies $\langle x_i^2 \rangle = \sigma_i^2$ and $\langle \overline{x}^2 \rangle = C(\overline{x})$, and the expectation value $\left\langle \chi^2_{\min} \right\rangle$ in eq. (6.15) simplifies to

$$\left\langle \chi^2_{\min} \right\rangle = n - NC(\overline{x}) \tag{6.16}$$

If the individual measurements are uncorrelated, then $C(\overline{x}) = 1/N$, and this result, (6.16) gives $n-1$, in accordance with (6.15). If there are reasons to suspect that the measurements x_i are correlated, then one can reinterpret (6.16), assuming that the actual value of χ^2, (6.12) is equal to its expectation value, and derive a variance estimate:

$$C(\overline{x}) = \frac{1}{N}(n - \chi^2) \tag{6.17}$$

This simple scaling prescription for the case that the χ^2 of a weighted average is smaller than expected defines an effective way to take imperfections or incomplete knowledge about the input data into account.

In our case ($n = 2$) this general approach gives the following practical procedure: the final measured particle yield in a momentum-bin is calculated from the results of

the two finders (x_1 and x_2) as

$$\overline{x} = \frac{1}{N}\left(\frac{x_1}{\sigma_1^2} + \frac{x_1}{\sigma_1^2}\right) \tag{6.18}$$

where $N = 1/\sigma_1^2 + 1/\sigma_2^2$. To calculate the variance of the averaged result, one first calculates χ^2 as

$$\chi^2 = \frac{(x_1 - \overline{x})^2}{\sigma_1^2} + \frac{(x_2 - \overline{x})^2}{\sigma_2^2} \tag{6.19}$$

The variance of the averaged result is finally calculated as

$$\sigma = \begin{cases} \dfrac{1}{\sqrt{N}} \cdot \chi & \text{if } \chi^2 \geq 1 \\ \dfrac{1}{\sqrt{N}} \cdot \sqrt{2 - \chi^2} & \text{if } \chi^2 < 1 \end{cases} \tag{6.20}$$

In order to study the behavior of the variance defined this way, we will examine two cases: (1) when the difference between the results of the two finders is larger than their quoted errors (2) when the difference between the two results is smaller than the quoted errors. For simplicity we assume that the errors of the two results are approximately the same: $\sigma_1 \approx \sigma_2 \approx \sigma_{1,2}$. In this case $\overline{x}$ is the average of x_1 and x_2. We define $\Delta x = |x_1 - \overline{x}| = |x_2 - \overline{x}|$. Using these notations χ^2 and N are expressed as

$$\chi^2 = 2\frac{\Delta x^2}{\sigma_{1,2}^2} \quad \text{and} \quad N = \frac{2}{\sigma_{1,2}^2} \tag{6.21}$$

(1) If the difference between the results of the two finders is larger than their errors (to be more quantitative: $\Delta x > \sigma_{1,2}/\sqrt{2}$), then $\chi^2 \geq 1$ and therefore the resulting variance of $\overline{x}$ will be Δx. Note that this estimation of the error is indeed bigger, than what one would get by the usual combination of the errors (the naive error of the average of x_1 and x_2): $\frac{1}{2}\sqrt{\sigma_1^2 + \sigma_2^2} = \frac{1}{2}\sqrt{\sigma_{1,2}^2 + \sigma_{1,2}^2} = \sigma_{1,2}/\sqrt{2}$.

(2) If the difference between the results of the two finders is smaller than their errors ($\Delta x < \sigma_{1,2}/\sqrt{2}$), the resulting variance of $\overline{x}$ will be $\sqrt{\sigma_{1,2}^2 - \Delta x^2}$. This expression might be surprising for the first sight: a smaller difference between the two results gives a larger error estimate. Recall that a χ^2 smaller than its expectation value (a too good agreement of the individual results compared to their error) was attributed to positive

correlations, and not to the overestimation of the individual errors. In the case of two measurements this approach might seem to be needless, resulting in an unnecessary overestimation of the errors. (two measurements can by chance be very close to each other even if their errors are large; having 100 results much closer to each other than their errors would indeed indicate the presence of positive correlations). Note however, that the resulting estimate for the variance of the final result is smaller than the error of the individual results even in this pessimistic approach, but larger than the naive combination of the errors: $\sigma_{1,2}/\sqrt{2}$.

Figure 6.18 shows a schematic plot of our error estimation as a function of the difference between the two results (Δx), assuming the above conditions.

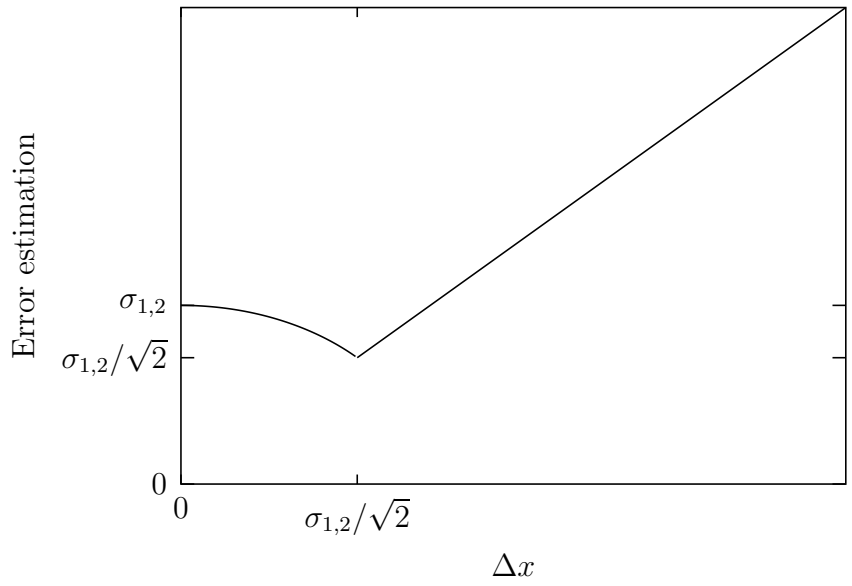

Figure 6.18: The behavior of our error estimation, eq. (6.20), as a function of the difference between the results of the two finders

Chapter 7

Final Results and Discussion

In this chapter I present the final results obtained by the previously described methods. A large part of this chapter is dedicated to the presentation of strange and multistrange particle spectra in proton-proton collisions. These are the first measurements of the Λ and $\overline{\Lambda}$ spectra by a large-statistics, large acceptance experiment, and the first ever results on multistrange baryon spectra. Therefore these results will be presented in detail. The results of other searches, which became possible only with the help of these data, will be presented afterwards.

7.1 The Final Spectra of Strange and Multistrange Particles

7.1.1 Λ and $\overline{\Lambda}$ Spectra

For the derivation of the common results, the 20-point-cut was used for `MTV0` for the Λ and $\overline{\Lambda}$ particles. Having studied the symmetricity of the results, for the derivation of the final spectra we make use of the symmetry of p-p collisions. At certain rapidities or Feynman-x values there were such p_T regions, where no measurement could be done. These p_T ranges have been completed from the corresponding rapidity or Feynman-x bin in the opposite hemisphere, if possible. The longitudinal spectra were calculated from these completed p_T distributions, in the same way as it was done before.

The presented results have been feeddown-corrected with respect to the $\Xi, \overline{\Xi} \rightarrow \Lambda$ decay. The average correction has been taken between the two extremes shown in equation (6.6).

Figures 7.1 and 7.2 show the transverse momentum distributions of Λs and $\overline{\Lambda}$s at different rapidities and Feynman-x values. In order to put all spectra in one plot, some of them were scaled. The same scaling factors were applied at corresponding y or x_F values in the opposite hemispheres, so that these spectra can be directly compared. These plots also indicate, which p_T regions have been completed from the opposite hemisphere.

The transverse momentum spectra were fitted with the function (6.1). The T parameter (inverse slope) resulting from these fits is shown as the function of rapidity or Feynman-x in figure 7.3. These results are consistent with the T parameter (the shape of the p_T spectra) being independent from the longitudinal momenta – which could already be seen in figures 7.1 and 7.2.

The rapidity, Feynman-x and invariant Feynman-x distributions (number of particles per inelastic event and unit of rapidity or x_F) of Λs and $\overline{\Lambda}$s are shown in figures 7.4, 7.5 and 7.6. In order to get the cross sections in mbarn, the results have to be scaled with the inelastic cross section of p-p collisions (31.7 mbarn at 158 GeV beam energy). The shape of the Λ rapidity distribution (minimum at y_{cm}, and increasing towards the backward and forward hemispheres) reflects the *leading baryon effect*: baryons having common quarks with the projectile or target nucleon have a tendency to have larger momenta compared to other particles. The more quarks the particle shares with the projectile or target, the more pronounced this effect will be (see the flat rapidity distribution of Ξ^- in a later section. Ξ^- shares only one quark with the projectile).

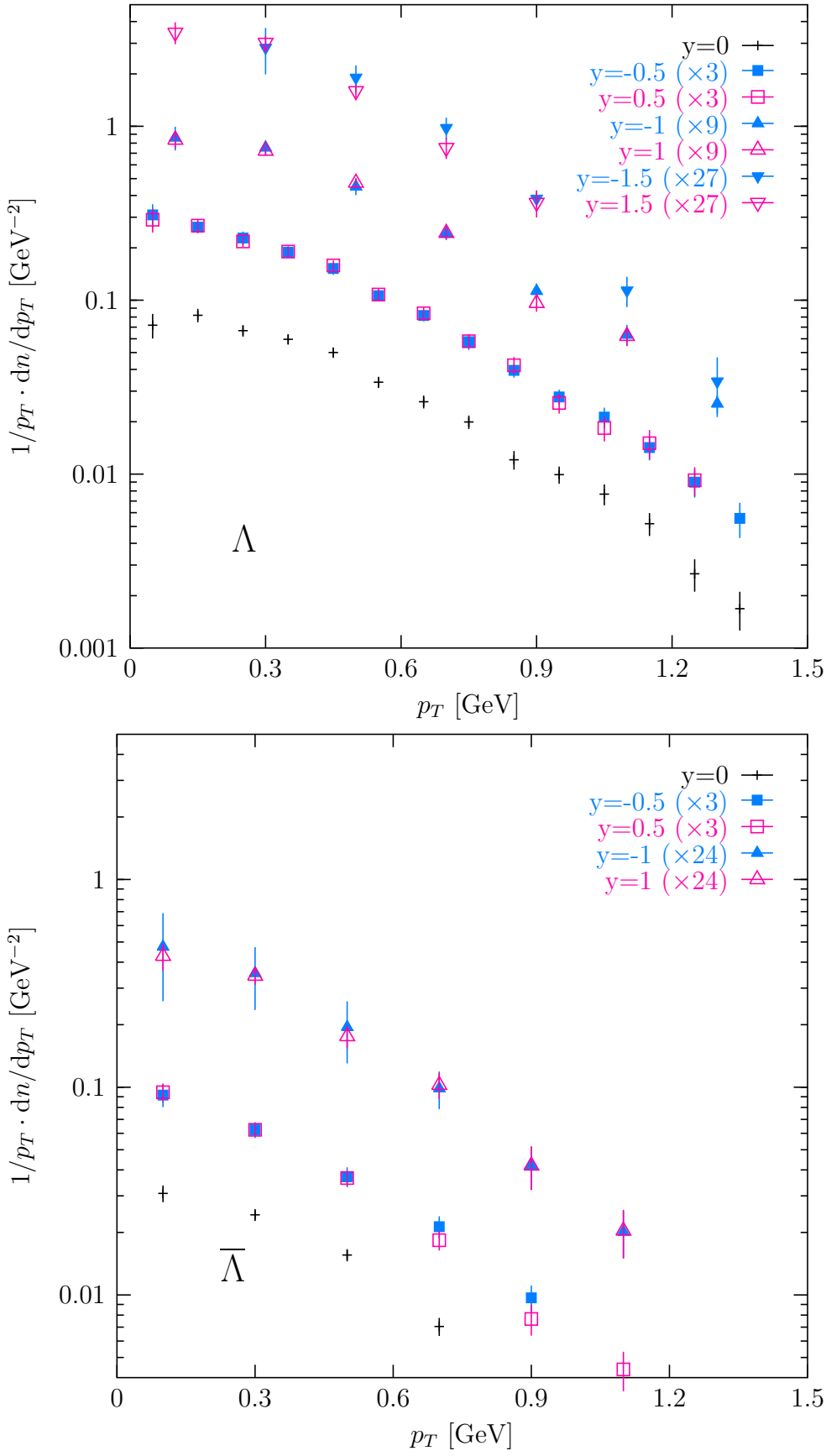

Figure 7.1: p_T spectra of Λs and $\overline{\Lambda}$s at different rapidities

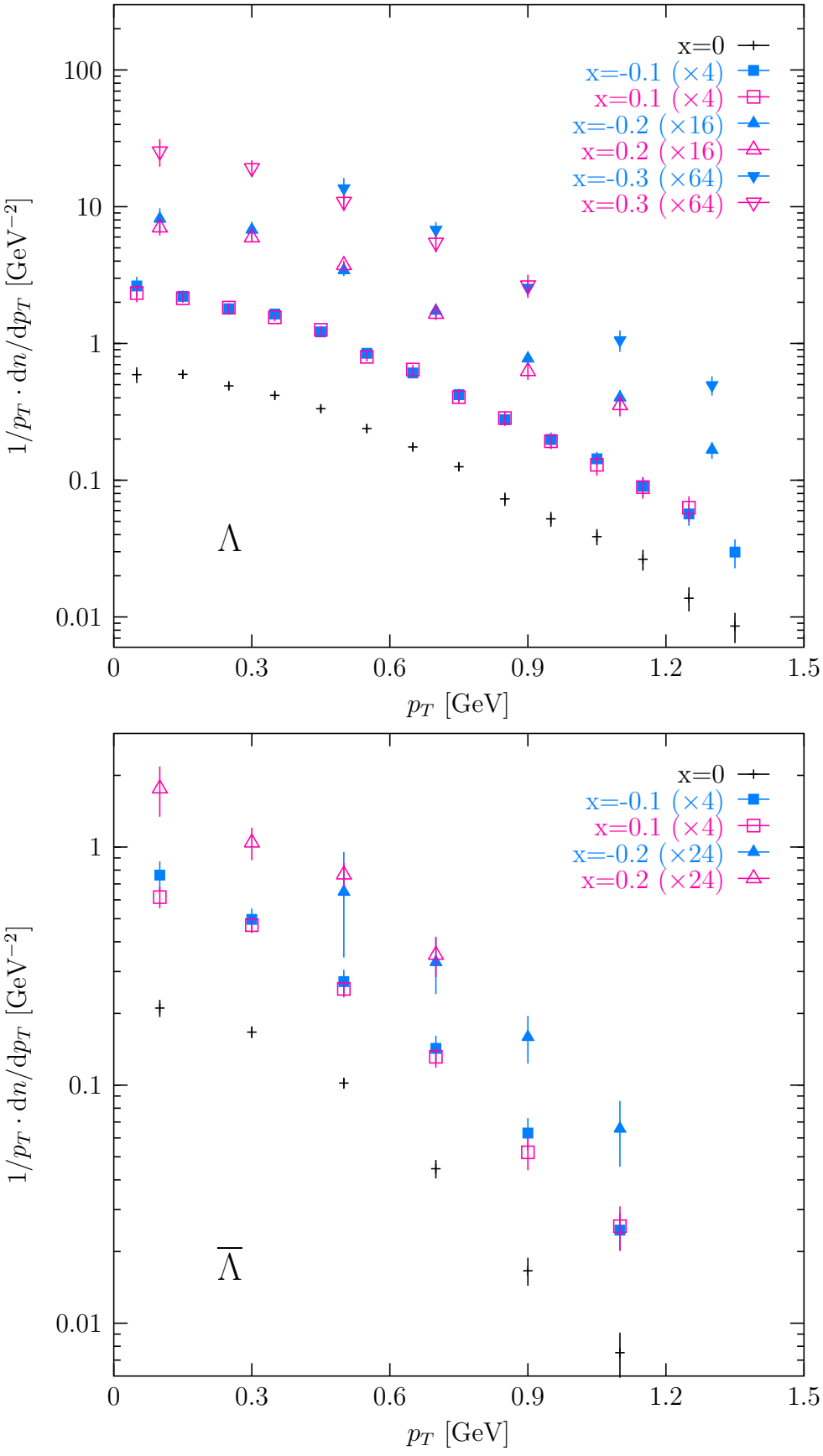

Figure 7.2: p_T spectra of Λs and $\overline{\Lambda}$s at different Feynman-x values

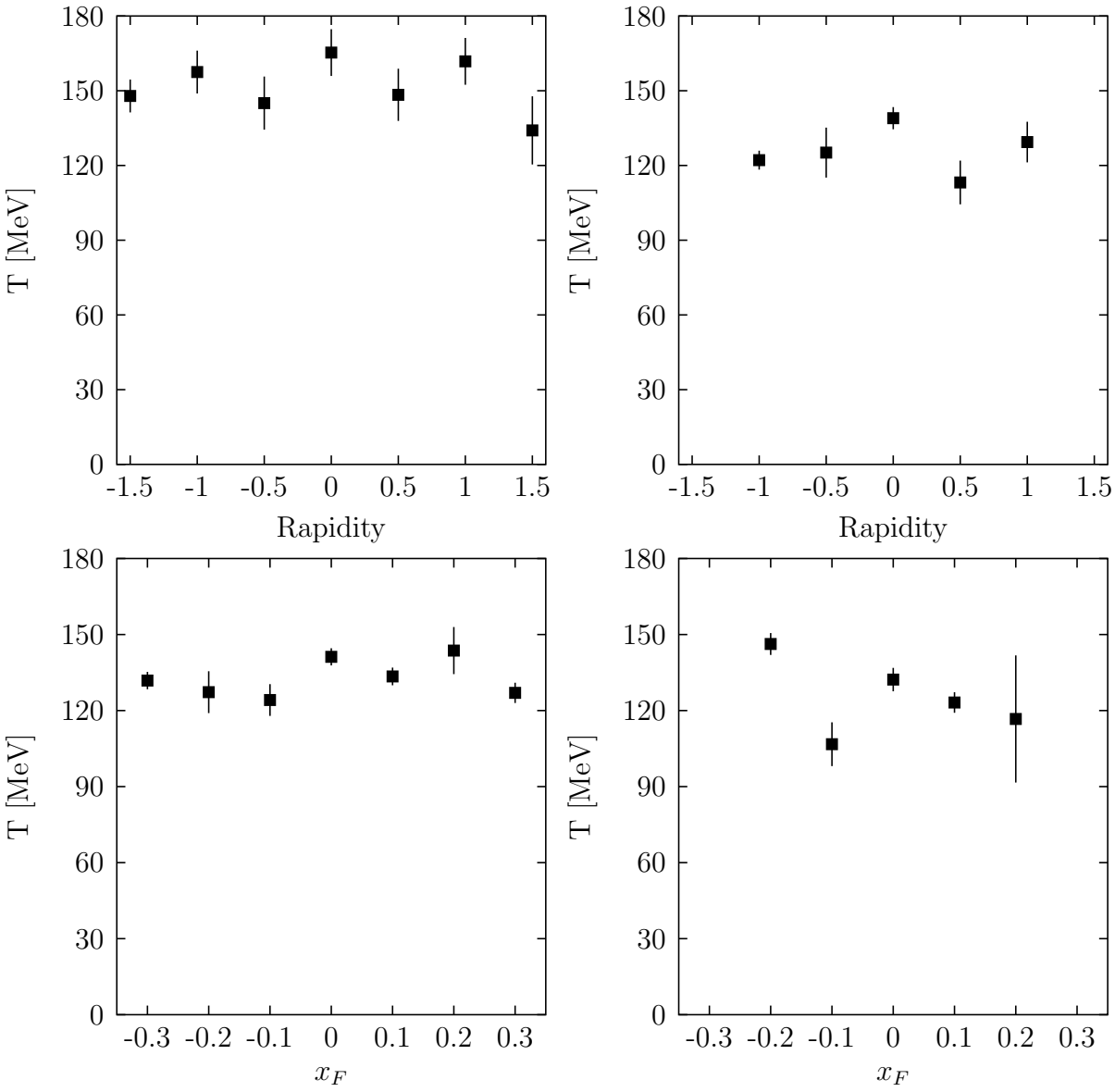

Figure 7.3: The inverse slope parameter (T) of the transverse momentum spectra (resulting from a fit of the function (6.1) to the measured points) as a function of rapidity (above) and Feynman-x (below)

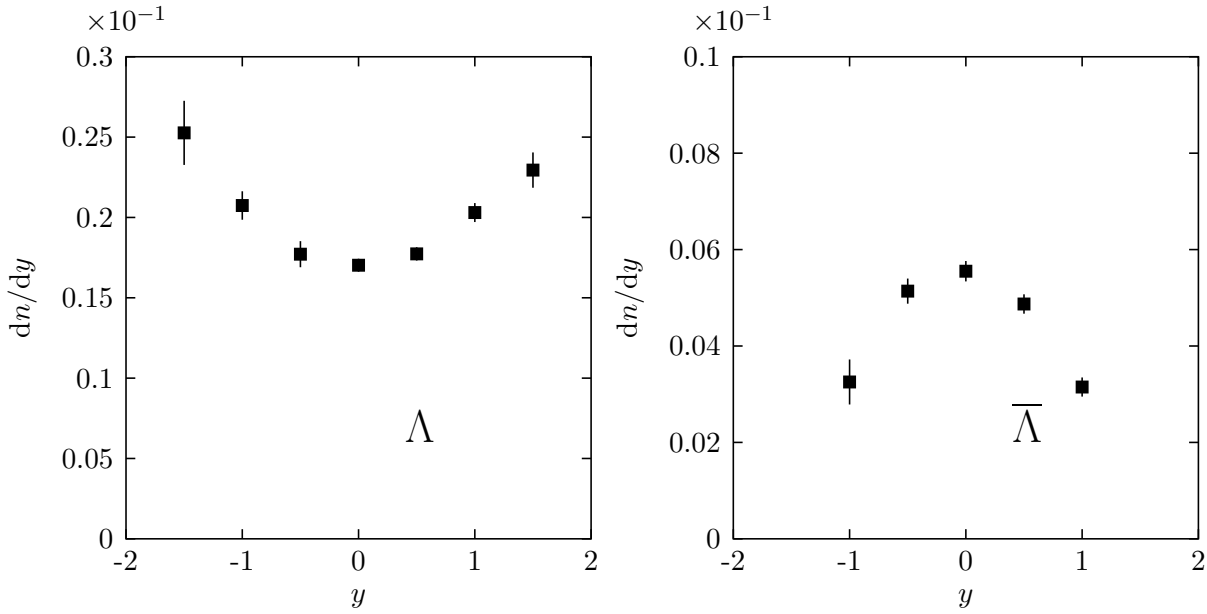

Figure 7.4: Rapidity distribution of Λs and $\overline{\Lambda}$s

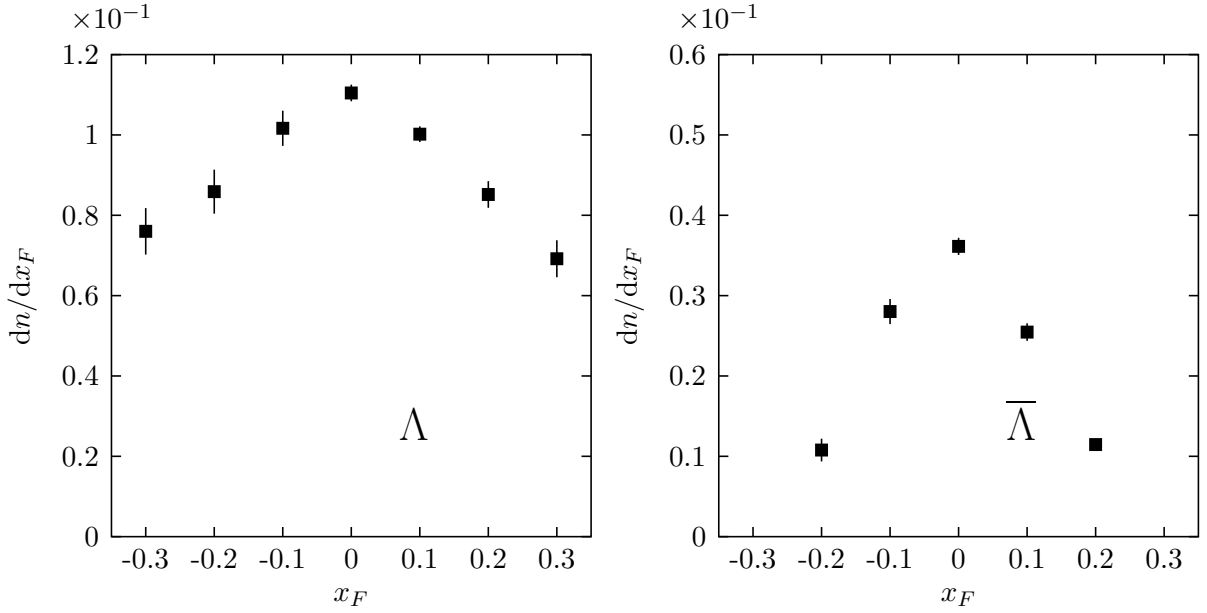

Figure 7.5: Feynman-x distribution of Λs and $\overline{\Lambda}$s

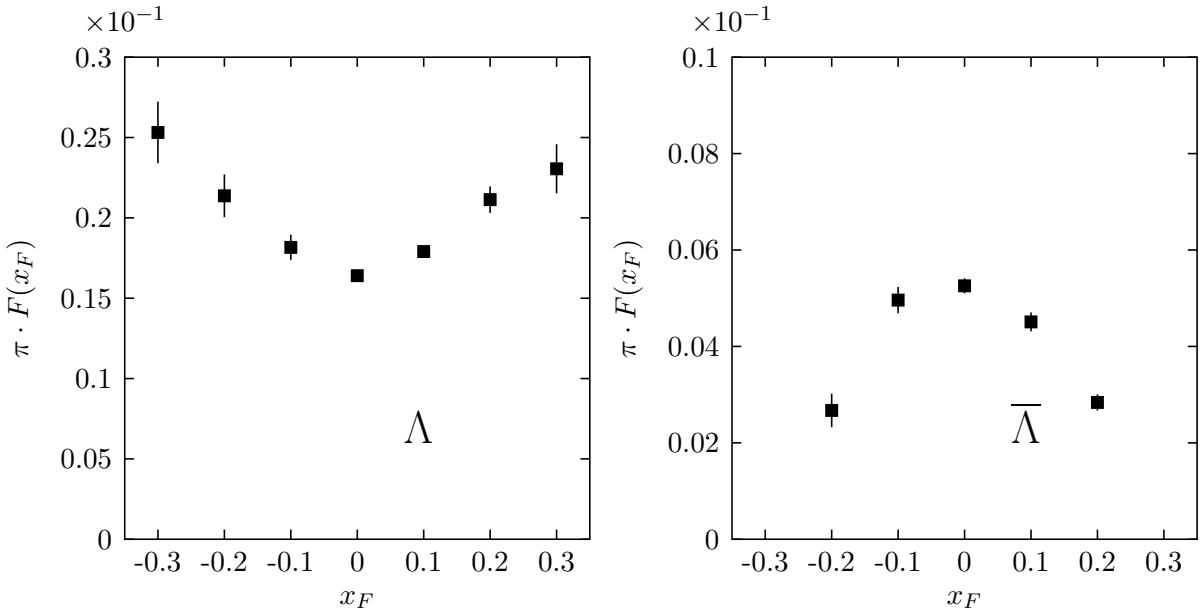

Figure 7.6: Invariant Feynman-x distribution of Λs and $\overline{\Lambda}$s

7.1.2 Ξ^- and $\overline{\Xi}^+$ Results

The transverse momentum distributions of Ξ^- and $\overline{\Xi}^+$ in the rapidity range [-0.75;0.75] are shown in figure 7.7. The longitudinal distributions are shown in figures 7.8 and 7.9.

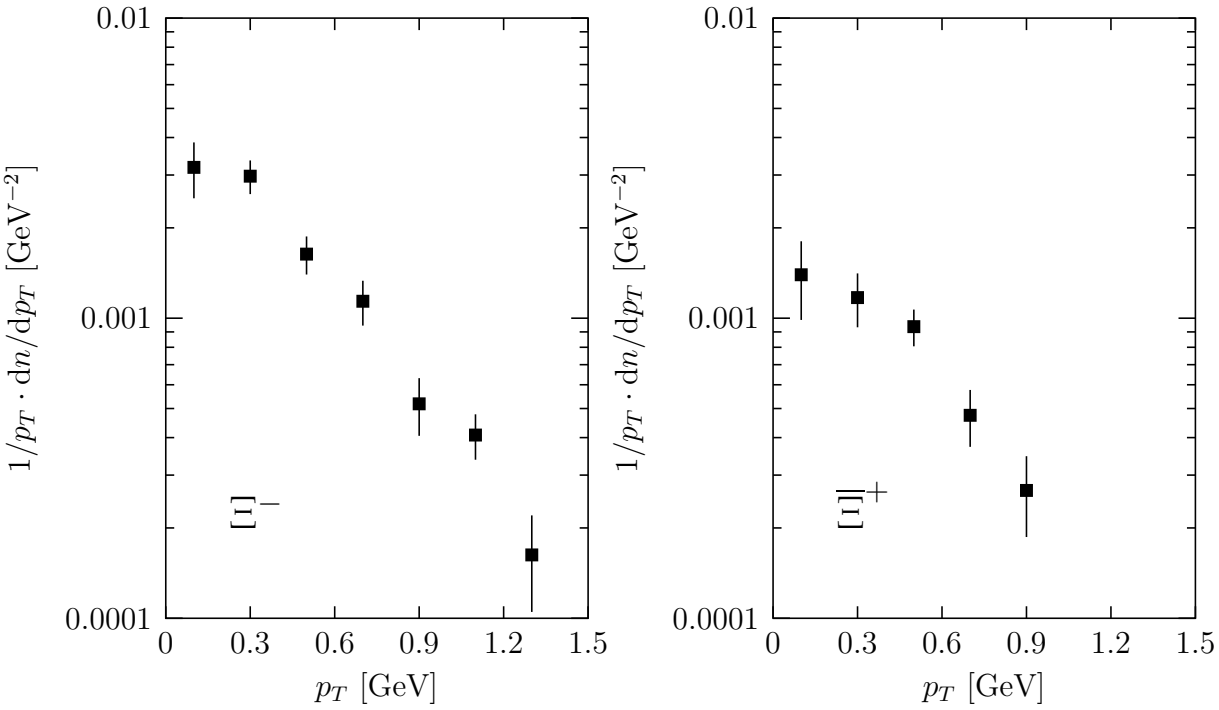

Figure 7.7: Transverse momentum distributions of Ξ^- and $\overline{\Xi}^+$ in the rapidity range [-0.75;0.75].

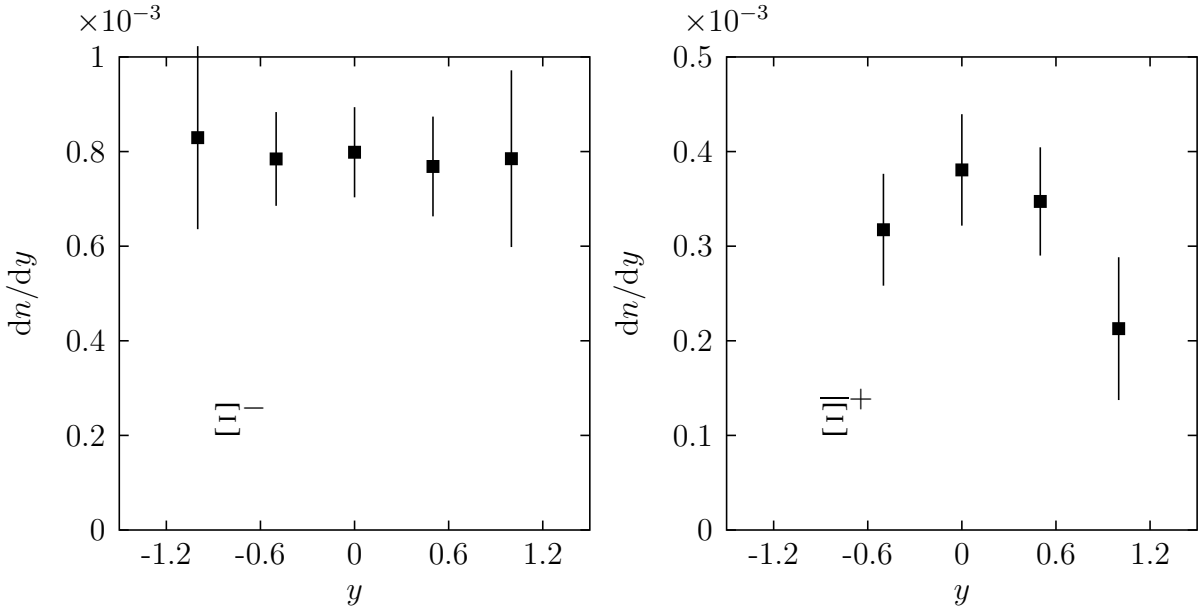

Figure 7.8: Rapidity distributions of Ξ^- and $\overline{\Xi}^+$.

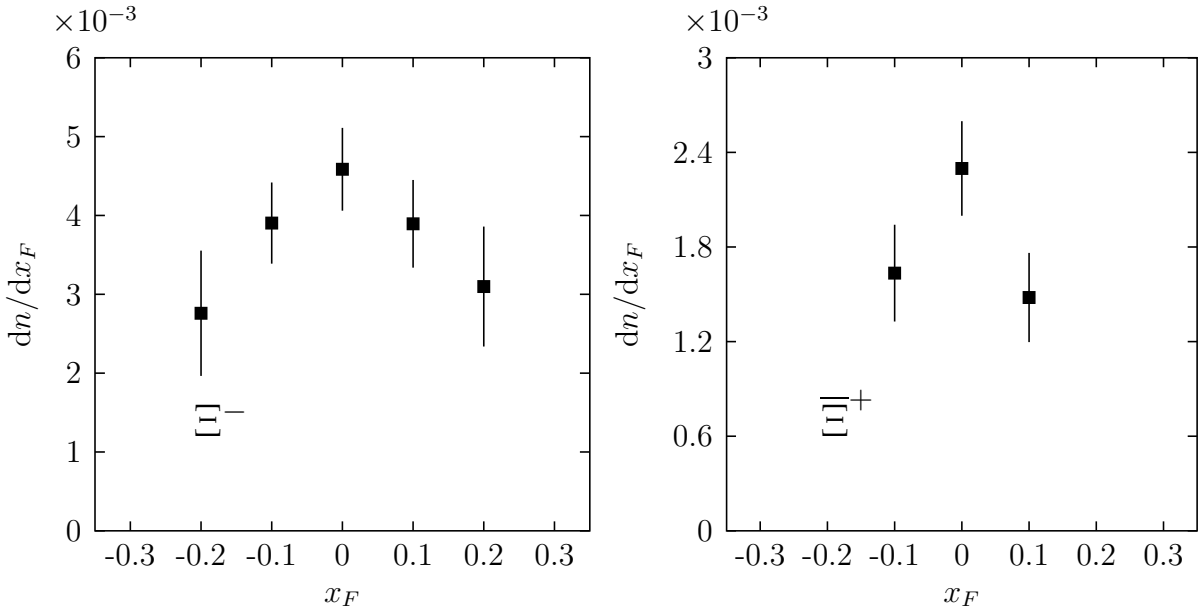

Figure 7.9: Feynman-x distributions of Ξ^- and $\overline{\Xi}^+$.

7.2 Comparison to Other Measurements

Λ and $\overline{\Lambda}$ production in proton-proton collisions has been measured by several experiments. Most results are obtained by bubble-chamber experiments [26]– [48]. Other results are measured by the EHS [49]– [52] and ISR experiments [53]– [57]. Most of these experiments measured Λ and $\overline{\Lambda}$ production in only one (the backward) hemisphere of the proton-proton center-of-mass system, therefore checking the symmetry of the distributions was not possible. In the framework of this thesis the majority of the existing results have been collected and put into a database.[1] The presented summary plots are the results of this work.

The rapidity distributions of Λ and $\overline{\Lambda}$ measured by these experiments are summarized in figures 7.10 and 7.11. NA49 results are also shown in red. Since there is no scaling in the rapidity spectra with collision energy, only results in a limited energy range are shown. Earlier measurements have large errorbars, and are widely spread. All results on the Λ rapidity distribution show a peak in the backward region, which is associated with the leading particle effect. NA49 results are fully compatible with these measurements, and have significantly smaller errors.

There are less numerous measurements on the antilambda rapidity distribution. NA49 results are between the results at lower and higher energies (reflecting the increase of the antilambda yield with increasing collision energy), and provide a great improvement in the data quality with their small errorbars.

Feynman-x and invariant Feynman-x (see Appendix B) distributions are summarized in figures 7.12, 7.13, 7.14 and 7.15. There exist only a few measurements of the Λ Feynman-x distribution, with large errorbars. This is even more true for the antilambda. NA49 results are again very important to improve the quality of the existing data. Much more experiments have measured the invariant Feynman-x distributions of the lambda and antilambda. NA49 results nicely agree with the world average for Λ. The $\overline{\Lambda}$ results are also compatible with the poor quality world data.

[1] The results were taken from the Durham database (http://www-spires.dur.ac.uk/HEPDATA/) when they were available there. Otherwise the articles were scanned, and the values were read from the published plots, using a privately modified version of the software `gv`.

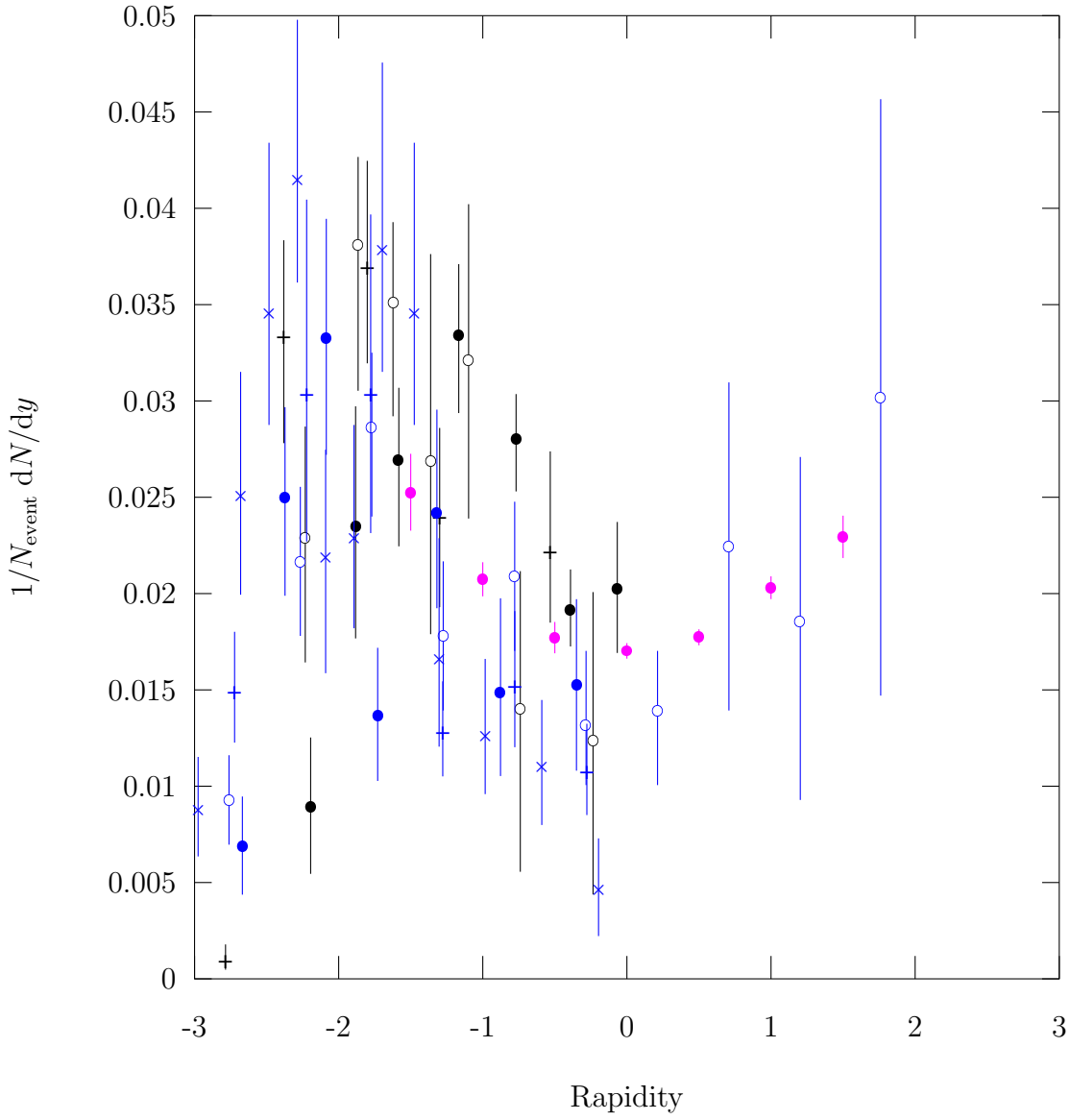

Figure 7.10: Summary of Λ rapidity distributions in proton-proton collisions. The different colors indicate different energy ranges: black = 10–18 GeV, blue: >18 GeV. NA49 results are shown in red

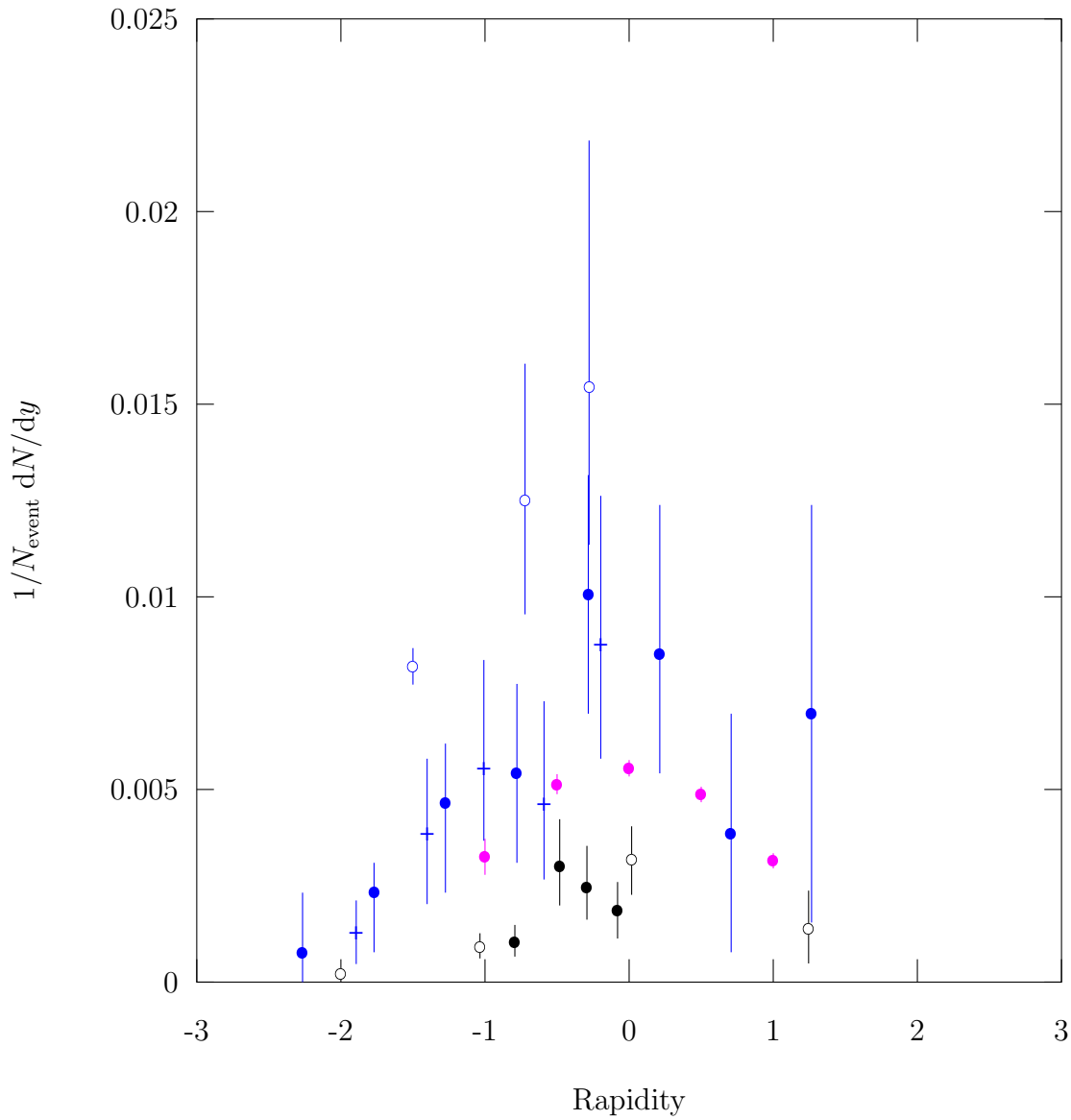

Figure 7.11: Summary of $\overline{\Lambda}$ rapidity distributions in proton-proton collisions. The different colors indicate different energy ranges: black = 10–18 GeV, blue: >18 GeV. NA49 results are shown in red

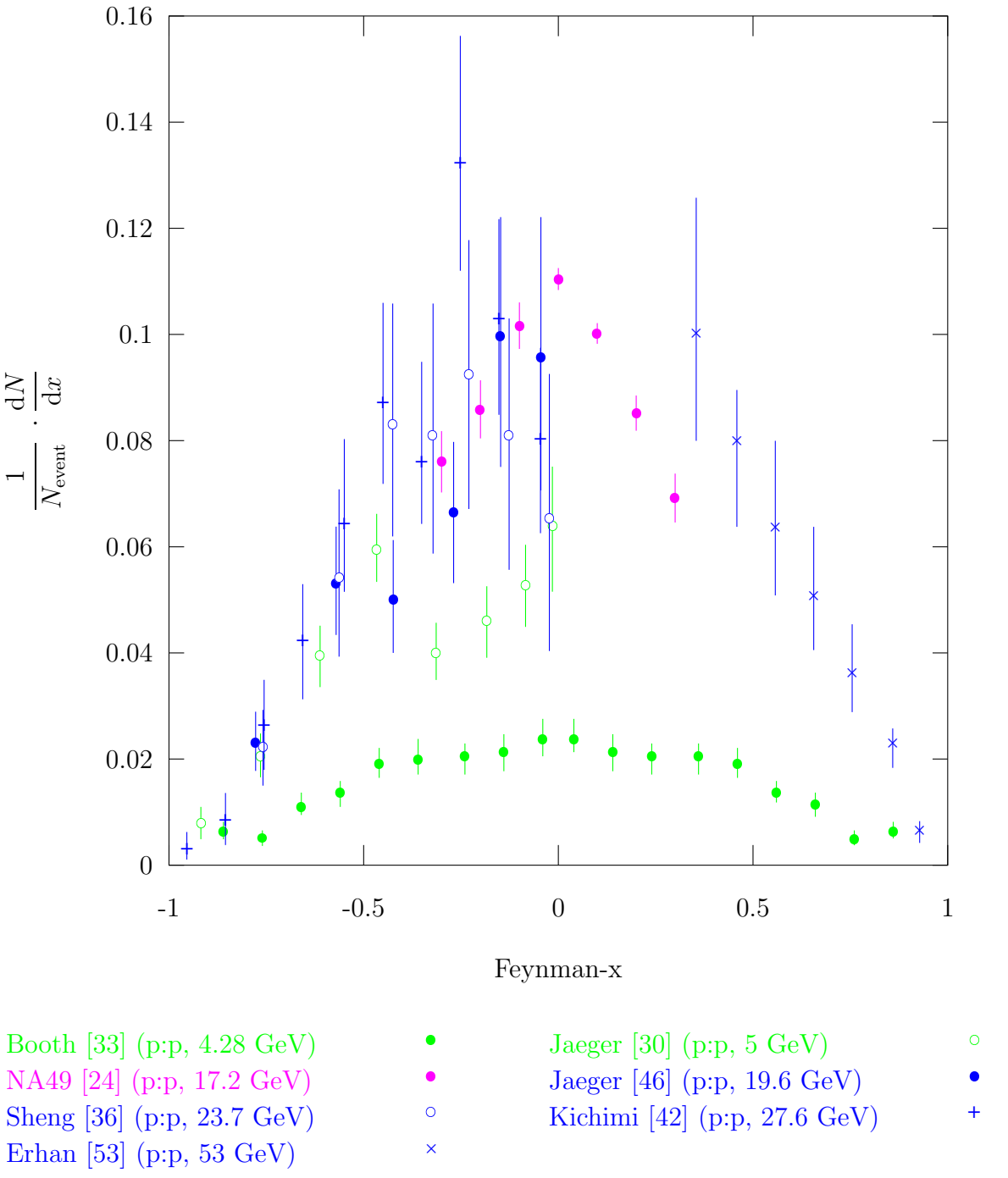

Figure 7.12: Summary of Λ Feynman-x distributions in proton-proton collisions. The different colors indicate different energy ranges: green = 0–10 GeV, black = 10–18 GeV, blue: >18 GeV. NA49 results are shown in red

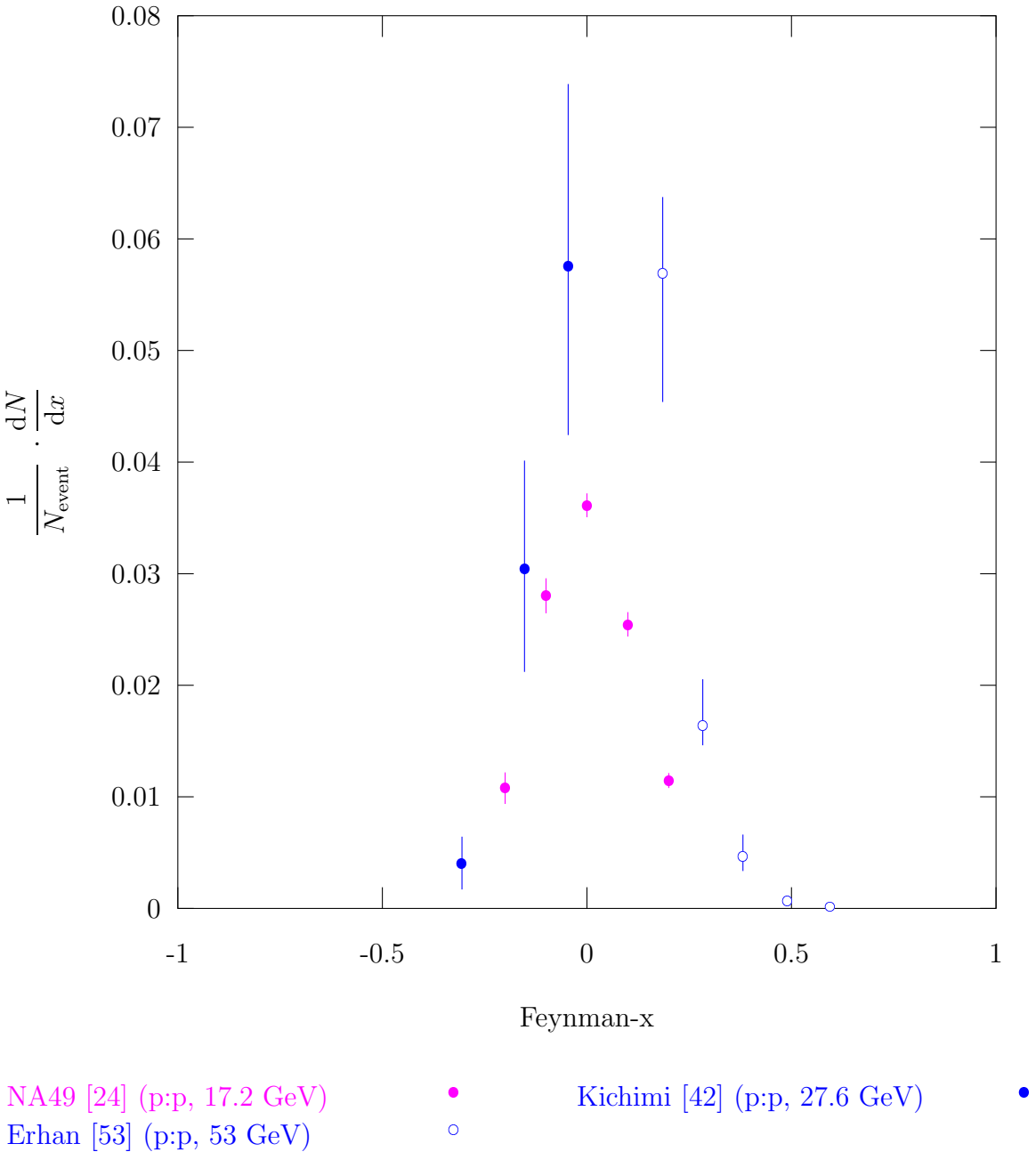

Figure 7.13: Summary of $\overline{\Lambda}$ Feynman-x distributions in proton-proton collisions. The different colors indicate different energy ranges: green = 0–10 GeV, black = 10–18 GeV, blue: >18 GeV. NA49 results are shown in red

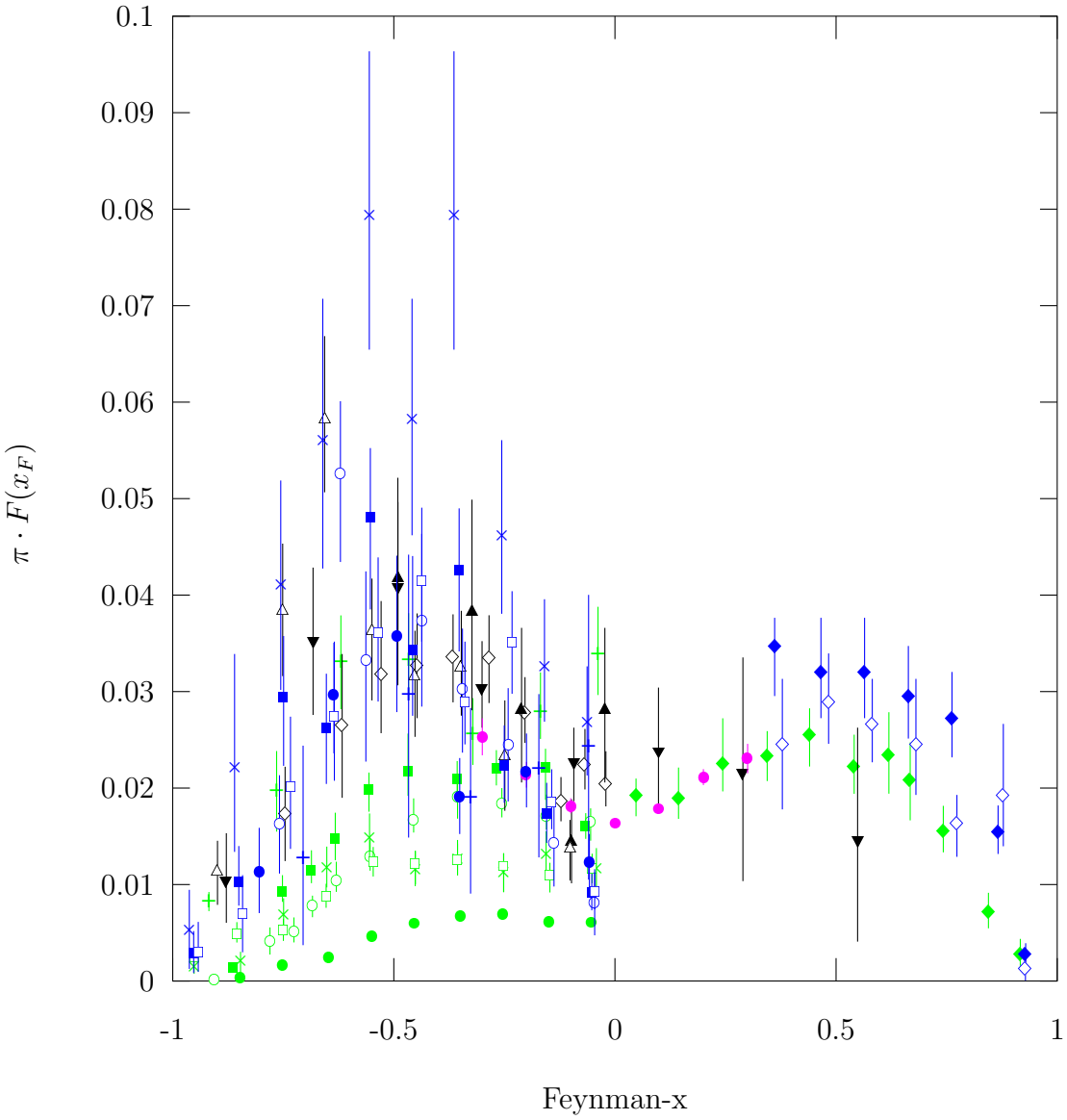

Oh [34] (p:p, 3.8 GeV - corrected for $\Sigma^{\pm}$)
Jaeger [30] (p:p, 5 GeV)
Blobel [28] (p:p, 6.84 GeV)
Bogolyubsky [72] (p:p, 7.86 GeV - russian)
Blumenfeld [44] (p:p, 11.45 GeV)
Brick [31] (p:p, 16.6 GeV)
Jaeger [46] (p:p, 19.6 GeV)
Dao [38] (p:p, 23.9 GeV)
Asai [52] (p:p, 26 GeV)
Erhan [53] (p:p, 53 GeV)
Blobel [28] (p:p, 4.93 GeV)
Oh [34] (p:p, 5.6 GeV - averaged from 5.1,6 GeV)
Oh [34] (p:p, 6.9 GeV - averaged from 6.4,6.8,7.4 GeV)
Ammosov [26] (p:p, 11.4 GeV)
Chapman [35] (p:p, 13.9 GeV)
NA49 [24] (p:p, 17.2 GeV)
Sheng [36] (p:p, 23.7 GeV)
Bailly [49] (p:p, 26 GeV)
Kichimi [42] (p:p, 27.6 GeV)
Erhan [53] (p:p, 62 GeV)

Figure 7.14: Summary of Λ invariant Feynman-x distributions in proton-proton collisions. The different colors indicate different energy ranges: green = 0–10 GeV, black = 10–18 GeV, blue: >18 GeV. NA49 results are shown in red

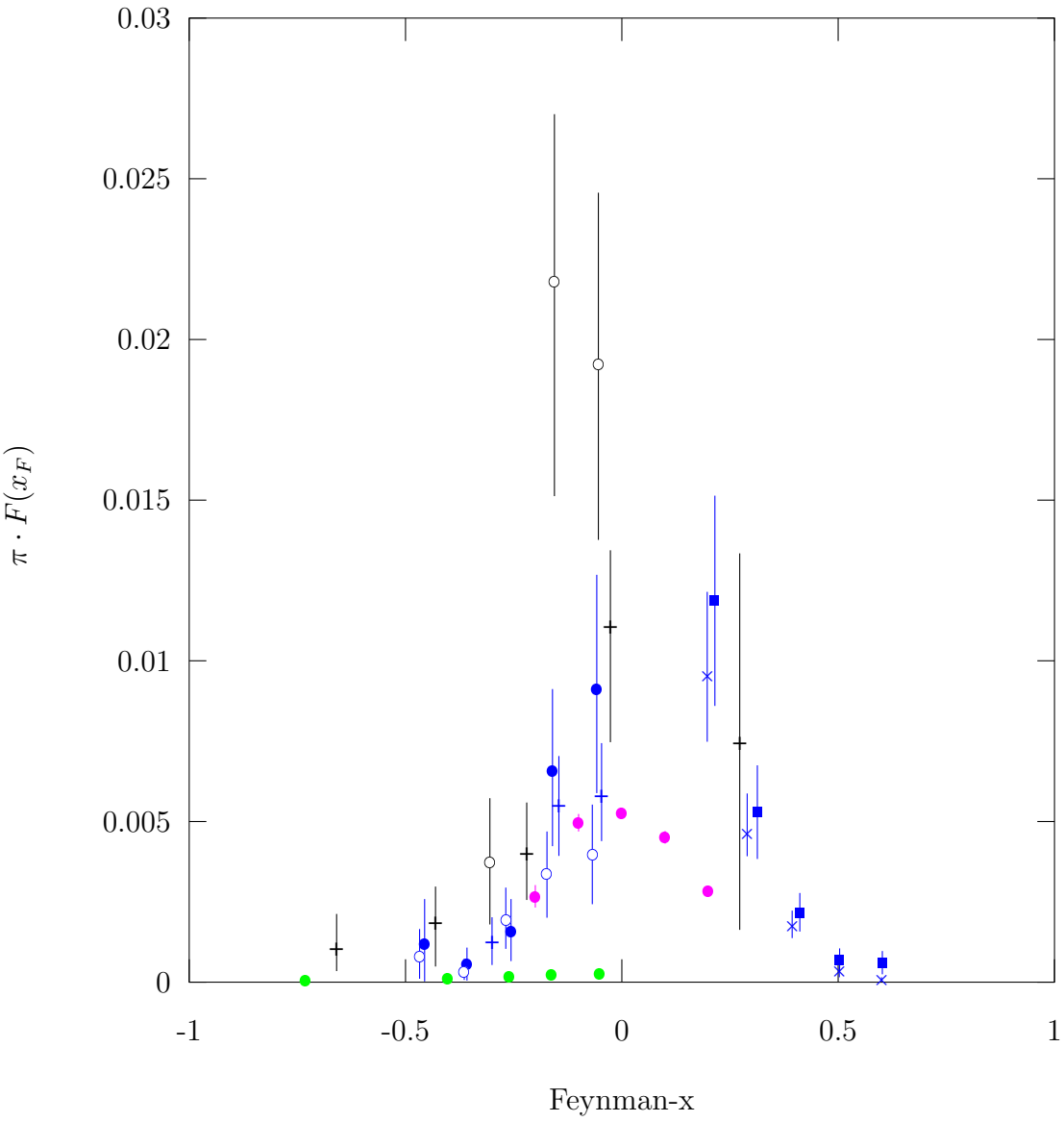

Figure 7.15: Summary of $\overline{\Lambda}$ invariant Feynman-x distributions in proton-proton collisions. The different colors indicate different energy ranges: green = 0–10 GeV, black = 10–18 GeV, blue: >18 GeV. NA49 results are shown in red

The results presented in this thesis are the first measurements of Ξ^- and $\overline{\Xi}^+$ spectra in proton-proton collisions. Ξ^- production in proton-proton collisions was measured only by one other experiment at the CERN ISR [53]. That experiment had acceptance only in one hemisphere in the region $0.4 < x_F$. The inclusive cross section of Ξ^- in this region was found to be (9±3) μb. NA49 results are obtained in the region -0.25< x_F <0.25. In order to compare these two measurements, the Ξ^- Feynman-x distribution predicted by `VENUS` was normalized to the measured results in this x_F range (see fig. 7.16). Integrating this distribution over the range $0.4 < x_F$ we obtained the inclusive cross section of 5.1 μb, which – under the circumstances – is in good agreement with the results presented by [53, Erhan].

Ξ^- and $\overline{\Xi}^+$ production has been measured also by the *hyperon beam experiment* [58] at the CERN SPS. In this experiment the hyperons were produced by 200 GeV protons incident on a BeO target, and the hyperons were detected in the range 0.35< x_F <0.66. Due to the differences of the reaction types and the studied momentum regions these results can not easily be compared.

Ξ^- production has also been observed in $\overline{p}p$ collisions at high center-of-mass energies ($\sqrt{s}$ = 540 GeV) [65].

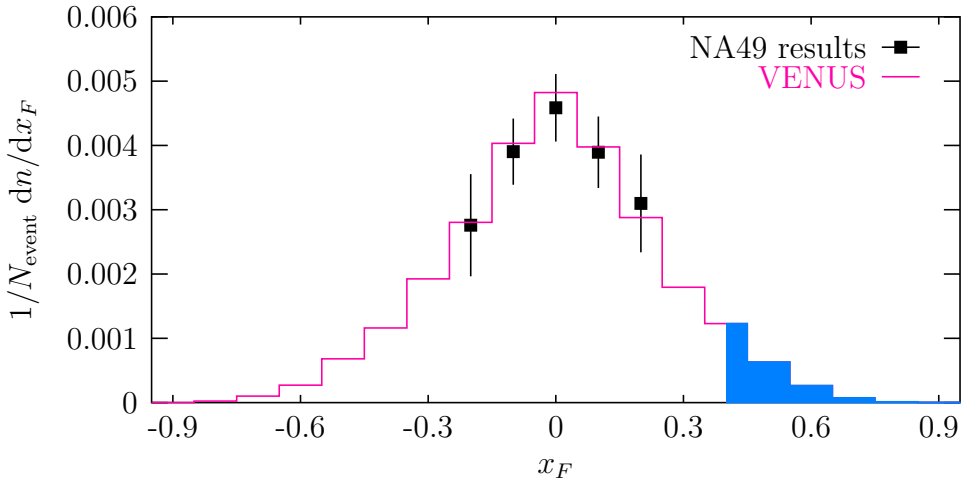

Figure 7.16: The measured and the (normalized) `VENUS`-predicted x_F distribution of Ξ^-. The filled region represents the range measured by [53].

7.3 Ω Yields

7.3.1 Experimental Results

The number of observed Ωs in the rapidity range $-0.7 < y < 0.7$ (the surface of the peak above the background, see figure 6.13) is roughly 50. In order to estimate the detection efficiency, 3500 VENUS-generated Ω^--events were simulated. The correction factor for Ωs in the above mentioned momentum range was obtained from the simulation to be $2.78/BR$, where the factor 2.78 includes the acceptance, reconstruction efficiency and the effect of the applied cuts, and $BR = 0.678 \cdot 0.639$ is the branching ratio into the charged channel of the 3-particle final state. Since the rapidity range $-0.7 < y < 0.7$ could not be divided into smaller bins, the overall correction factor derived from the simulation, and therefore the estimated Ω yield depends on the momentum distribution of the simulated particles. The Ω^- yield per inelastic event and per unit of rapidity is estimated to be

$$\frac{N^{\Omega^-}}{N_{\mathrm{ev}}} = (8.5 \pm 1.3) \cdot 10^{-5}$$

No measurements exist on the production of the Ω particle in p-p collisions. The closest reaction type is the proton-beryllium data of the WA97 experiment [68], where the total yield of $\Omega^- + \overline{\Omega}^+$ was measured to be $16 \pm 6 \cdot 10^{-5}$ per inelastic event. These two results can not be directly compared: in p-Be collisions more nucleons participate in the collision, therefore the particle yields are higher. A simple minded way to scale the p-Be results to the p-p results is to scale the yields by the ratio of the number of participants (this concept, and the way it is measured will be discussed in a later session, 7.7; for the moment we refer to the intuition of the reader). The average number of participants in p-Be collisions is estimated to be 2.5, the number of participants in p-p collisions is 2, the scaling factor is 2/2.5:

Exp.	Reaction	N_{part}	Statistics	Yield	Yield in p-p
WA97	p-Be	2.5	33 $(\Omega^- + \overline{\Omega}^+)$	$16 \cdot 10^{-5}$	$12.8 \cdot 10^{-5}$
NA49	p-p	2	50 Ω^-		$(8.5 \pm 1.3) \cdot 10^{-5}$

Though the scaled yield of the WA97 experiment is higher than the NA49 results,[2] the relatively good agreement – regarding the large uncertainties in the way of comparison – confirms the NA49 results, which are the first measurement of the Ω^- production cross section in p-p collisions.

[2] An *enhancement* of the Λ and Ξ^- yield between p-p and scaled p-Be collisions is observed as well, see section 7.7.

Since no clear signal is seen in the $\overline{\Omega}^+$ mass spectrum, one can only estimate an upper limit on the $\overline{\Omega}^+$ production cross section, or on the $\overline{\Omega}^+/\Omega^-$ ratio. Presenting the latter one has the benefit of avoiding the usage of correction factors, and therefore several possible systematic errors.

The estimation of the $\overline{\Omega}^+/\Omega^-$ ratio can be done using standard confidence interval calculation methods. The small statistics of even the Ω^-s (50 candidates), however, makes the situation a bit more complicated: it is not enough to estimate a confidence interval on the expectation value of the number of $\overline{\Omega}^+$s; the $\overline{\Omega}^+/\Omega^-$ ratio depends also on the number of Ω^-s, which we don't know exactly: it has a variance of $\sqrt{50}$. Fortunately this problem is quite simple, since the two unknown quantities (number of $\overline{\Omega}^+$s and Ω^-s, or equivalently, the number of Ω^-s and the $\overline{\Omega}^+/\Omega^-$ ratio) are uncorrelated.

The $\overline{\Omega}^+$ invariant mass spectrum was fitted with a first order polynomial. The background in the mass range [1.668; 1.677] GeV (3 bins) is calculated as the area below this polynomial, which is 70. The total number of entries in these 3 bins is 78. Using standard confidence interval calculation methods (see for example [89]), an upper limit estimation for the number of $\overline{\Omega}^+$s is derived with 95% confidence level, which – depending on the number of omegas – gives an upper limit for the $\overline{\Omega}^+/\Omega^-$ ratio. Figure 7.17 shows this upper limit estimation as the function of the number of Ωs (N^{Ω^-}). The indicated range of N^{Ω^-} was chosen to be a symmetric, 95% confidence interval around the observed value (50). The curve has a value of 0.5 at the observed number of omegas ($N^{\Omega^-} = 50$). In the following paragraphs this value will be quoted.

7.3.2 Comparison to Model Predictions

While absolute particle yields in physics models often depend on the parameters of the model, the predicted particle ratios can be a more characteristic property of the model. In [82] the predictions of different string-model implementations (UrQMD, PYTHIA and NEXUS) and a statistical model [83] for the $\overline{B}/B$ ratio are presented and compared to preliminary NA49 results (see figure 7.18; $\overline{B}$ denotes an antibaryon, B denotes a baryon).

Both the string models and the statistical models agree in predicting an increasing $\overline{B}/B$ ratio with increasing strangeness, which is also observed in the data. The string models, however, predict the $\overline{\Xi}^+/\Xi^-$ ratio to be close to 1, and the $\overline{\Omega}^+/\Omega^-$ ratio to be substantially larger than unity. The prediction of the statistical model (right panel

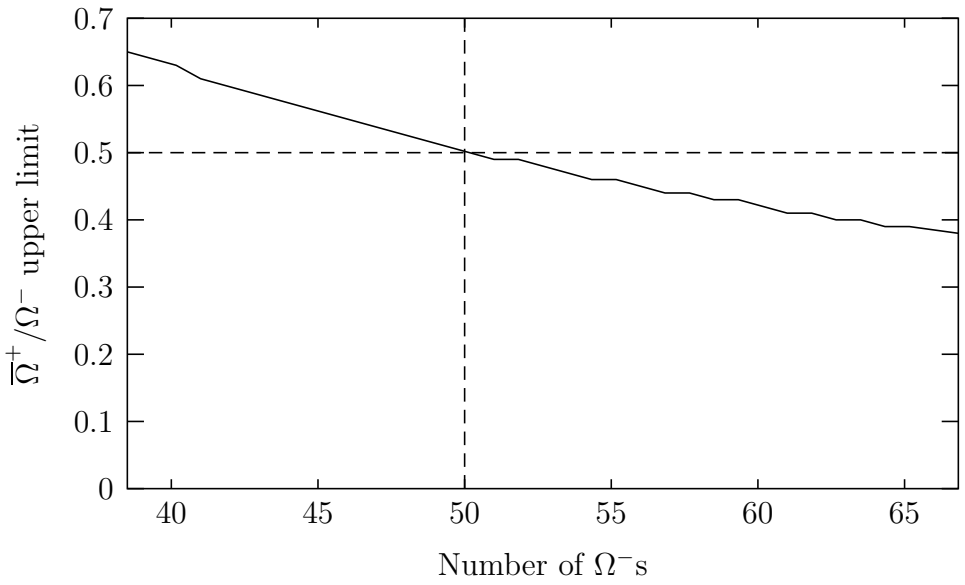

Figure 7.17: Upper limit estimation for the $\overline{\Omega}^+/\Omega^-$ ratio with 95% confidence level, depending on the true number of omegas

of figure 7.18) was done for the full phase space, while the measurements of the $\overline{B}/B$ ratio have been performed at midrapidity, where this ratio is expected to be the largest. Therefore a precise agreement between these predictions and the measured points is not to be expected. However, they agree in the key result $\overline{B}/B < 1$ (which would not change by measuring the $\overline{B}/B$ ratio in the full phase space). Note that the upper limit estimation for the $\overline{\Omega}^+/\Omega^-$ was calculated for the rapidity range -0.7$< y <$0.7, where it is expected to be smaller than at midrapidity.

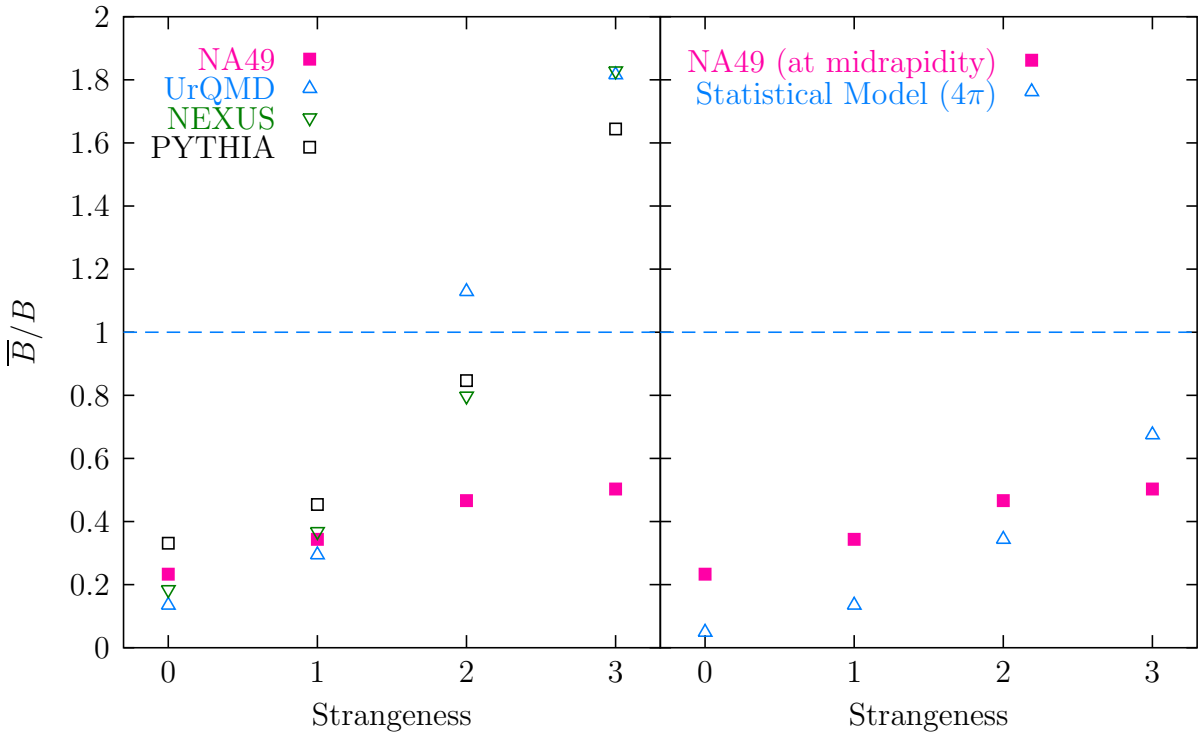

Figure 7.18: Left: antibaryon to baryon ratio at midrapidity in p-p collisions at p_{beam} = 160 GeV, as a function of strangeness, predicted by string models. Left: the same ratio predicted by a statistical model (for the full phase space)

7.4 Energy-dependence of midrapidity yields

In the previous section longitudinal distributions of Λ and $\overline{\Lambda}$ at different energies were compared. In this section we shall explore the central region around y=0. Figure 7.19 shows the Λ and $\overline{\Lambda}$ midrapidity yields as the function of collision energy. (For those experiments, which didn't show rapidity spectra, the invariant Feynman-x distribution was used at $x_F = 0$, since at this point the two are equal up to a factor π, see Appendix B). For Λ production the energetically most favored reaction is $pp \rightarrow p\Lambda K$, which has a threshold energy $\sqrt{s} \geq 2.55$ GeV. Above this collision energy the Λ midrapidity yield has a plateau, which is followed by a slight decrease. The $\overline{\Lambda}$ production has a much higher threshold: due to baryon number conservation not only the strangeness has to be compensated, but a new baryon has to be created as well. The energetically most favored reaction is $pp \rightarrow pp\Lambda\overline{\Lambda}$ with a threshold energy $\sqrt{s} \geq 4.106$ GeV. The $\overline{\Lambda}$ midrapidity yield is steeply rising in the region of the Λ plateau, and they reach the same magnitude at around $\sqrt{s}$ ≈30-40 GeV. The experimental results from p-p collisions around this energy range are compatible with identical Λ and $\overline{\Lambda}$ yields at midrapidity,

and predict a common increase of them at higher energies. Measurements of Λ and $\overline{\Lambda}$ yields at higher energies ($\sqrt{s} > 200$ GeV) exist only in $\overline{p}p$ collisions [63], where Λ and $\overline{\Lambda}$ yields are equal. These results are also shown in figure 7.19.[3] Although the equality of Λ and $\overline{\Lambda}$ midrapidity yields in $\overline{p}p$ collisions is no surprise, these results follow the assumed trend of the same Λ and $\overline{\Lambda}$ midrapidity yields in p-p collisions. These results can be explained with the following picture [85]:

The Λ baryon has 2 common quarks with the projectile (or target) proton. This causes the leading particle effect (see the peaked rapidity distribution of Λ, fig. 7.10). At low energies a small momentum transfer is sufficient to "pull back" the 2 valence quarks of the projectile in rapidity space (*baryon stopping*), resulting in a Λ particle at midrapidity (*direct production*). No $\overline{\Lambda}$s can be produced by this mechanism, since $\overline{\Lambda}$s consist of antiquarks not present in the proton. At higher and higher energies larger momentum transfers are needed to produce Λs at midrapidity from the valence quarks of the projectile; these processes are less probable, which can be the reason of the decrease of the Λ midrapidity yield above 20 GeV. However, at the same time the $\overline{\Lambda}$ yield increases steeply, indicating that another mechanism – baryon pair production – is getting more dominant, where all quarks of the baryons are newly created (in pairs). At high energies, where the *direct production* of Λs at midrapidity is negligible, baryon pair production might be the dominant mechanism responsible for both Λ and $\overline{\Lambda}$ production, resulting in an equal Λ and $\overline{\Lambda}$ midrapidity-yield. The central region becomes baryon free, by which we mean that the net baryon yield (baryons minus antibaryons) approaches zero.

At the SPS energy ($\sqrt{s} = 17.2$ GeV) there is a considerable $\overline{\Lambda}$ production, but we have not reached yet the energy range, where the central region is baryon free. A significant fraction of Λs is produced via pair-production (about $^1/_3$ of the Λs, if we estimate this fraction with the $\overline{\Lambda}$ yield), but the dominant production mechanism is still baryon stopping. If the observed Λs could be classified into these two groups, one could study these two production mechanisms. I will present the first attempts into this direction in the following sections.

[3]The UA5 detector had no magnetic field for the measurement of particle momenta. V^0s were analyzed using hypotheses about the V^0 identity. This analysis made the distinction between Λ and $\overline{\Lambda}$ impossible, and the reported yields are therefore the sum of Λs and $\overline{\Lambda}$s ($\Lambda + \overline{\Lambda}$).

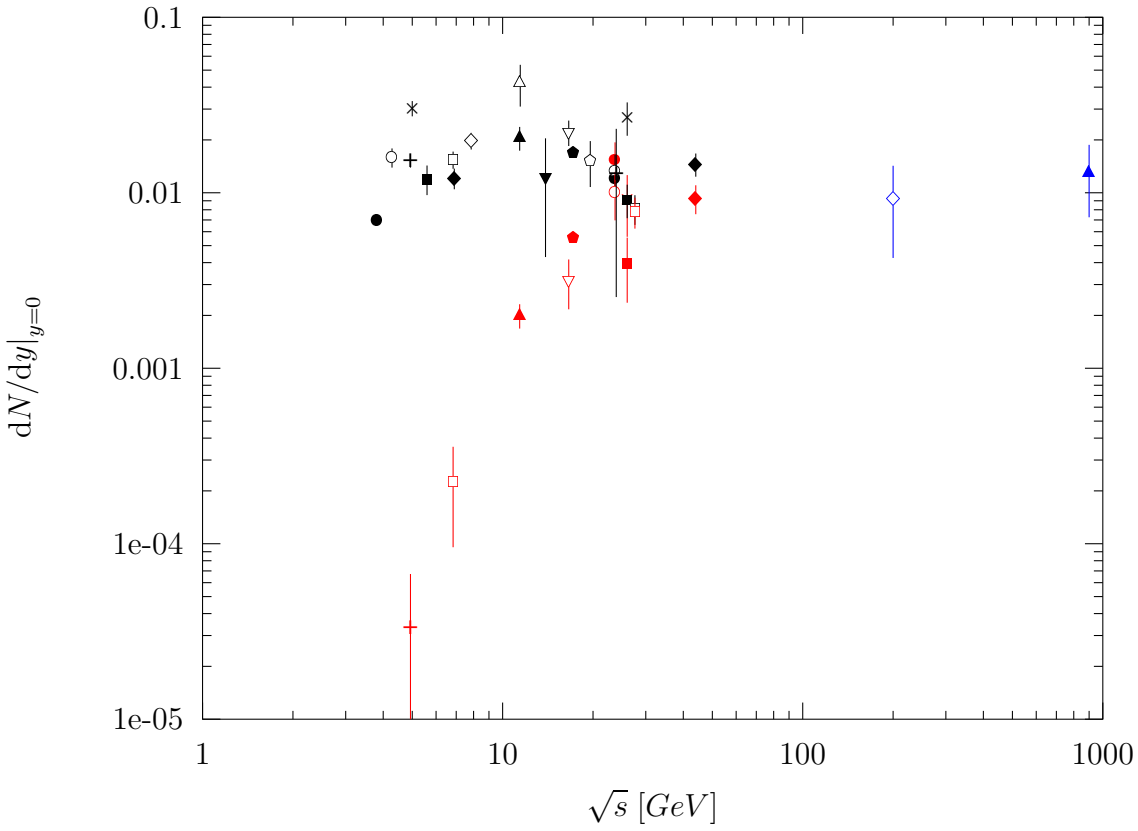

Oh [34] (p:p, 3.8 GeV - corrected for $\Sigma^{\pm}$) ●
Blobel [28] (p:p, 4.93 GeV) +
Oh [34] (p:p, 5.6 GeV - averaged from 5.1,6 GeV) ■
Oh [34] (p:p, 6.9 GeV - averaged from 6.4,6.8,7.4 GeV) ◆
Ammosov [26] (p:p, 11.4 GeV) ▲
Chapman [35] (p:p, 13.9 GeV) ▼
NA49 [24] (p:p, 17.2 GeV) ⬟
Sheng [36] (p:p, 23.7 GeV) ●
Dao [38] (p:p, 23.9 GeV) +
Asai [52] (p:p, 26 GeV) ■
F.W. B"usser [54] (p:p, 44 GeV) ◆
Ansorge [63] (pbar:p, 900 GeV - $(\Lambda + \overline{\Lambda})/2$) ▲

Booth [33] (p:p, 4.28 GeV) ○
Jaeger [30] (p:p, 5 GeV) ×
Blobel [28] (p:p, 6.84 GeV) □
Bogolyubsky [72] (p:p, 7.86 GeV - russian) ◇
Blumenfeld [44] (p:p, 11.45 GeV) △
Brick [31] (p:p, 16.6 GeV) ▽
Jaeger [46] (p:p, 19.6 GeV) ⬠
LoPinto [43] (p:p, 23.7 GeV) ○
Bailly [49] (p:p, 26 GeV) ×
Kichimi [42] (p:p, 27.6 GeV) □
Ansorge [63] (pbar:p, 200 GeV - $(\Lambda + \overline{\Lambda})/2$) ◇

Figure 7.19: Energy dependence of Λ and $\overline{\Lambda}$ midrapidity yield. Black symbols represent the Λ midrapidity yields, red symbols represent the $\overline{\Lambda}$ midrapidity yields. The blue symbols are the $(\Lambda+\overline{\Lambda})/2$ results in $\overline{\text{p}}$-p collisions.

7.5 Transverse Momentum Distributions of Λ and $\overline{\Lambda}$ at Midrapidity

In order to study differences between Λ and $\overline{\Lambda}$ production at midrapidity, the transverse momentum distributions of these particles at $y = 0$ (-0.25< y <0.25) are compared in figure 7.20. The $\overline{\Lambda}$ points were scaled to match the Λ results at low p_T. The different slope of Λ and $\overline{\Lambda}$ is clearly visible from this plot. The different slopes of the spectra can also be an indication for the different production mechanisms responsible for baryon and antibaryon production. The yield and transverse momentum distribution of pair-created Λs is assumed to be the same as those of the $\overline{\Lambda}$. In order to estimate the transverse momentum distribution of non-pair-created Λs at midrapidity, the function (6.1) was fitted to the $\overline{\Lambda}$ transverse momentum distribution (without scaling), and then subtracted from the Λ transverse momentum distribution. This is also shown on the plot with red triangles (scaled to match the Λ distribution at low p_T.) A fit of the function (6.1) to these points (shown with red dashed line) gave the value of the T parameter $T_{\Lambda-\overline{\Lambda}} = 184$ GeV.

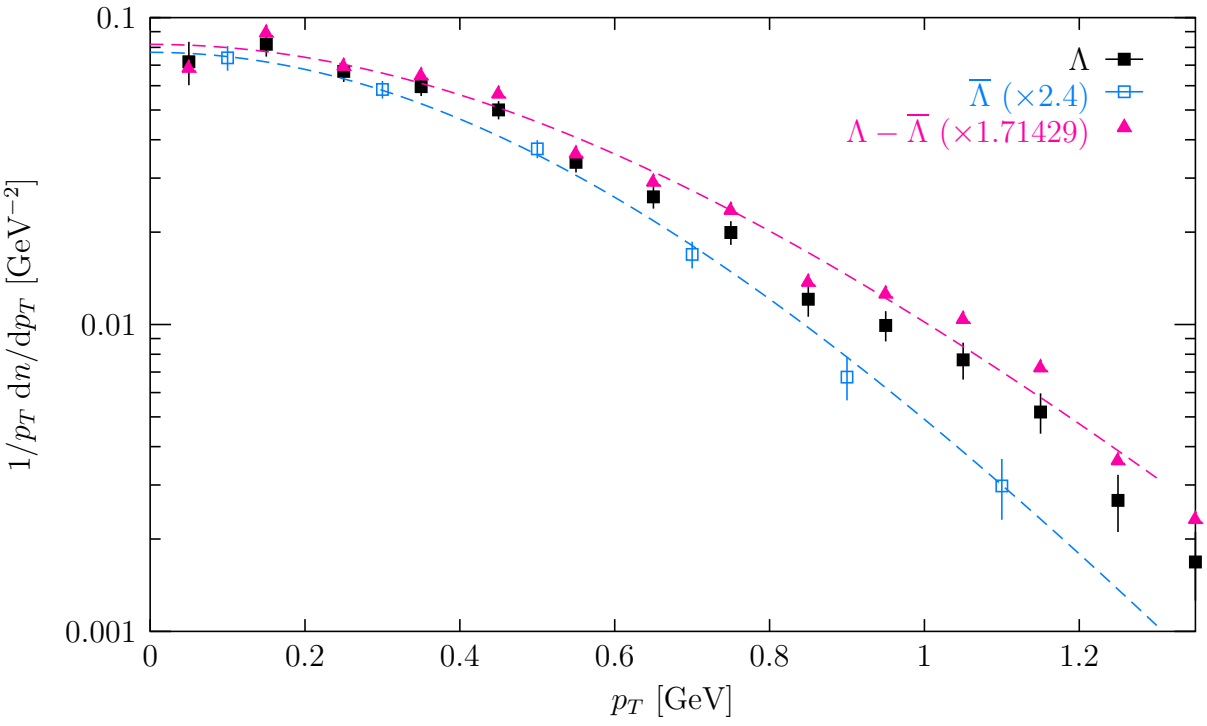

Figure 7.20: Λ and $\overline{\Lambda}$ transverse momentum distributions at midrapidity. The $\overline{\Lambda}$ and Λ − $\overline{\Lambda}$ results were scaled by the indicated factors to match the Λ points at low p_T

The difference of transverse momentum distributions of baryons and antibaryons at midrapidity is not a unique property of Λs. The transverse momentum distributions of

protons and antiprotons in p-p collisions at p_{beam}=158 GeV are shown in figure 7.21. The proton and antiproton spectra have been scaled in order to match the spectra of Λ and $\overline{\Lambda}$, respectively. The slopes of proton and Λ agree within errors; the same is true for the antibaryons as well.

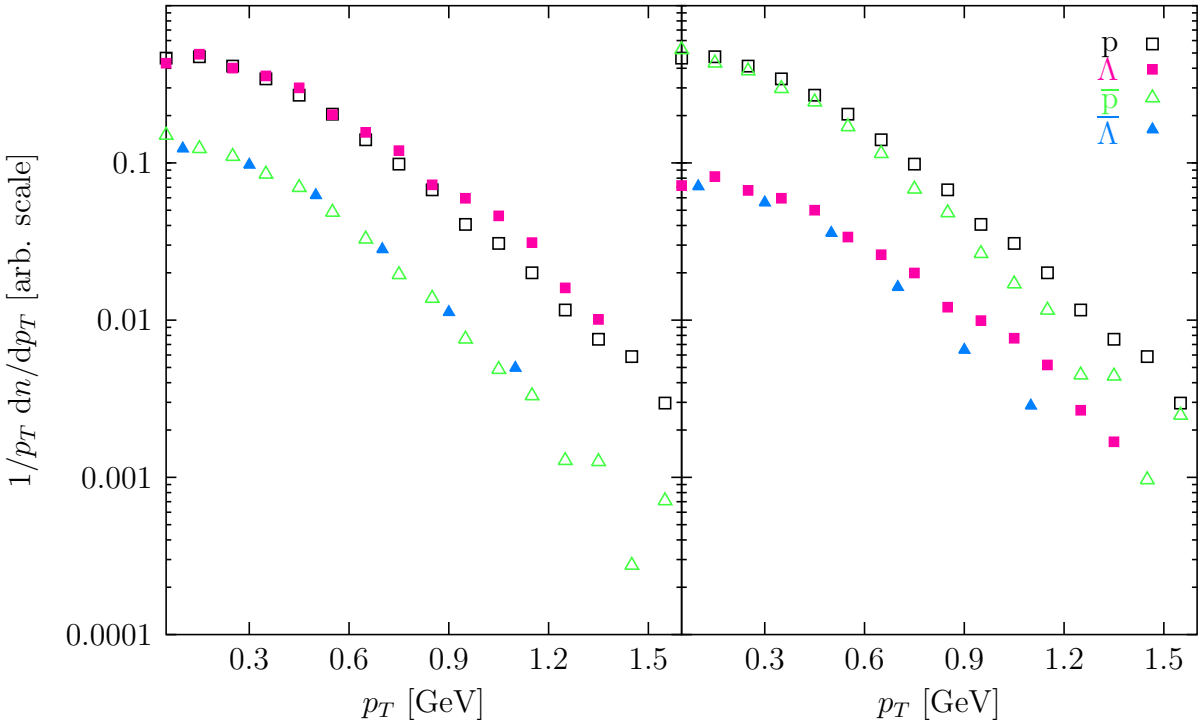

Figure 7.21: The transverse momentum distributions of protons and antiprotons in p-p collisions (arbitrary scale) measured by NA49 (preliminary results) compared to the p_T distributions of Λ and $\overline{\Lambda}$ at the same energies. The left panel demonstrates the similarity of Λ-proton and $\overline{\Lambda}$-$\overline{\mathrm{p}}$ slopes. The right panel demonstrates the same qualitative difference between proton and antiproton spectra, which was observed for the hyperons.

7.6 Study of Baryon-Antibaryon Correlations

7.6.1 Experimental Results

The constituents of the produced $\overline{\Lambda}$s clearly can not originate from the valence quarks of the projectile or target proton: these antiquarks are newly created in the collision. Due to the conservation laws their corresponding antiparticles (quarks) also have to be created in the collision. This quark-antiquark pair production is not a surprising fact. But this doesn't necessarily involve that baryons are also produced in symmetric B$\overline{\mathrm{B}}$ pairs (where B denotes a baryon, $\overline{\mathrm{B}}$ denotes its antibaryon): the produced quarks

and antiquarks do not have to organize into hadrons in the same way. For example $\overline{\Lambda}$s do not have to be produced in pairs with Λs. The antistrangeness and antibaryon number associated with an $\overline{\Lambda}$ can be compensated by different particles. Some processes involving $\overline{\Lambda}$ production are

			Threshold	
pp	$\rightarrow$	$p\ \overline{\Lambda}\Lambda\ p$	4.106 GeV	(7.1a)
		$p\ \overline{\Lambda}p\ \Lambda$	4.106 GeV	(7.1b)
		$p\ \overline{\Lambda}\Sigma^+\ n$	4.377 GeV	(7.1c)
		$p\ \overline{\Lambda}pK^-\ p$	4.426 GeV	(7.1d)

where the notation reflects the position of the particles in longitudinal momentum space: the two leading baryons (from the target and projectile) are separated from the rest by spaces. Among these reactions the energetically most favored one is (7.1a), but the difference in the threshold energies is not large. Reactions (7.1a) and (7.1b) have the same threshold energy and the same particle content in the final state. They differ only in the position of the particles in momentum space: in reaction (7.1b) at least one quark (the s quark created in pair with the $\overline{s}$ antiquark) has to be accelerated to large momenta, and at least one valence quark of the projectile has to be stopped to low momenta; this process is expected to be of smaller probability. These considerations lead to the expectation, that pair-produced baryons should be at low rapidities.

In order to check baryon-antibaryon pair-production, a subsample from the whole dataset was selected using an *antibaryon trigger* ($\overline{\text{B}}$-trigger): those events are accepted for the analysis, which contain an antibaryon (which can be either an antiproton or an antilambda, according to the purpose of the analysis) around midrapidity. Note that triggering on antibaryons (instead of baryons at midrapidity) is necessary, since baryons with small rapidities can be produced by stopping, without the presence of a baryon-antibaryon pair. For these studies – since the low statistics was the biggest problem – the combined results of the two finders were used: the V^0 candidates found by `VOFIND` were completed with the extra candidates found by `MTVO`.

For Λ-$\overline{\Lambda}$ correlation studies those events were selected ($\overline{\Lambda}$-events), which contained an antilambda candidate fulfilling the following requirements:

- dE/dx cut of the daughters around the Bethe-Bloch curve — 3σ
- Rapidity range — -0.7 < y <0.7
- Distance of the V^0 vertex from the primary vertex — > 12 cm
- Impact parameter of the $\overline{\Lambda}$ trajectory at the main vertex — $|b_x| < 1.2$ cm, $|b_y| < 0.7$ cm
- The angle of the decay plane (see fig. 5.1) — $|\cos(\phi)| < 0.96$
- Transverse momentum — $p_T < 1.2$ GeV
- Invariant mass with the $\overline{\Lambda}$ hypothesis (this region will be called the *peak-range*) — $|m_{\text{inv}} - 1.115| < 10$ MeV

The cuts mentioned above were chosen as a compromise between two main goals: keeping the most events with a possibly clear $\overline{\Lambda}$ mass peak. The invariant mass distribution of $\overline{\Lambda}$s with these cuts (except the last one of course) is shown in figure 7.22. The number of $\overline{\Lambda}$-events was 9247.

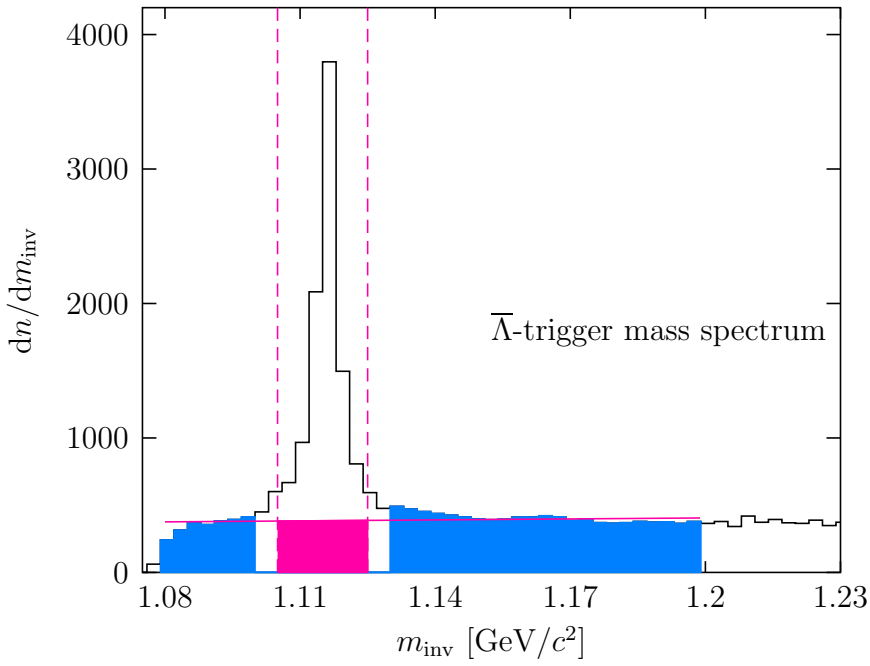

Figure 7.22: Invariant mass distribution of $\overline{\Lambda}$s after the cuts mentioned before. The selected mass range of the $\overline{\Lambda}$ triggers is indicated with the dashed red lines.

The statistics of Λs in the selected subsample of the events (containing a good $\overline{\Lambda}$ candidate within the mass range indicated in figure 7.22) was not sufficient to derive the yield in rapidity-p_T bins. The rapidity spectrum of Λs was derived using the whole p_T range in each rapidity bin. This of course introduces a dependency of the results on the

transverse momentum distribution of the simulated particles, through the uncertainty of the correction factors. This uncertainty can be estimated by calculating the correction factors in $y - p_T$ bins from the simulation, and weighting these correction factors by transverse momentum distributions of the form (6.1) with different T parameters:

$$\frac{1}{C_y} = \frac{\sum_{p_T} \frac{1}{C_{y,p_T}} \cdot f(T, p_T)}{\sum_{p_T} f(T, p_T)} \tag{7.2}$$

where C_y is the "overall" correction factor in a rapidity bin (the inverse of the acceptance in that bin), C_{y,p_T} is the correction factor in a rapidity–p_T bin, and $f(T, p_T)$ is the number of simulated particles in the transverse momentum bin p_T (the integral of the function (6.1) with parameter T over the p_T bin), and the sums run over the p_T bins. (The nominator of the right-hand side is the total number of detected particles, whereas the denominator is the total number of generated particles in the rapidity-bin). Using the correction factors derived from the simulation in p_T bins of 10 MeV width, and two values of the T parameter ($T = 130$ MeV and 180 MeV) the uncertainty of the results is estimated to be less than 7% within the used rapidity range [-1.25;1.25].

Due to the small statistics, in the $\overline{\Lambda}$-events much looser cuts were applied for the Λs, than before: only a 3σ cut around the Bethe-Bloch curve of the daughters was applied, and the decay vertex of the Λ was required to be at least 12 cm away from the primary vertex. After these cuts the number of candidates over the background is about 840. The rapidity distribution of Λs in $\overline{\Lambda}$-events (per $\overline{\Lambda}$-event) is shown in figure 7.23 in blue, compared to the same distribution in minimum-bias p-p events (black) (ignore the green and red symbols for the moment). Note that while in the case of minimum-bias p-p events the Λ spectrum had to be multiplied by the ratio of our trigger cross section to the total inelastic cross section of p-p collisions (we wanted to obtain the yield per inelastic event, and we had to take into account, that not all inelastic events are accepted by our trigger, see section 5.2), the same multiplication does not have to be done for the Λ spectrum in $\overline{\Lambda}$-events (our goal is to derive the yield per $\overline{\Lambda}$-events).

Before analyzing these results, let us study how the same spectrum behaves if we trigger on $\overline{\Lambda}$ candidates *outside* of the previous invariant mass range ($\pm$10 MeV around the nominal $\overline{\Lambda}$ mass), and select those events, which have no $\overline{\Lambda}$ candidate within this range, but do have a candidate within the blue region shown in figure 7.22 (1.08<

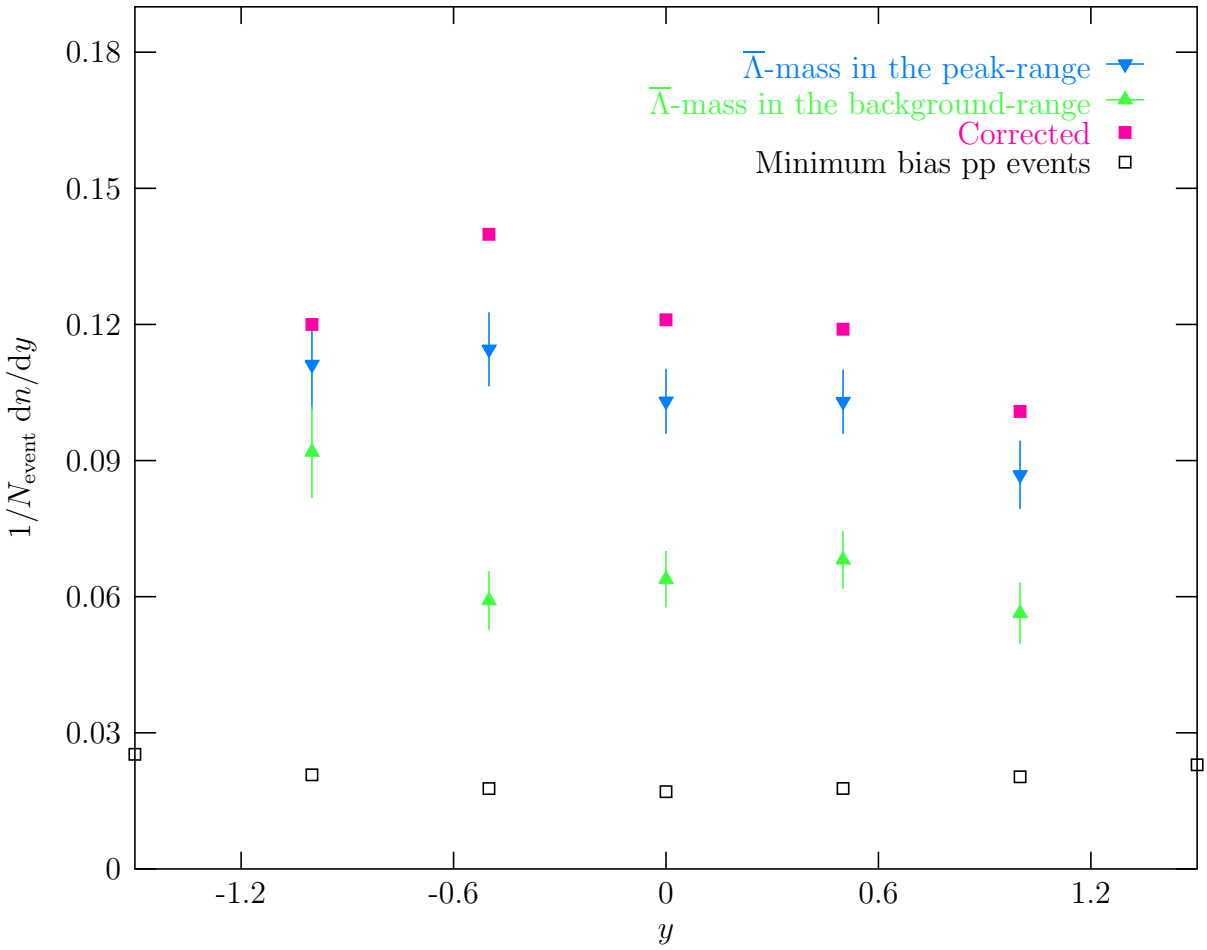

Figure 7.23: The rapidity distribution of Λs in $\overline{\Lambda}$-events, together with the same distribution in minimum-bias p-p events.

m_{inv} <1.1 or 1.13< m_{inv} <1.2 MeV). This range will be referred to as the *background region*. Since in these events there is most probably an antiproton (we required the negative daughter of the [most probably fake] V^0 candidate to have a dE/dx value closer than 3σ to the Bethe-Bloch curve of the antiproton), by baryon number conservation we expect to also have an increased number of baryons (and therefore an increased number of Λs) in these events. The rapidity distribution of Λs in these events is also shown in figure 7.23 in green. According to our expectation this yield is also higher than the Λ yield in minimum bias p-p events.

Since the background is not zero below the $\overline{\Lambda}$-peak in the $\overline{\Lambda}$-trigger mass spectrum (fig. 7.22), our $\overline{\Lambda}$-event sample contains extra events, where the $\overline{\Lambda}$ trigger is fake. The Λ

yield (per event) therefore contains a contribution by these events:

$$\text{Yield (per event)} = \frac{\Lambda_{\text{true}} + \Lambda_{\text{fake}}}{N_{\text{true}} + N_{\text{fake}}} \tag{7.3}$$

where Λ_{true} is the total number of lambdas in those events, where the $\overline{\Lambda}$ candidate is a real antilambda, Λ_{fake} is the total number of lambdas in those events, where the $\overline{\Lambda}$ candidate is fake. Similarly, N_{true} and N_{fake} are the number of these events, respectively. For simplicity we will assume, that each entry in the $\overline{\Lambda}$ mass histogram in figure 7.22 originates from a separate event (this assumption is true within 5% accuracy). If this assumption is valid, the number of background events within the peak-range of the $\overline{\Lambda}$-mass (N_{fake}) can be estimated by fitting a first order polynomial to the mass spectrum in the background-range (blue region), and calculating the surface below this polynomial in the peak-range (red region in figure 7.22). Assuming that the the Λ yield in events with a fake $\overline{\Lambda}$ candidate is independent from the invariant mass of the fake $\overline{\Lambda}$-trigger, we can estimate Λ_{fake} as the total number of lambdas in the events with an $\overline{\Lambda}$ mass in the background region, scaled by the ratio of the number of fake $\overline{\Lambda}$-events within the peak-range of the $\overline{\Lambda}$-mass (N_{fake}, the red area in 7.22) to the number of events having an $\overline{\Lambda}$-mass in the background region (the blue area in 7.22). Subtracting Λ_{fake} and N_{fake} from the observed number of lambdas and from the number of events, respectively, we can obtain the corrected number of lambdas per event corresponding to real $\overline{\Lambda}$-events, which is also shown in figure 7.23 in red.

Though the points are scattered (due to the small statistics), one can draw some conclusions from this plot:

- Compared to minimum bias p-p events, the probability of Λ production is about 4-5 times higher in those events, which contain an $\overline{\Lambda}$.
- The shape of the distribution has also changed: in contrast to the distribution in minimum bias p-p events, the Λ rapidity distribution in $\overline{\Lambda}$-events is peaking at midrapidity, similarly to the $\overline{\Lambda}$ rapidity distribution.

The increased Λ-yield in the $\overline{\Lambda}$-events, compared to minimum bias p-p events is not a surprise. By the selection of events containing an $\overline{\Lambda}$ one selects more violent collisions, where probably all particle species are more abundantly produced. A more fruitful study would be to compare the results of the same analysis with different antibaryon triggers.

For $\overline{\mathrm{p}}$-Λ correlation studies those events were selected, which fulfilled the following requirements ($\overline{\mathrm{p}}$-events):

- There is an antiproton candidate with transverse momentum less than 1.2 GeV.
- The rapidity of this antiproton candidate falls in the range [-0.9;0.9]. Together with the previous condition this not only selects particles around midrapidity, but also assures, that the total laboratory momentum of the antiproton candidate is greater than 3.4 GeV, therefore excludes the cross-over region of the Bethe-Bloch curves (see figure 3.2).
- Since the Bethe-Bloch curves of negative kaons and antiprotons are close, an antiproton selection using a band around the Bethe-Bloch curve of the antiproton would contain a large contamination of kaons as well. Therefore it was required, that the antiproton candidate has a dE/dx value *below* the nominal Bethe-Bloch curve. Another event sample was selected with the additional requirement that the dE/dx of the antiproton candidate be outside of a 3σ band around the Bethe-Bloch curve of the kaon ($\overline{3\sigma K}$).
- There is *no* $\overline{\Lambda}$ candidate in the event: those events were excluded from the analysis, which had a $\overline{\Lambda}$ candidate fulfilling the following criteria: both daughters have a measured dE/dx within a 3σ band around the corresponding Bethe-Bloch curve; rapidity of the candidate falls between -1.2 and 1.2; the invariant mass of the candidate is closer than 0.015 GeV to the nominal $\overline{\Lambda}$ mass.

The last requirement was introduced in order to exclude such events, where the antiproton candidate is not a primary particle, but originates from an antilambda. In order to increase the probability of the exclusion of $\overline{\Lambda}$-events from this sample, the requirements on the $\overline{\Lambda}$ candidate were much looser than those used for the analysis of the $\overline{\Lambda}$ spectra (Table 5.1). Since the detection and reconstruction efficiency of the NA49 detector and reconstruction software is not 100%, this event sample can still contain a contamination by $\overline{\Lambda}$-events. Their fraction can be estimated as follows: according to preliminary NA49 result on $\overline{\mathrm{p}}$ production, the $\overline{\Lambda}$ rapidity distribution is roughly 0.3 times that of the $\overline{\mathrm{p}}$; the branching ratio of the $\overline{\Lambda}$ into the charged channel is 64%, and the probability of not observing an $\overline{\Lambda}$ with the above mentioned cuts in the rapidity range [-1.2;1.2] is 36% (obtained from the simulation). These factors give a 7% contamination of $\overline{\Lambda}$-events into our $\overline{\mathrm{p}}$-event sample.

The rapidity distribution of Λs in $\overline{\text{p}}$-events is shown in figure 7.24 with and without the additional $\overline{3\sigma K}$ selection criteria, compared to the rapidity distribution of Λs in $\overline{\Lambda}$-events and minimum-bias p-p events. In $\overline{\text{p}}$-events (similarly to the $\overline{\Lambda}$-events) we can also observe the change of the shape of the rapidity distribution compared to the minimum-bias p-p collisions: it is peaking at midrapidity. The increase of the Λ yield is also significant, in the central region the yield has increased by about a factor of 3. However, this is still much smaller than the increase seen in $\overline{\Lambda}$-events. These results indicate a significantly stronger $\overline{\Lambda}$-Λ than $\overline{\text{p}}$-Λ correlation.

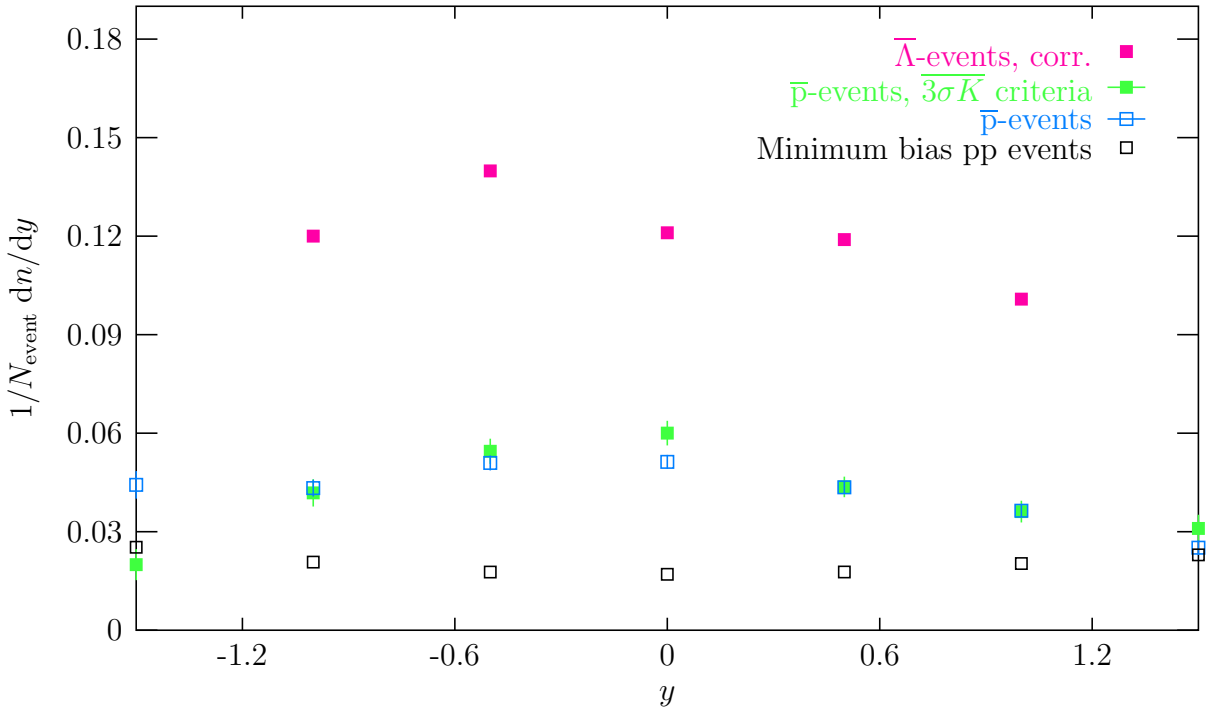

Figure 7.24: Rapidity distribution of Λs in $\overline{\text{p}}$-events

The results presented in this section originate from a study started recently. Since no similar studies exist yet on the market, one awaits for confirmation or disproof by other experiments, and these results are considered to be preliminary at the moment. However, this should not keep us from interpreting these results.

In order to estimate the total Λ yield in $\overline{\Lambda}$-events, the corrected rapidity distribution of Λs (red symbols in figure 7.23) is fitted with a Gaussian (which had a fixed width, σ=1, see formula in figure 7.25). The resulting amplitude is $A = 0.35$. The total Λ yield per $\overline{\Lambda}$-event (the surface below this curve) is therefore 0.35. This result signals a strong Λ-$\overline{\Lambda}$ correlation: in 35% of the cases $\overline{\Lambda}$-production is associated with Λ-production.

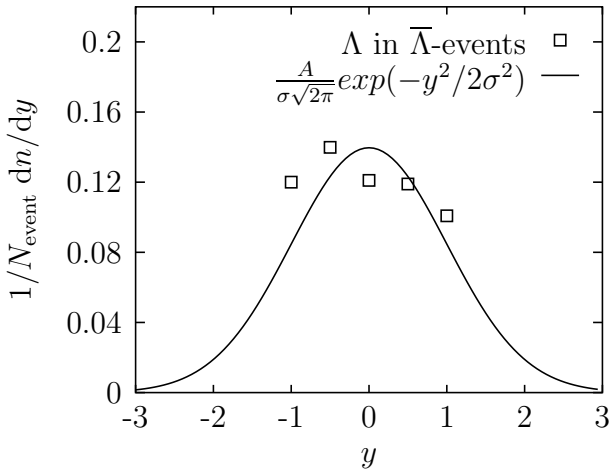

Figure 7.25: Rapidity distribution of Λs in $\overline{\Lambda}$-events, and the fitted Gaussian

A similar direction of research has been carried out at the CERN ISR [53] (at $\sqrt{s}$=53 and 62 GeV). The invariant mass spectrum of $\overline{\rm p}\pi^+$ pairs was studied in those events, which had four or more charged tracks, and two of the other tracks formed a Λ ($1.106 < M_{p\pi^-} < 1.126$). A peak was observed at the antilambda mass, whereas no peak was observed, if the invariant mass of the $\rm p\pi^-$ pair fell outside of the Λ peak ($1.086 < M_{p\pi^-} < 1.106$ or $1.126 < M_{p\pi^-} < 1.146\ GeV$), indicating that Λ production is possible without an associated $\overline{\Lambda}$, but $\overline{\Lambda}$s are always produced in conjunction with a Λ in events with four- (or more) prong topology. However, the available statistics for this analysis was quite low (about 50 entries), and the acceptance of the detector was not the most appropriate for Λ-$\overline{\Lambda}$ correlation studies: while $\overline{\Lambda}$s (and pair-produced Λs) are mostly produced at the central region ($|x_F| < 0.3$, see figure 7.5), the ISR detector had acceptance for Λs and $\overline{\Lambda}$s at $x_F > 0.3$, therefore the simultaneous production of Λ-$\overline{\Lambda}$ pairs could only be studied at $x_F^{\rm total} > 0.6$, with both the Λ and $\overline{\Lambda}$ being forward-going.

In section 7.5 the different slope of the transverse mass spectra of baryons and antibaryons was attributed to different production mechanisms. Antibaryons were assumed to be created via pair-production, while at these energies two mechanisms were supposed to be responsible for baryon production: baryon stopping and pair-production. Assuming that baryons observed in conjunction with an antibaryon are created via pair-production, one can check the validity of the above ideas. Figure 7.26 shows the transverse momentum distribution of Λs in $\overline{\Lambda}$-events and $\overline{\rm p}$-events. Contrary to our expectations the shape of the p_T distribution of Λs in $\overline{\rm B}$-events (where the Λ sample should be dominated by pair-created Λs) is very similar to the p_T distribution in minimum-bias

p-p events (where the dominant fraction of Λs is not pair-created).

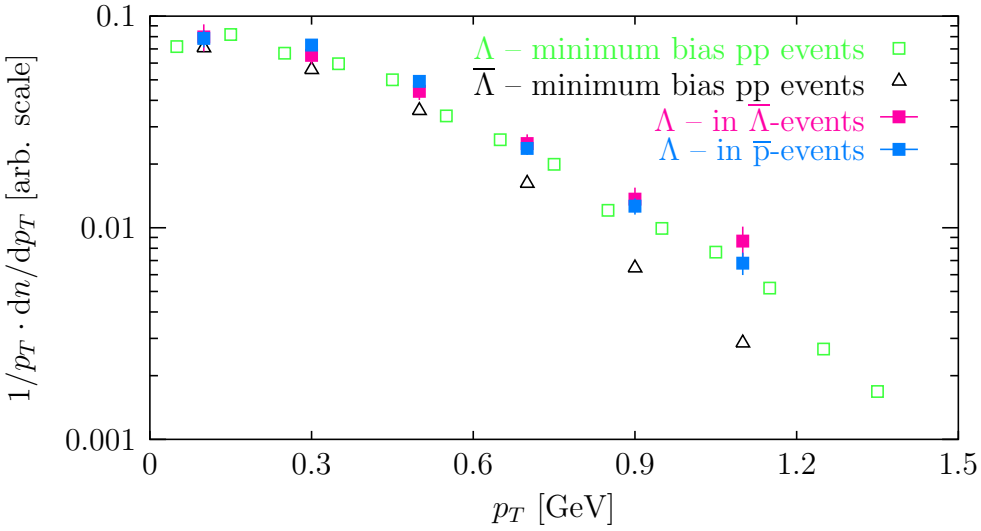

Figure 7.26: Transverse momentum distribution of Λs in $\overline{\Lambda}$-events and $\overline{p}$-events

7.6.2 Comparison to Model Predictions

Two event generators (VENUS and HIJING) were tested with the above experimental results. Figure 7.27 shows the results of these tests. The rapidity distributions predicted by the two models are shown in the upper panels. The `VENUS`-predicted rapidity distribution of Λs in minimum bias p-p collisions has a minimum at midrapidity, in accordance with the measured distribution. The distribution of Λs created together with an $\overline{\Lambda}$ has a completely different shape, which agrees with the $\overline{\Lambda}$ distribution. The peaks corresponding to the leading particle effect have disappeared. The `HIJING`-predicted rapidity distribution of Λs in minimum bias p-p collisions also shows the two peaks in the backward and forward hemispheres, but it has a plateau in the central region, which can be attributed to pair-production: in this region the Λ and $\overline{\Lambda}$ rapidity distributions in minimum bias p-p collisions agree (the Λ and $\overline{\Lambda}$ rapidity distribution in the upper right panel are to be directly compared). If Λs are created together with an $\overline{\Lambda}$, the shape of the central region does not change. It is interesting to observe that though the relative weight of the leading-baryon peaks has decreased, they can still be observed, contrary to `VENUS`-predictions (this distribution has been scaled by 5.4 relatively to the rapidity distributions of Λ and $\overline{\Lambda}$ in order to demonstrate the similarity in shape with the $\overline{\Lambda}$ distribution in the central region).

The p_T distributions at midrapidity, predicted by the two models are shown in the lower panels. `VENUS` predicts, that the distributions of Λ and $\overline{\Lambda}$ have a different shape in minimum bias collisions, in accordance with the observations. However, the shape of the p_T distribution of Λs changes, if we select Λs created together with an $\overline{\Lambda}$, which is in contradiction with the measured results. `HIJING` predicts, that the shape of the Λ p_T distribution does not change if one selects Λs created together with an $\overline{\Lambda}$ – but there is also no difference between the Λ and $\overline{\Lambda}$ p_T distributions in shape.

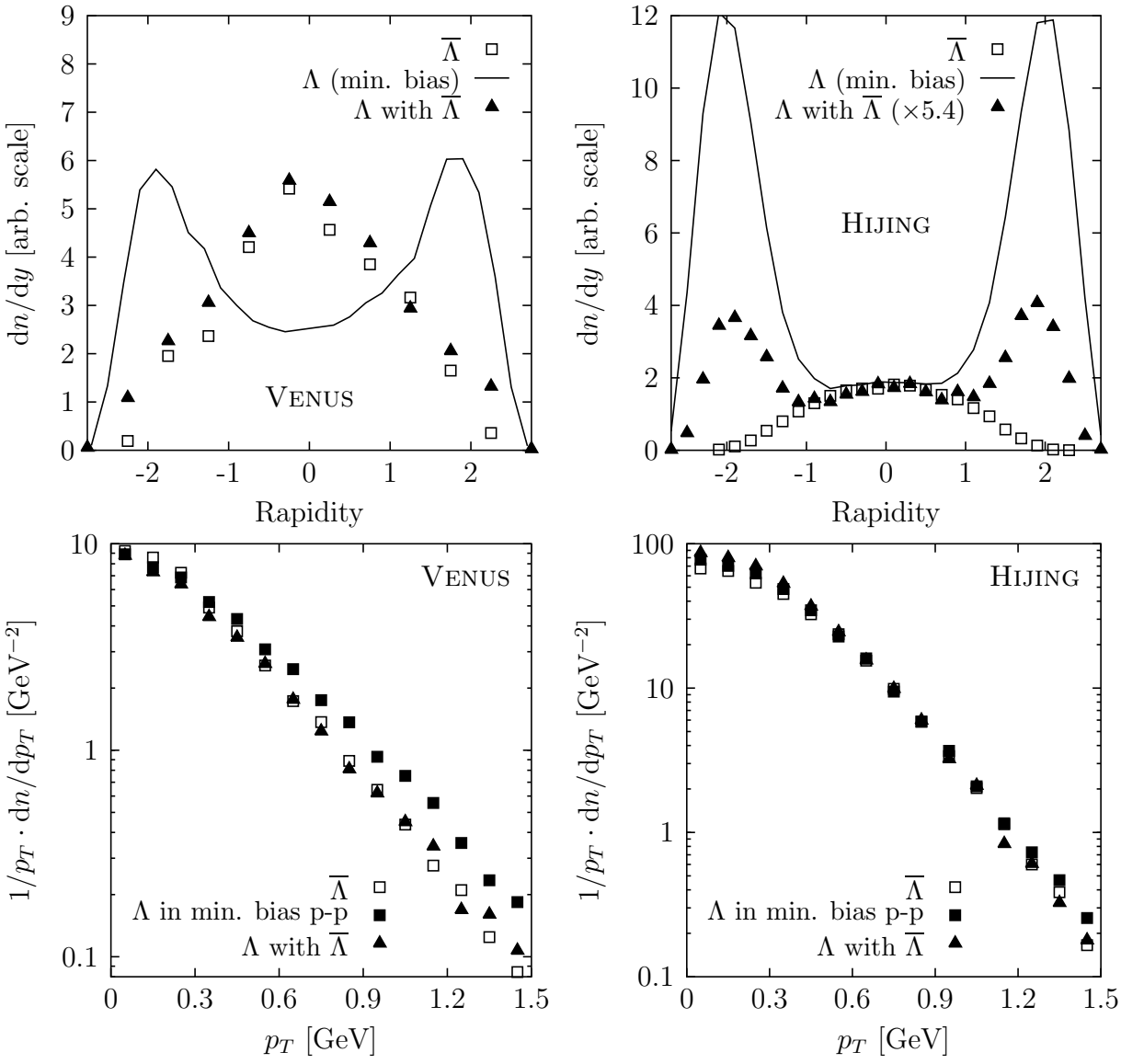

Figure 7.27: Comparison to Models. Left panels: Venus. Right panels: Hijing. The Venus rapidity distributions were scaled in order to demonstrate the similarity in shape between the $\overline{\Lambda}$ and Λ-with-$\overline{\Lambda}$ distributions. The Hijing Λ and $\overline{\Lambda}$ rapidity distributions are on the same scale, only the Λ-with-$\overline{\Lambda}$ distribution has been scaled by 5.4 relatively to the others.

7.7 Strangeness Enhancement in p-A and A-A collisions

Heavy ion or proton-nucleus collisions can occur with different impact parameters (with different centrality). Having a geometrical picture in mind, in heavy ion collisions only a certain part of the two nuclei will overlap, or *participate* in the collisions, depending on the centrality of the collision. Other parts (the *spectators*) will not participate. In proton-nucleus collisions, depending on the centrality of the event, the projectile proton will see different amounts of nuclear material, or with other words it will collide with different number of nucleons. Behind this picture there is necessarily the assumption, that the nucleons keep their identity after the first collision. In the case of a nucleon fragmenting into its constituents right after the first collision one could not speak about multiple collisions of a nucleon.

Strangeness enhancement seen in A-A collisions does not necessarily signal quark gluon plasma formation. This can have other reasons as well, such as the multiple collisions of the participating nucleons. Studying p-A collisions from the same aspect can provide useful information to decide if strangeness enhancement is a unique feature of heavy ion collisions, or can also be seen in p-A collisions, where quark gluon plasma formation is not expected. Moreover, the less complex p-A system is a good laboratory to study what happens with a nucleon suffering several collisions. Therefore the centrally selected A-A data should not be compared to inclusive p-A results, but the centrality dependence of strange particle yields in p-A collisions should also be studied.

In this subsection we first briefly summarize, how the centrality of the events, or the number of participants, or the average number of collisions suffered by a participant is determined by the different experiments. Particle yields will then be discussed as a function of these quantities.

7.7.1 Determination of Centrality or the Number of Collisions

The BNL experiment E910 at the AGS accelerator uses Time Projection Chambers as detectors. The multiplicity of *grey* protons and deuterons (identified in the momentum ranges [0.25,1.2] GeV and [0.5,2.4] GeV, respectively) was used to estimate the mean number of collisions suffered by the proton projectile, using a physics model to relate these quantities [88].

The WA97 experiment has dedicated multiplicity detectors, which count charged particles in the pseudo-rapidity range $2< \eta <4$. Their Pb+Pb data sample was divided into different multiplicity classes, in which the average number of participants, $N_{\rm part}$ was determined from a Wounded Nucleon Model fit to the charged multiplicity distribution. The p+Be and p+Pb data sample was not divided into centrality bins; the mean number of participants in an average p+Be or p+Pb collision was determined as the average value of inelastic collisions in the framework of the Glauber model (see [67] and references therein).

The p+Pb data sample of NA49 was recorded using different centrality triggers (using the Centrality Detector, see sec. 2.2), in order to enrich the data sample with higher-centrality events. The data sample was divided into two centrality bins with $N_{\rm grey} <6$ or $N_{\rm grey} \geq 6$, where $N_{\rm grey}$ is the number of gray particles (the number of hits detected in the centrality detector plus the number of particles detected in the TPCs in the momentum range 0.15 – 1 GeV). The number of collisions suffered by the projectile was related to the detected grey particle multiplicity using the `VENUS` model. For the centrality determination in Pb+Pb collisions the charged multiplicity observed in the detectors was used to estimate the number of participants.

7.7.2 Definitions of Strangeness Enhancement

As it was mentioned in section 1.1 strangeness enhancement in heavy ion collisions (compared to elementary, p-p collisions) can be a signature of quark-gluon plasma formation. Earlier experimental results were interpreted as a clear evidence for the absence of strangeness enhancement in proton-nucleus collisions, and for strangeness enhancement in heavy ion collisions, which was explained by the quark-gluon plasma state reached in the heavy ion collisions. However, the interpretation (enhancement or no enhancement) of the experimental results (the strange particle yields) strongly depends on the way one defines strangeness enhancement [84,86]. While the definition in A-A collisions is more or less straightforward, there are completely different approaches to define strangeness enhancement in p-A collisions.

Since in p-A or A-A collisions all particle species are more abundantly produced than in p-p collisions, the definition of enhancement clearly needs some normalization. Strange particle yields can be normalized for example to the pion yields, or to the number of participants in the collision. In this discussion we shall use the latter approach.

Wounded Nucleon Model (WNM)

In this picture strangeness enhancement in A-A and p-A collisions is defined as the excess of strangeness (at midrapidity) over the strangeness yield in proton-proton collisions, scaled by the number of wounded nucleons (participants). Since there are 2 wounded nucleons in proton-proton collisions, and N_W wounded nucleons in A-A collisions, the proton-proton yield is scaled by $N_W/2$, and the enhancement (E) is defined as

$$\left.\frac{\mathrm{d}N}{\mathrm{d}y}\right|_{y=0}^{AA} = E \cdot \frac{N_W}{2} \cdot \left.\frac{\mathrm{d}N}{\mathrm{d}y}\right|_{y=0}^{pp} \tag{7.4}$$

In proton-nucleus collisions, where the projectile proton collides with ν nucleons of the target nuclei the number of participants is $\nu + 1$. The enhancement (E) in p-A collisions is therefore defined as

$$\left.\frac{\mathrm{d}N}{\mathrm{d}y}\right|_{y=0}^{pA} = E \cdot \frac{\nu+1}{2} \cdot \left.\frac{\mathrm{d}N}{\mathrm{d}y}\right|_{y=0}^{pp} \tag{7.5}$$

The 2-Component Picture

In this picture [81,84] midrapidity yields are contributed to by both the target and the projectile. Therefore in the case of the symmetric proton-proton collisions both contributions are $^1/_2$ times the midrapidity yield. In the symmetric A-A collisions with N_{part} participants the number of participants on both the target and projectile side is $N_{\mathrm{part}}/2$. Therefore in the definition of enhancement the target and projectile contributions of proton-proton collisions are scaled by $N_{\mathrm{part}}/2$, and strangeness enhancement (E) is defined as

$$\left.\frac{\mathrm{d}N}{\mathrm{d}y}\right|_{y=0}^{AA} = E \cdot \frac{N_{\mathrm{part}}}{2} \cdot \frac{1}{2} \left.\frac{\mathrm{d}N}{\mathrm{d}y}\right|_{y=0}^{pp} + E \cdot \frac{N_{\mathrm{part}}}{2} \cdot \frac{1}{2} \left.\frac{\mathrm{d}N}{\mathrm{d}y}\right|_{y=0}^{pp} \tag{7.6}$$

In the asymmetric p-A collisions, however, strangeness enhancement is not attributed to all participating nucleons. There is an important difference between the target and projectile now: each of the ν participating target nucleons collide once, while the projectile proton suffers ν collisions. Therefore there is no reason to assume, that the target nucleons produce more strangeness than in proton-proton collisions. The target

contribution of proton-proton collisions is simply scaled by ν, and the enhancement is attributed to the projectile [81,84,86]:

$$\left.\frac{\mathrm{d}N}{\mathrm{d}y}\right|_{y=0}^{pA} = E \cdot \frac{1}{2} \left.\frac{\mathrm{d}N}{\mathrm{d}y}\right|_{y=0}^{pp} + \nu \cdot \frac{1}{2} \left.\frac{\mathrm{d}N}{\mathrm{d}y}\right|_{y=0}^{pp} \tag{7.7}$$

Note that in this picture the definition of enhancement in A-A collisions agrees with that in the Wounded Nucleon Picture, while the definition of enhancement in p-A collisions is different: the definition in the Wounded Nucleon Picture, eq. (7.5) will give a smaller enhancement, since the enhancement is distributed over all participants.

7.7.3 Experimental Results

Λ Yield in p-Au Collisions at $p_{\mathrm{beam}} = 17.5$ GeV

Centrality controlled studies of Λ production in p-Au collisions were first done by the E910 experiment at AGS at p_{beam}=17.5 GeV [87]. The integrated Λ yields at different centralities (number of collisions, ν) were compared to the N_{part}-scaled yield of pp collisions, $^1/_2 N^{pp}(\nu+1)$, where the Λ multiplicity in p-p collisions, N^{pp}=0.054 ($\pm$0.002) was obtained by parameterizing and interpolating the energy dependence of Λ multiplicities to $p_{\mathrm{beam}} = 17.5$ GeV. The Λ multiplicity was observed to initially increase faster with ν than expected from the N_{part} scaling (see fig. 7.28), meaning that strangeness enhancement is already seen in p-Au collisions, if one uses eq. (7.5) as the definition of enhancement.

The integrated Λ yield was also compared to a "binary-collisions" scaling of p-p data, $N^{\mathrm{BC}}(\nu) = N^{pp} \cdot \nu$ (the red line in figure 7.28). The idea behind this picture is that each subsequent collision of the projectile should produce the same amount of strangeness, which was considered to be the fastest plausible increase that could be expected from the multiple scattering of the incoming proton. The Λ yields were found to be consistent with this upper limit for $\nu \leq 3$. Above this region the fast increase stops, and one can observe a saturation, which could be explained by the decreasing center-of-mass energy of the subsequent collisions, or by the "exhaustion" of the poor projectile.

Λ and Ξ Midrapidity-Yields at the CERN-SPS

Though Λ and $\overline{\Lambda}$ yields at midrapidity have already been measured in p-p collisions by several experiments, in earlier interpretations of strangeness enhancement proton-beryllium collisions were used as a reference [67]. The strange particle yields, normalized

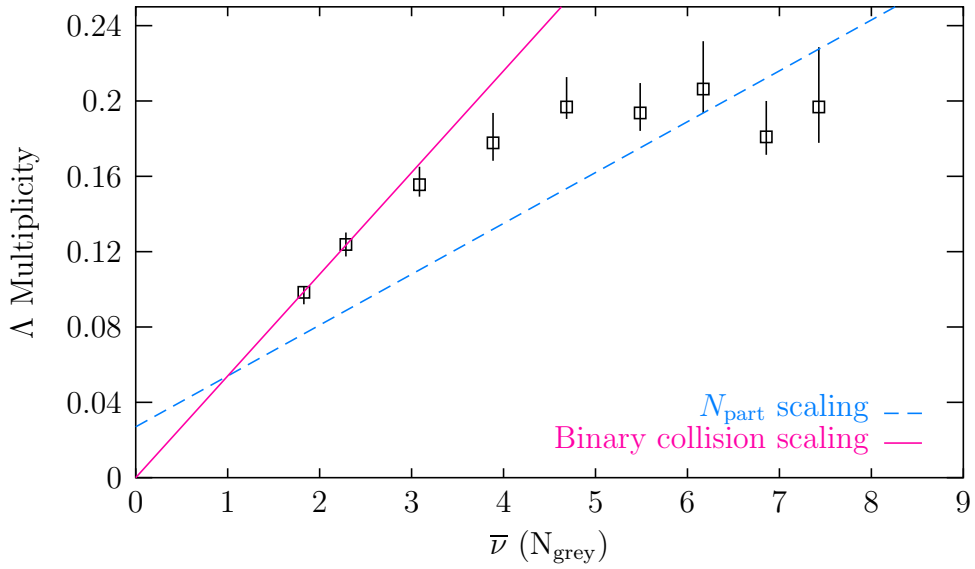

Figure 7.28: The Λ multiplicity as a function of number of collisions ν in p-Au collisions [87]

by the number of participants, relative to the p-Be results, as measured by the WA97 experiment [68] are shown in figure 7.29. In *minimum-bias* p-Pb collisions no strangeness enhancement was observed compared to p-Be collisions, whereas in Pb-Pb collisions the enhancement was significant, sometimes as high as a factor of about 3 for Λ, 8 for Ξ^-.

Using NA49's proton-proton data as a reference, using the other definition (equation 7.7) of strangeness enhancement for p-A collisions, and studying centrality-dependence of strange particle yields in p-A collisions, one can come to different conclusions. Strangeness enhancement at midrapidity in p-A and A-A collisions (with respect to p-p collisions) as defined by equations (7.6) and (7.7) is shown in figure 7.30. The preliminary p-Pb results of NA49 have been determined from an analysis using `VOFIND` and `XI_FIND` by [90]. This dataset has not yet been analyzed by `MTVO`, and these results are not feeddown-corrected. The Pb-Pb results of NA49 also originate from `VOFIND`- and `XI_FIND`-analyses, done by collaborators. From these plots it is clearly visible, that if one uses equation (7.7) to define strangeness enhancement in p-A collisions, and the results obtained by NA49 in p-p collisions as a reference, than an enhancement of about 2 or higher can be observed already in p-Be collisions. The enhancement is larger for larger number of collisions ν. The enhancement seen in Pb-Pb and p-Pb collisions is of similar magnitude.

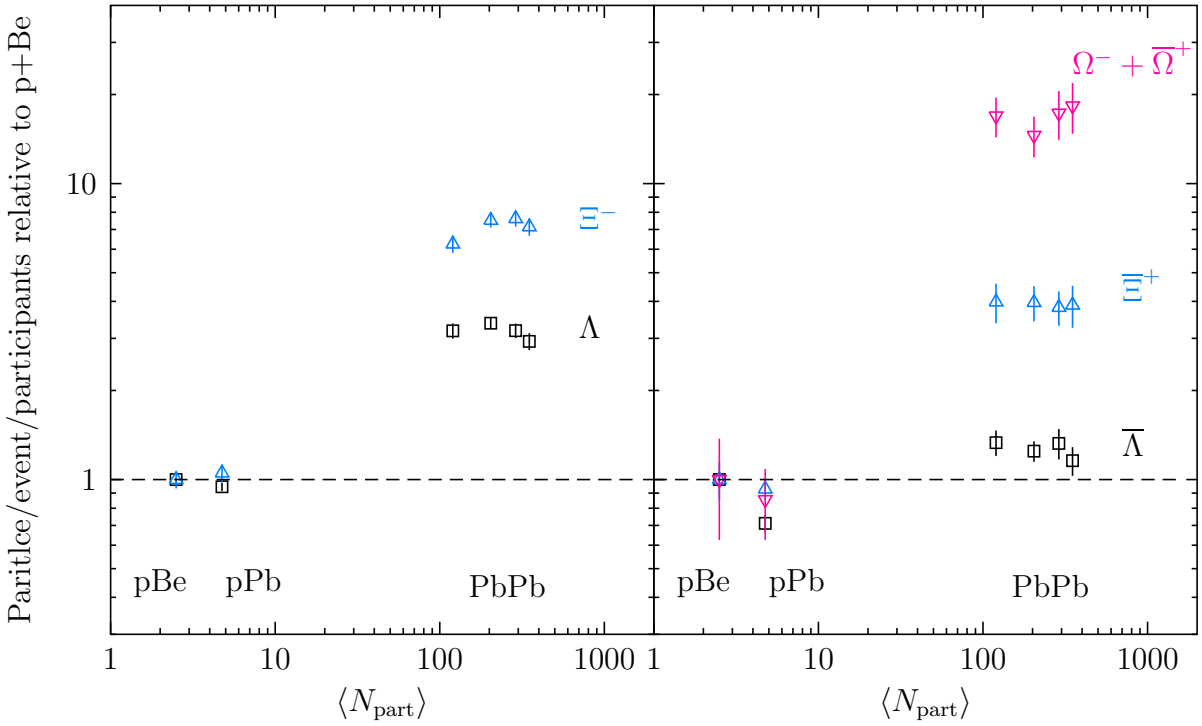

Figure 7.29: Yields per unit rapidity per participant relative to p+Be, as measured by the WA97 collaboration [67]

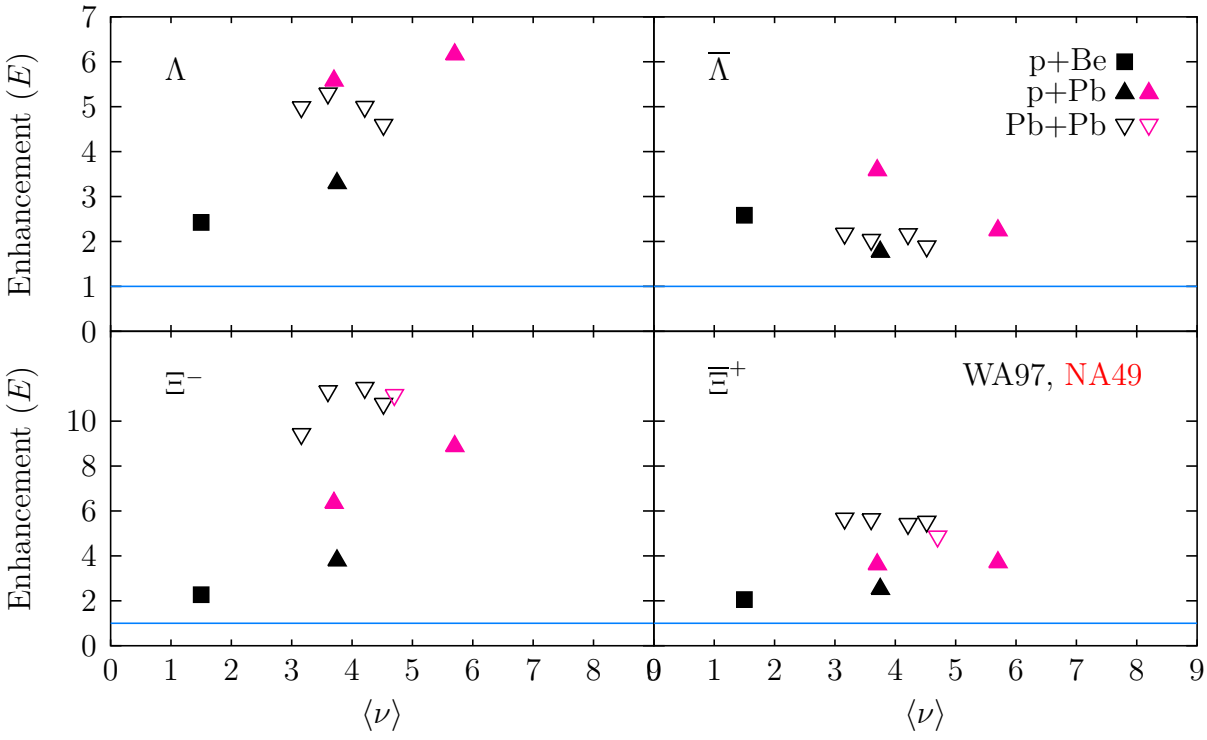

Figure 7.30: Strangeness enhancement in p-A and A-A collisions at midrapidity, as a function of the number of collisions per participant. Black symbols show WA97 results, red symbols are NA49 results.

7.8 Summary and Outlook

The availability of the new results on strange baryon production in proton-proton collisions from the high-statistics NA49 experiment opened new possibilities in particle and heavy ion physics.

Strangeness enhancement studies in heavy ion collisions have new reference data. It has been shown in this thesis (and in other recent publications), that strangeness enhancement should be interpreted with caution: proton-nucleus collisions also show an enhancement, which is similar in magnitude to the enhancement seen in nucleus-nucleus collisions. Besides the indispensable proton-proton measurements one needs detailed (centrality controlled) results from proton-nucleus collisions. We expect a lot of new results to emerge from the experiments at RHIC, and the future experiment *ALICE* at the CERN LHC.

The observation of the Ω^- particle, and the upper limit estimation of the $\overline{\Omega}^+/\Omega^-$ ratio extend the results on the antibaryon-to-baryon ratios to the whole strangess range. These results are in clear contradiction with string models, which predict very high $\overline{\mathrm{B}}/\mathrm{B}$ ratios for $s = 2, 3$ particles. With the analysis of the increased statistics of proton-proton data of the NA49 experiment the $\overline{\Omega}^+$ particle should be visible, and its production cross section will hopefully be estimated.

Results on strange baryon correlations opened the possibility to study the properties of strangeness and baryon production. The similar shape of the Λ and proton p_T distributions at midrapidity suggest a common property of baryons. Antibaryons ($\overline{\Lambda}$ and antiproton) also have a very similar shape, which is different from that of the baryons. The shape of the Λ p_T distribution does not change if one selects Λs created in conjunction with antibaryons. If one assumes, that these Λs are created with the same mechanism as the $\overline{\Lambda}$s (pair production), these observations open the question, what is then responsible for the different slopes of the p_T distributions? These results will hopefully initiate further studies on particle correlations, and will contribute to a more accurate understanding of hadronic reactions.

Appendix A

Numerical Results

The numerical results (the final Λ, $\overline{\Lambda}$, Ξ^- and $\overline{\Xi}^+$ spectra) are presented in the following tables.

Table A.1: Longitudinal distributions of Λ, $\overline{\Lambda}$, Ξ^- and $\overline{\Xi}^+$ (per inelastic event, shown in figures 7.4, 7.5, 7.8 and 7.9)

Rapidity distributions

y	-1.5	-1	-0.5	0	0.5	1	1.5
Λ ($\times 10^2$)	2.53±0.20	2.07±0.09	1.77±0.08	1.70±0.04	1.77±0.04	2.03±0.06	2.29±0.11
$\overline{\Lambda}$ ($\times 10^2$)		0.33±0.05	0.51±0.03	0.56±0.02	0.49±0.02	0.31±0.02	
Ξ^- ($\times 10^4$)		8.29±1.93	7.84±0.99	7.99±0.95	7.68±1.05	7.85±1.87	
$\overline{\Xi}^+$ ($\times 10^4$)			3.17±0.59	3.81±0.59	3.47±0.57	2.13±0.75	

Feynman-x distributions

x_F	-0.3	-0.2	-0.1	0	0.1	0.2	0.3
Λ ($\times 10^2$)	7.60±0.58	8.59±0.55	10.17±0.44	11.04±0.21	10.02±0.19	8.52±0.33	6.92±0.46
$\overline{\Lambda}$ ($\times 10^2$)		1.08±0.14	2.80±0.16	3.61±0.11	2.55±0.11	1.15±0.07	
Ξ^- ($\times 10^4$)		27.59±7.95	39.03±5.15	45.86±5.25	38.94±5.56	30.98±7.61	
$\overline{\Xi}^+$ ($\times 10^4$)			16.34±3.07	22.98±3.00	14.80±2.83		

Invariant Feynman-x distributions

x_F	-0.3	-0.2	-0.1	0	0.1	0.2	0.3
Λ ($\times 10^2$)	2.53±0.19	2.14±0.13	1.82±0.08	1.64±0.03	1.79±0.04	2.11±0.08	2.31±0.15
$\overline{\Lambda}$ ($\times 10^2$)		0.27±0.03	0.50±0.03	0.53±0.02	0.45±0.02	0.28±0.02	

Table A.2: Λ and $\overline{\Lambda}$ yields in $p_T - y$ bins

1.35	0.0016±0.0006	0.0036±0.0004	0.0025±0.0005	0.0022±0.0005			
1.25			0.0037±0.0006	0.0033±0.0007	0.0038±0.0007		
1.15	0.0046±0.0009	0.0077±0.0010	0.0054±0.0008	0.0059±0.0008	0.0057±0.0010	0.0075±0.0009	
1.05			0.0074±0.0009	0.0080±0.0011	0.0064±0.0010		
0.95	0.0127±0.0013	0.0112±0.0011	0.0087±0.0008	0.0094±0.0010	0.0081±0.0010	0.0096±0.0010	0.0121±0.0021
0.85			0.0111±0.0010	0.0102±0.0012	0.0119±0.0013		
0.75	0.0253±0.0036	0.0188±0.0015	0.0144±0.0014	0.0149±0.0013	0.0145±0.0011	0.0189±0.0015	0.0194±0.0027
0.65			0.0176±0.0013	0.0169±0.0014	0.0182±0.0015		
0.55	0.0352±0.0062	0.0249±0.0026	0.0194±0.0012	0.0185±0.0013	0.0197±0.0015	0.0262±0.0017	0.0295±0.0025
0.45			0.0228±0.0018	0.0225±0.0015	0.0237±0.0016		
0.35	0.0314±0.0093	0.0251±0.0023	0.0220±0.0014	0.0208±0.0014	0.0221±0.0016	0.0240±0.0014	0.0336±0.0030
0.25			0.0189±0.0017	0.0167±0.0012	0.0181±0.0012		
0.15		0.0095±0.0014	0.0131±0.0010	0.0122±0.0010	0.0134±0.0012	0.0092±0.0009	0.0128±0.0018
0.05			0.0051±0.0007	0.0035±0.0005	0.0048±0.0007		
p_T [GeV]/y	-1.5	-1	-0.5	0	0.5	1	1.5

1.15		0.0009±0.0002	0.0013±0.0002	0.0013±0.0003	0.0016±0.0003	0.0009±0.0002	
1.05							
0.95		0.0015±0.0003	0.0029±0.0004	0.0025±0.0004	0.0022±0.0003	0.0015±0.0003	
0.85							
0.75		0.0028±0.0005	0.0049±0.0006	0.0049±0.0004	0.0042±0.0004	0.0029±0.0004	
0.65							
0.55		0.0040±0.0013	0.0061±0.0006	0.0077±0.0005	0.0060±0.0004	0.0036±0.0004	
0.45							
0.35		0.0044±0.0014	0.0062±0.0005	0.0072±0.0004	0.0062±0.0004	0.0042±0.0004	
0.25							
0.15		0.0019±0.0008	0.0030±0.0003	0.0030±0.0002	0.0031±0.0003	0.0017±0.0002	
0.05							
p_T [GeV]/y	-1.5	-1	-0.5	0	0.5	1	1.5

Table A.3: Λ and $\overline{\Lambda}$ yields in $p_T - x_F$ bins

1.35	0.0100±0.0016	0.0135±0.0018	0.0100±0.0024	0.0115±0.0028			
1.25			0.0177±0.0031	0.0171±0.0034	0.0196±0.0041		
1.15	0.0181±0.0032	0.0276±0.0036	0.0259±0.0044	0.0303±0.0052	0.0255±0.0045	0.0242±0.0041	
1.05			0.0376±0.0046	0.0405±0.0054	0.0340±0.0056		
0.95	0.0359±0.0047	0.0436±0.0042	0.0471±0.0059	0.0495±0.0061	0.0457±0.0057	0.0352±0.0047	0.0374±0.0072
0.85			0.0588±0.0056	0.0620±0.0069	0.0604±0.0072		
0.75	0.0741±0.0102	0.0758±0.0075	0.0791±0.0082	0.0940±0.0065	0.0758±0.0066	0.0718±0.0069	0.0598±0.0091
0.65			0.0988±0.0087	0.1137±0.0077	0.1047±0.0086		
0.55	0.1064±0.0201	0.1071±0.0100	0.1164±0.0101	0.1312±0.0089	0.1097±0.0085	0.1165±0.0092	0.0850±0.0117
0.45			0.1366±0.0115	0.1499±0.0087	0.1415±0.0092		
0.35		0.1272±0.0180	0.1435±0.0100	0.1460±0.0085	0.1357±0.0091	0.1115±0.0075	0.0899±0.0123
0.25			0.1119±0.0107	0.1223±0.0080	0.1142±0.0084		
0.15		0.0510±0.0097	0.0828±0.0084	0.0891±0.0064	0.0801±0.0054	0.0439±0.0055	0.0397±0.0090
0.05			0.0329±0.0055	0.0295±0.0039	0.0292±0.0041		
p_T [GeV]$/x_F$	-0.3	-0.2	-0.1	0	0.1	0.2	0.3

1.15		0.0030±0.0009	0.0067±0.0012	0.0082±0.0017	0.0070±0.0014		
1.05							
0.95		0.0059±0.0013	0.0141±0.0022	0.0149±0.0020	0.0117±0.0018		
0.85							
0.75		0.0095±0.0025	0.0249±0.0032	0.0311±0.0027	0.0230±0.0023	0.0102±0.0019	
0.65							
0.55		0.0135±0.0063	0.0340±0.0041	0.0510±0.0027	0.0316±0.0024	0.0159±0.0018	
0.45							
0.35			0.0372±0.0041	0.0500±0.0028	0.0352±0.0025	0.0130±0.0020	
0.25							
0.15			0.0190±0.0026	0.0210±0.0017	0.0154±0.0015	0.0073±0.0017	
0.05							
p_T [GeV]$/x_F$	-0.3	-0.2	-0.1	0	0.1	0.2	0.3

Appendix B

Kinematical variables

Particles created in high-energy collisions are usually classified by their longitudinal (parallel to the collision axis) and transverse momentum. If we choose the coordinate axis z to be the collision axis, the transverse momentum component is $p_T = \sqrt{p_x^2 + p_y^2}$ The transverse momentum of the particle is often characterized by its *transverse mass*: $m_T = \sqrt{p_T^2 + m^2}$, where m is the mass of the particle.

To characterize the longitudinal momentum of the particle, different schools prefer different variables. One of the choices is *rapidity*:

$$y = \frac{1}{2} \cdot \log\left(\frac{E + p_z}{E - p_z}\right)$$

where E is the particle's energy, and p_z is't longitudinal momentum component. The advantage of rapidity is, that it is only modified by an additional constant when a Lorentz boost (with a velocity β) along the z axis is performed:

$$y \to y + \frac{1}{2} \log\left(\frac{1 - \beta}{1 + \beta}\right)$$

Therefore comparisons between different frames (for example center of mass system, and laboratory frame) is straightforward, and the shape of rapidity distributions is unchanged. The disadvantage of rapidity is, that it mixes the longitudinal and transverse momentum components.

The other choice to characterize the longitudinal momentum of the particle is *Feynman's scaling variable* x_F, which is the particle's longitudinal momentum component divided by the momentum of the beam particle (everything calculated in the center of mass frame):

$$x_F = \frac{p_z^{\mathrm{cm}}}{p_{\mathrm{beam}}^{\mathrm{cm}}}$$

Experimental data confirms, that above a certain collision energy (around 13 GeV) for most particles the x_F-distributions have a similar shape, independently from the collision energy.

The invariant Feynman-x distribution is defined as the integral of the invariant cross section over p_T (the energy-weighted transverse momentum distribution):

$$F(x_F) = \frac{1}{\pi} \int \frac{E}{p_{\text{beam}}^{\text{cm}}} \frac{\mathrm{d}N}{\mathrm{d}x_F \, \mathrm{d}p_T} \mathrm{d}p_T \tag{B.1}$$

The relation between the invariant Feynman-x and rapidity distribution at midrapidity (or $x_F = 0$, which is the same) can be easily calculated. Using the definitions of Feynman-x and rapidity in the center of mass frame one gets

$$x_F = \frac{E}{p_{\text{beam}}^{\text{cm}}} \tanh y \tag{B.2}$$

where E is the particle's energy. Let us take a rapidity bin of width $\mathrm{d}y$ around midrapidity, and calculate the momentum region in the variables x_F and p_T, which this rapidity bin corresponds to:

$$\mathrm{d}x_F|_{y=0} = \frac{E}{p_{\text{beam}}^{\text{cm}}} \tanh(\mathrm{d}y)\bigg|_{y=0} = \frac{E}{p_{\text{beam}}^{\text{cm}}} \frac{1}{\cosh^2 y} \mathrm{d}y\bigg|_{y=0} = \frac{E}{p_{\text{beam}}^{\text{cm}}} \mathrm{d}y \tag{B.3}$$

This means, that the x_F range, which corresponds to the rapidity-bin $\mathrm{d}y$ around midrapidity gets wider with increasing p_T. Its width is proportional to the particle's energy E. Using the relation between $\mathrm{d}x_F$ and $\mathrm{d}y$ at midrapidity, the midrapidity yield can be directly related to the value of the invariant Feynman-x distribution:

$$\frac{\mathrm{d}N}{\mathrm{d}y}\bigg|_{y=0} = \int \frac{\mathrm{d}N}{\mathrm{d}y \, \mathrm{d}p_T} \mathrm{d}p_T\bigg|_{y=0} = \int \frac{E}{p_{\text{beam}}^{\text{cm}}} \frac{\mathrm{d}N}{\mathrm{d}x_F \, \mathrm{d}p_T} \mathrm{d}p_T = \pi \, F(x_F)|_{x_F=0} \tag{B.4}$$

Acknowledgements

I would like to thank my advisor György Vesztergombi for his support, and for giving me the possibility to join such a prestigious institution as CERN. He devoted a lot of effort to expose his students to competitive situations, and to let them have a wide experience in experimental particle physics.

I am very grateful for my closest colleagues at CERN, with whom I worked on this topic. I felt lucky to share this work with Tatjana Šusa, who was always ready to help, often devoting her freetime. Her endurance was really inspiring. Kreso Kadija could very successfully mix good atmosphere with hard and conscious work. Both were necessary to carry out this work. I am very grateful for his encouragement and direction in physics.

Hans Gerhard Fischer is the initiator and maintainer of the elementary beam program in the NA49 experiment. He spent a lot of effort on keeping the experiment running. I am grateful for his support and critics, which helped me to make efforts for better results. His fascinating knowledge about the physics literature was a great help for me.

I express my gratitude to my colleagues and friends from Budapest: Zoltán Fodor, Ferenc Siklér, Gábor Veres and Dezső Varga, for their help in both scientific and everyday questions. Ferenc, Gábor and Dezső provided me excellent company at our dinner-parties at CERN. I am especially grateful to Gábor for his useful comments about this thesis. We had a lot of stimulating discussions with Ferenc, from which I profited a lot. Besides, he made my alldays a fun with his continous tomfoolery. I directly profited a lot from Dezső's critical attitude, and useful suggestions as well.

I am especially grateful to Péter Lévai for his directions and thorough comments about my thesis.

I would like to thank Latchezar Betev, whom I could always ask anything about the experiment. I am grateful for the members of the NA49 experiment, who were responsible for its continous operation: Peter Seyboth, Reinhard Stock, Siegfried Wenig, and all collaborators of the experiment.

My work was partially supported by the Hungarian Scientific Research Fund (OTKA) under the contracts F034707 and T0032293. I acknowledge the travel grants of the Doctoral School of the Eötvös Loránd University.

I am most grateful to my family for they continous support and love, and for all I got from them during my life, which were the basis for all I reached in life.

Bibliography

[1] http://www.bnl.gov/bnlweb/facilities/AGS.html

[2] http://www.bnl.gov/rhic/

[3] http://www.cern.ch

[4] *S. Afanasev et al.*, The NA49 Large Acceptance Hadron Detector – Nucl. Instrum. Meth. A430:210-244 (1999)

[5] http://na49info.cern.ch/

[6] *S.A. Bass, M. Gyulassy, H. Stöcker, W. Greiner*, Signatures of Quark-Gluon-Plasma formation in high energy heavy-ion collisions: A critical review – J.Phys. G25, 1 (1999)

[7] *T. Matsui, H. Satz*, J/ψ Suppression by Quark-Gluon Plasma Formation – Phys.Lett. B178, 416 (1986)

[8] *J. Rafelski, B. Müller*, Strangeness Production in the Quark-Gluon Plasma – Phys.Rev.Lett. 48, 1066 (1982)

[9] *P. Koch, J. Rafelski, B. Müller*, Strangeness in Relativistic Heavy Ion Collisions – Phys.Rep. 142, 167 (1986)

[10] *M.C. Abreu et al.*, The dependence of the anomalous J/ψ suppression on the number of participant nucleons – Nucl. Phys. B521, 195-203 (2001)

[11] *J. Ashman et al.*, An Investigation of the Spin Structure of the Proton in Deep Inelastic Scattering of Polarised Muons on Polarised Protons – Nucl.Phys. B328, 1 (1989)

[12] *B. Frois*, The Spin Structure of the Nucleon – Prog.Part.Nucl.Phys. 34, 87-101 (1995)

[13] *M. Alberg*, Strangeness in the Nucleon – Prog.Parg.Nucl.Phys. 36, 217-228 (1996)

[14] *M.G. Sapozhnikov*, Polarized strangeness in the nucleon – Nucl.Phys. A692, 63 (2001)

[15] *J. Ellis, M. Karliner, D.E. Kharzeev, M.G. Sapozhnikov*, Abundant Phi Meson Production in $\overline{p}p$ Annihilation at Rest and Strangeness in the Nucleon – Phys.Lett. B353, 319 (1995)

[16] *J. Ellis, M. Karliner, D.E. Kharzeev, M.G. Sapozhnikov*, Hadronic probes of the polarized intrinsic strangeness of the nucleon – Nucl.Phys. A673, 256-278 (2000)

[17] *Keh-Fei Liu*, Strangeness Content in the Nucleon – J.Phys. G27, 511-522 (2001)

[18] *R.M. Sternheimer, R.F. Peierls*, General Expression for the Density Effect for the Ionization Loss of Charged Particles – Phys.Rev. B3, 3681-3692 (1971)

[19] *Rob. A. Barton*, Multi-Strange Hyperon Production in Relativistic Heavy Ion Collisions – PhD. thesis

[20] *Lee Barnby*, Measurement of Λ, $\overline{\Lambda}$ and K-short from Pb-Pb Collisions at 158 GeV per nucleon in a Large Acceptance Experiment – PhD. Thesis

[21] *Gábor I. Veres*, Baryon Momentum Transfer in Hadronic and Nuclear Collisions at the CERN NA49 Experiment – PhD. Thesis

[22] *Ferenc Siklér*, Részecskekorrelációk Vizsgálata Nagyenergiájú Nehézion-űtkőzésekben – PhD. Thesis, Budapest, 1997, Eőtvős Lorand University

[23] *Dezső Varga*, Semleges részecskék méreése a CERN NA49 kísérleténél – Diploma Thesis, Budapest, Eőtvős Lorand University

[24] An article to be published somewhere, OR: *Dániel Barna,* Strange Particle Production at 158 AGeV proton-proton Collisions – PhD Thesis in your hands

[25] *K. Geiger, D.K. Srivastava*, Parton cascade description of relativistic heavy ion collisions at the CERN Super Proton Synchrotron at 158A GeV? – Phys.Rev. C 56, 2718-2725 (1997)

[26] *V. V. Ammosov et al.*, Neutral strange particle production in pp interactions at 60 GeV/c – Nucl.Phys. B115, 269-286 (1976)

[27] *H. Bøggild et al.*, The Inclusive Single-Particle Spectra of π^-, K^0_S and Λ in Proton-Proton Collisions at 19 GeV/c – Nucl.Phys. B57, 77-99 (1973)

[28] *V. Blobel et al.*, Multiplicities, Topological Cross Sections, and Single Particle Inclusive Distributions from *pp* Interactions at 12 and 24 GeV – Nucl. Phys. B69, 454-492 (1974)

[29] *D.R. Ward et al.*, Comparison of Neutral Particle Production in 100 GeV/c $\overline{p}p$ and *pp* Interactions – Phys.Lett. B62, 237 (1976)

[30] *K. Jaeger*, Inclusive γ, π^0, K^0 and Λ production in 12.4-GeV/c pp interactions – Phys.Rev. D11, 1756 (1975)

[31] *Brick*, Inclusive production of neutral strange particles by 147 GeV/c $\pi^+/K^+/p$ interactions in hydrogen – Nucl.Phys. B164, 1-24 (1980)

[32] *Nandi*, Inclusive particle production in 100 geV/c $\pi^- p$ and $\bar{p}p$ interactions – Nucl.Phys. B169, 20-48 (1980)

[33] *Booth*, Differences between $\bar{p}p$ and pp interactions at 8.8 GeV/c and their relationship to $\bar{p}p$ annihilations – Phys.Rev. D27, 2018 (1983)

[34] *B.Y.Oh*, Inclusive study of Λ^0 and $\Sigma^\pm$ hyperons produced in proton-proton collisions from 6.6 to 28 GeV/c – Nucl.Phys. B49, 13-21 (1972)

[35] *J.W. Chapman*, Production of γ, Λ^0, K_S^0 and $\bar{\Lambda^0}$ in pp collisions at 102 GeV/c – Phys.Lett. B47, 465 (1973)

[36] *A. Sheng*, PP interactions at 300 GeV/c: γ and neutral-strange-particle production – Phys.Rev. D11, 1733 (1975)

[37] *R.D. Kass*, Charged- and neutral-particle production from 400-GeV/c pp collisions – Phys.Rev. D20, 605 (1979)

[38] *F.T. Dao*, PP interactions at 303 GeV/c: Inclusive studies of γ, K_S^0 and Λ^0 production – Phys.Rev.Lett. 30, 1151 (1973)

[39] *G. Charlton*, Neutral-Strange-Particle Production in 205-GeV pp interactions – Phys.Rev.Lett. 30, 574 (1973)

[40] *J. Whitmore*, Multiparticle Production in the Fermilab Bubble Chambers – Physics Reports 27, 187-273 (1976)

[41] *H. Kichimi et al.*, Inclusive Λ, $\overline{\Lambda}$ and $\Sigma^\pm(1385)$ Production in 405 GeV/c pp Interactions – Phys.Lett. B72, 411-414 (1978)

[42] *H. Kichimi*, Inclusive study of strange-particle production in pp interactions at 405 GeV/c – Phys.Rev. D20, 37 (1979)

[43] *F. LoPinto*, Inclusive K^0, Λ^0, $K*^\pm(890)$ and $\Sigma*^\pm(1385)$ production in pp collisions at 300 GeV/c – Phys.Rev. D22, 573 (1980)

[44] *H. Blumenfeld*, Inclusive neutral kaon and lambda production in 69 GeV pp interactions – Phys.Lett. B45, 528 (1973)

[45] *K. Alpgård*, A triple-regge analysis of the inclusive reaction $pp \to \Lambda + X^{++}$ at 19 GeV/c – Nucl.Phys. B105, 349-354 (1976)

[46] *K. Jaeger*, Characteristics of V^0 and γ production in pp interactions at 205 GeV – Phys.Rev.D 11, 2405 (1975)

[47] *M. Firebaugh*, Strange-Particle Production in 8-BeV/c Proton-Proton Interactions – Phys.Rev. 172, 1354 (1968)

[48] *Margaret Alston-Garnjost*, Neutral Particle Production in $\pi^+ p$ and pp Collisions at 100 GeV/c – Phys.Rev.Lett 35, 142 (1975)

[49] *J.L. Bailly*, Test of a Quark-diquark Fragmentation Mechanism in Proton-Proton interactions at 360 GeV/c – Zeit.Phys. C31, 367-373 (1986)

[50] *J.L. Bailly*, Analysis of transverse momentum distributions for pp interactions at 360 GeV/c in the framework of a quark-diquark fragmentation model – Zeit.Phys. C35, 295-300 (1987)

[51] *M. Asai*, Neutral Strange Particle Correlations in 360 GeV/c pp Interactions – Zeit.Phys. C34, 429 (1987)

[52] *M. Asai*, Inclusive K^0_S, Λ and $\bar{\Lambda}$ Production in 360 GeV/c pp Interactions Using the European Hybrid Spectrometer – Zeit.Phys. C27, 11-19 (1985)

[53] *S. Erhan*, Hyperon Production in pp Interactions at $\sqrt{s}$ = 53 and 62 GeV – Phys.Lett. B85, 447 (1979)

[54] *F.W. Büsser*, K^0 and Λ production at the CERN ISR – Phys.Lett. 61B, 309 (1976)

[55] *P. Chauvat*, Differences in Leading Baryon Production from $p\bar{p}$ and pp Collisions with $\sqrt{s}$ = 31 GeV at the CERN-ISR – Phys.Lett. 127B, 384 (1983)

[56] *D. Drijard*, Neutral Strange Particle Production in Proton-Proton Collisions at $\sqrt{s}$ = 63 GeV – Zeit.Phys. C12, 217-224 (1982)

[57] *G.J. Bobbink*, The production of high-momentum particles and resonances in pp collisions at the CERN Intersecting Storage Rings – Nucl.Phys. B217, 11-30 (1983)

[58] *M. Bourquin et al.*, Particle and Antiparticle Production by 200 GeV/c Protons in the Charged Hyperon Beam at the CERN SPS – Nucl.Phys. B153, 13-38 (1979)

[59] *Bocquet*, Inclusive Production of Strange Particles in $p\overline{p}$ Collisions at $\sqrt{s}$ = 630 GeV with UA1 – Phys.Lett B366, 441 (1996)

[60] *Alexopoulos*, Results from E735 at the Tevatron Proton-Antiproton Collider with $\sqrt{s}$ = 1.8 TeV – Nucl. Phys. A544, 343c (1992)

[61] *Alexopoulos et al.*, Hyperon production from proton-antiproton collisions at $\sqrt{s}$=1.8 TeV – Phys.Rev. D46, 2773 (1992)

[62] *Banerjee et al.*, Λ and $\overline{\Lambda}$ Production from Proton-Antiproton Collisions at $\sqrt{s}$ = 1.8 TeV – Phys.Rev.Lett. 62, 12 (1989)

[63] *Ansorge et al.*, Hyperon Production at 200-GeV and 900-GeV Center-of-Mass Energy – Nucl.Phys. B328, 36-58 (1989)

[64] *K. Alpgård et al.*, Strange Particle Production at the CERN SPS Collider – Phys.Lett. B115, 65 (1982)

[65] *G.J. Alner et al.*, Observation of Ξ^- Production in $\overline{p}p$ Interactions at 540 GeV cms Energy – Phys.Lett. B151, 309 (1985)

[66] *T. Virgili for the NA57 Collaboration*, Study of the Production of Strange and Multi-Strange Particles in Lead-Lead Interactions at the CERN SPS: the NA57 Experiment – Nucl.Phys. A681, 165c-173c (2001)

[67] *F. Antinori et al.*, Production of strange and multistrange hadrons in nucleus-nucleus collisions at the SPS – Nucl.Phys. A661, 130c-139c (1999)

[68] Strange particle yields measured by the WA97 experiment – http://wa97.web.cern.ch/WA97/Data/TableQM99.html

[69] *E.L. Berger*, Test of limiting behavior for Λ and K^0_1 produced in inclusive pp interactions – Phys.Rev.Lett. 28, 322 (1972)

[70] *R.L. Eisner*, Effects of beam polarization on Λ and K^0 inclusive production in pp interactions at 12 GeV/c – Phys.Rev. D21, 10 (1980)

[71] *M. Gazdziczki*, Strangeness in Nuclear Collisions – Zeit.Phys. C71, 55 (1996)

[72] *Bogolyubsky*, Study of Neutral Strange Particle Production in *pp* Interactions at 32-GeV/C and Comparison with $\overline{p}p$ Data. (In Russian) – Yad.Fiz. 50, 683-694 (1989)

[73] *William H. Press, Saul A. Teukolsky, william T. Vetterling, Brian P. Flannery*, Numerical Recipes in C – Cambridge University Press

[74] *Michael Schmelling*, Averaging Measurements with Hidden Correlations and Asymmetric Errors – arXiv:hep-ex/0006004

[75] Geant: Detector Description and Simulation tool – http://wwwinfo.cern.ch/asdoc/geant_html3/geantall.html

[76] *K. Werner*, Strings, Pomerons and the VENUS model of hadronic interactions at ultrarelativistic energies – Phys.Rept. 232, 87-299 (1993)

[77] *B. Andersson et al.*, A model for low p_T hadronic reactions, with generalizations to hadron-nucleus and nucleus-nucleus collisions – Nucl.Phys. B281, 289 (1987)

[78] http://o.home.cern.ch/o/ondrejch/public/vertex/vtx_corrs/

[79] *G.P. Yost*, Averaging in the presence of "sliding" errors – Nucl.Inst.Meth. A312, 598 (1992)

[80] *M. Schmelling*, Averaging measurements with hidden correlations and asymmetric errors. – hep-ex/0006004

[81] *Hans Gerhard Fischer*, Private communication

[82] *M. Bleicher et. al.*, Overpopulation of $\overline{\Omega}$ in pp Collisions: A Way to Distinguish Statistical Hadronization from String Dynamics – Phys.Rev.Lett. 88, 202501 (2002)

[83] *F. Becattini, G. Passaleva*, Statistical hadronisation model and transverse momentum spectra of hadrons in high energy collisions – hep-ph/0110312

[84] *T. Šusa*, Cascade Production in p+p, p+A and A+A Interactions at 158-AGeV (talk held at Quark Matter 2001) – Nucl.Phys. A698, 491-494 (2002)

[85] *K. Kadija*, Strange Particle Production in p+p, p+Pb and Pb+Pb Interactions from NA49 (talk held at *Strange Quarks in Matter*, Frankfurt, 2001) – J.Phys. G28, 1675-1682 (2002)

[86] *D. Barna*, Strange Particle Production in Nuclear Collisions at CERN NA49 (talk held at the 7th Rencontres de Moriond on Electroweak Interactions and Unified Theories) – hep-ex/0205042

[87] *I. Chemakin et al.*, Semi-Inclusive Λ and K_S Production in p-Au Collisions at 17.5 GeV/c – Phys.Rev.Lett. 85, 4868-4871 (2000)

[88] *I. Chemakin et al.*, Measuring centrality with slow protons in proton-nucleus collisions at the AGS – Phys.Rev. C60, 024902 (1999)

[89] *W.J. Metzger*, Statistical Methods in Data Analysis – University note at *Katholieke Universiteit Nijmegen, The Netherlands*

[90] *Tatjana Šusa*